Mitigation of Amyloid Protein Fibrillation and Cellular Interaction with Nanostructures

Ava Faridi

Micro & Nano Technology, MS

A thesis submitted for the degree of Doctor of Philosophy at Monash University in 2020

Drug Delivery, Disposition and Dynamics

Institute of Pharmaceutical Sciences, Monash University

381 Royal Parade, Parkville Victoria 3052, Australia

Table of content

Copyright notice

Abstract

Amyloidosis refers to structural disorders induced by protein misfolding and self-assembly towards β-sheet rich amyloid fibrils. Amyloidosis of human islet amyloid polypeptide (IAPP), amyloid-β (Aβ), tau and α-synuclein (αS) is a hallmark of type 2 diabetes (T2D) and neurological disorders including Alzheimer's disease (AD) and Parkinson's disease (PD). For AD, specifically, formation of intracellular tangles and extracellular plaques of tau and Aβ is coupled with the toxicity resulted from amyloidosis as well as inflammation, implicating a close relationship between Aβ amyloidosis and immunopathology for the disease.

Different mechanisms have been proposed for the amyloid induced toxicity. One of the well-established mechanism structural conversation. Indeed, upon the structure of amyloids transform from monomer to oligomer/fibril the toxicity increase dramatically. Current main strategies against amyloidosis employ small molecules, chaperone proteins or engineered nanomaterials, to regulate interactions with amyloid proteins through hydrogen bonding, hydrophobic interaction or π-π stacking. Oligomers and protofibrils, among all forms of amyloid protein aggregates, are known to be the most toxic species. The toxicity induced by protein fibrillation originates from structural transitions from random to alpha helical and β-sheet conformations, usually initiated by association of the N-terminus of amyloid proteins with cell membranes. Associations of oligomers and protofibrils with cell membranes may induce porosity and altered fluidity of the membranes, influence concentration gradients of physiological ions and cellular response to produce reactive oxygen species (ROS), autophagy and apoptosis. During the structural transformation of proteins, oligomers and protofibrils form chiral mesoscopic structures, a feature which has rarely been exploited in the development of therapeutics against amyloid diseases. On the other hand, although NPs have been introduced to mitigate the toxicity of amyloid proteins, the effects of nanoparticle inhibitors on intracellular protein expression and regulation remain largely unknown.

The main body of this thesis consists of three chapters. In the first chapter, the immune blood cells association and cytokine secretion upon cell exposure to oligomeric and fibrillar Aβ was investigated. The effect of the plasma protein corona on amyloid protein-cell interaction was determined. Experiments indicate changes in membrane association between whole blood and washed blood (i.e., without plasma proteins) were minor for Aβ oligomers and significant for Aβ fibrils across all immune cell types. Based on real-time measurement by a localized surface plasmon resonance sensor, exposure of immune cells to Aβ oligomers resulted in elevated expressions of cytokines IL-6 and TNF. However, exposure of immune cells to Aβ fibrils did not induce notable cytokine secretion. This stronger immune cell association and cytokine stimulation of Aβ oligomers over fibrils is an evidence on the contrasting toxicities of oligomeric versus fibrillar structures resulting from their differential capacities in binding with plasma proteins to render a corona. These observations on immune cell association and cytokine secretion support a connection between Aβ amyloidosis and immunopathology in AD.

Further research on the fundamentals of amyloid diseases was followed by an investigation of the mitigation of amyloid protein toxicity with nanoparticles (NPs). In this study, for the first time, chiral silica nanoribbons were applied to ameliorate the *in vivo* amyloidogenesis of IAPP. Chiral silica nanoribbons, especially the right-handed ones, accelerated IAPP fibrillization through elimination of their nucleation phase and shortening of their elongation phase. The directional binding between the NPs and IAPP was further examined through coarse-grained simulations. Reduction of IAPP toxicity in pancreatic β cells as well as improvement of embryo survival, development and behaviour of treated zebrafish were observed with right-handed silica nanoribbons, which targeted the primarily left-handed IAPP aggregates. These results demonstrated the potency of chiral nanostructures against the enantioselectivity of amyloid proteins, as well as the use of zebrafish embryos as a high-throughput *in vivo* model for probing the interactions of different nanostructures and amyloid proteins.

While NPs have shown effectiveness to various extent against protein aggregation and toxicity, changes induced by NP inhibitors on intracellular protein expression exposed to amyloid proteins have not been documented. In the following chapter, the proteome of pancreatic β cells upon exposure to monomeric, oligomeric and fibrillar IAPP structures was analysed. This was followed by an introduction of graphene quantum dots (GQDs), known as the inhibitor of IAPP fibrillation, to mitigate cellular protein dysregulation. Briefly, 29 proteins were significantly dysregulated after beta cell exposure to IAPP species, with majority of them nucleotide-binding proteins. Upon introduction of GQDs, mitigation of protein expression, especially in exposure to the toxic oligomeric structures, was observed. This study implicated the capacity of GQDs in regulating protein expression through hydrogen bonding and hydrophobic interactions and pointed to nanomedicines as a new frontier against human amyloid diseases.

Publications during enrolment

1. Nandakumar, A., Xing, Y., Aranha, R.R., **Faridi, A.**, Kakinen, A., Javed, I., Koppel, K., Pilkington, E. H., Purcell, A. W., Davis, P. T., Faridi, P., Ding, F., Ke, P. C. Human Plasma Protein Corona of Aβ Amyloid and Its Impact on Islet 2 Amyloid Polypeptide Cross-Seeding, ***Biomacromolecules***, (2020) doi.org/10.1021/acs.biomac.9b01650.

2. Javed, I., Peng, G., Xing, Y., Yu, T., Zhao, M., Kakinen, A., **Faridi, A.,** Parish, C.L., Ding, F., Davis, T.P., Ke, P.C., Lin, S. Inhibition of amyloid beta toxicity in zebrafish with a chaperone-gold nanoparticle dual strategy, ***Nature Communications,*** 10 (2019), 3780.

3. **Faridi, A.,** Yang, W., Kelly, H.G., Wang, C., Faridi, P., Purcell, A.W., Davis, T.P., Chen, P., Kent, S.J., Ke, P.C. Differential Roles of Plasma Protein Corona on Immune Cell Association and Cytokine Secretion of Oligomeric and Fibrillar Beta-Amyloid, (2019) ***Biomacromolecules***, 20 (2019), 4208-4217.

4. **Faridi, A.**, Sun, Y., Mortimer, M., Aranha, R.R., Nandakumar, A., Li, Y., Javed, I., Kakinen, A., Fan, Q., Purcell, A.W., Davis, T.P., Ding, F., Faridi, P., Ke, P.C. Graphene quantum dots rescue protein dysregulation of pancreatic β-cells exposed to human islet amyloid polypeptide, ***Nano Research***, 12 (2019), 2827–2834.

5. Kakinen, A., Xing, Y., Hegoda Arachchi, N., Javed, I., Feng, L., **Faridi, A**., Douek, A.M., Sun, Y., Kaslin, J., Davis, T.P., Higgins, M.J., Ding, F., Ke, P.C. Single-Molecular Heteroamyloidosis of Human Islet Amyloid Polypeptide, ***Nano Letters,*** 19 (2019) 6535-6546.

6. Sun, Y., Kakinen, A., Zhang, C., Yang, Y., **Faridi, A**., Davis, T.P., Cao, W., Ke, P.C., Ding, F. Amphiphilic surface chemistry of fullerenols is necessary for inhibiting the amyloid aggregation of alpha-synuclein NACore, ***Nanoscale***, 11 (2019), 11933-11945.

7. Javed, I., He, J., Kakinen, A., **Faridi, A**., Yang, W., Davis, T.P., Ke, P.C., Chen, P. Probing the Aggregation and Immune Response of Human Islet Amyloid Polypeptides with Ligand-

Stabilized Gold Nanoparticles, ***ACS Applied Materials and Interfaces,*** 11 (2019) 10462-10471.

8. Kakinen, A., Sun, Y., Javed, I., **Faridi, A**., Pilkington, E.H., Faridi, P., Purcell, A.W., Zhou, R., Ding, F., Lin, S., Ke, P.C., Davis, T.P. Physical and toxicological profiles of human IAPP amyloids and plaques, ***Science Bulletin***, 64 (2019), 26-35.

9. **Faridi, A.**, Sun, Y., Okazaki, Y., Peng, G., Gao, J., Kakinen, A., Faridi, P., Zhao, M., Javed, I., Purcell, A.W., Davis, T.P., Lin, S., Oda, R., Ding, F., Ke, P.C. Mitigating Human IAPP Amyloidogenesis In Vivo with Chiral Silica Nanoribbons, ***Small***, 14 (2018), 1802825.

10. Javed, I., Yu, T., Peng, G., Sánchez-Ferrer, A., **Faridi, A**., Kakinen, A., Zhao, M., Mezzenga, R., Davis, T.P., Lin, S., Ke, P.C. In Vivo Mitigation of Amyloidogenesis through Functional-Pathogenic Double-Protein Coronae, ***Nano Letters***, 18 (2018), 5797-5804.

11. Kakinen, A., Javed, I., ***Faridi, A.,*** Davis, T.P., Ke, P.C. Serum albumin impedes the amyloid aggregation and hemolysis of human islet amyloid polypeptide and alpha synuclein, ***Biochimica et Biophysica Acta – Biomembranes***, 1860 (2018), 1803-1809.

12. Pilkington, E.H., Gustafsson, O.J.R., Xing, Y., Hernandez-Fernaud, J., Zampronio, C., Kakinen, A., **Faridi, A.**, Ding, F., Wilson, P., Ke, P.C., Davis, T.P. Profiling the Serum Protein Corona of Fibrillar Human Islet Amyloid Polypeptide, ***ACS Nano,*** 12 (2018), 6066-6078.

13. Wang, M., Gustafsson, O.J.R., Pilkington, E.H., Kakinen, A., Javed, I., **Faridi, A**., Davis, T.P., Ke, P.C. Nanoparticle-proteome in vitro and in vivo, ***Journal of Materials Chemistry B***, 6 (2018), 6026-6041.

Thesis including published works declaration

I hereby declare that this thesis contains no material which has been accepted for the award of any other degree or diploma at any university or equivalent institution and that, to the best of my knowledge and belief, this thesis contains no material previously published or written by another person, except where due reference is made in the text of the thesis. This thesis includes 3 original papers published in peer reviewed journals. The core theme of the thesis is mitigation of amyloid protein fibrillation and their cellular interaction with nanomaterials. The ideas, development and writing up of all the papers in the thesis were the principal responsibility of myself, the student, working within the Drug Delivery, Disposition and Dynamics, Monash Institute of Pharmaceutical Sciences under the supervision of Professor Pu Chun Ke and Professor Thomas P. Davis. The inclusion of co-authors reflects the fact that the work came from active collaboration between researchers and acknowledges input into team-based research. In the case of chapters 2, 3 and 4, my contributions to the work involved the following:

Thesis Chapter	**Publication Title**	**Status** (published, in press, accepted or returned for revision, submitted)	**Nature and % of student contribution**	**Co-author name(s) Nature and % of Co-author's contribution***	**Co-author(s), Monash student Y/N***
2	*Differential Roles of Plasma Protein Corona on Immune Cell Association and Cytokine Secretion of Oligomeric and Fibrillar BetaAmyloid*	*Published*	*55%. Concept, method development, data collection and analysis, and writing first draft*	*1. Wen Yang; help in experiment 5%* *2. Hannah Gabrielle Kelly; help in experiment 4%* *3. Chuanyu Wang; read manuscript 1%*	*1.No* *2.No* *3.No* *4.Yes* *5.No* *6.No* *7.No* *8.No* *9.No*

				4. Pouya Faridi; help in experiment 2% *5. Anthony Wayne Purcell; manuscript proofreading 1%* *6. Thomas P. Davis; research supervision 10%* *7. Pengyu Chen; manuscript proofreading 1%* *8. Stephen J. Kent; manuscript proofreading 1%* *9. Pu Chun Ke; research supervision and manuscript preparation 20%*	
3	*Mitigating Human IAPP Amyloidogenesis In Vivo with Chiral Silica Nanoribbons*	*Published*	*56%. Concept, method development, data collection and analysis, and writing first draft*	*1. Yunxiang Sun; help in simulation 1%* *2. Yutaka Okazaki; help in experiment 2%* *3. Guotao Peng; help in experiment 1%* *4. Jie Gao; help in experiment 1%* *5. Aleksandr Kakinen; help*	*1.No* *2.No* *3.No* *4.No* *5.No* *6.No* *7.No* *8.No* *9.No* *10.No* *11.No* *12.No*

				in experiment 1% *6. Pouya Faridi; help in experiment 1%* *7. Mei Zhao; help in experiment 1%* *8. Ibrahim Javed; read manuscript 1%* *9. Anthony W. Purcell; manuscript proofreading 1%* *10. Thomas P. Davis; research supervision 10%* *11. Sijie Lin; manuscript proofreading 1%* *12. Reiko Oda; manuscript proofreading 2%* *13. Feng Ding; help in simulation 1%* *14. Pu Chun Ke; research supervision and manuscript preparation 20%*	*13.No* *14.No*

4	*Graphene quantum dots rescue protein dysregulation of pancreatic β-cells exposed to human islet amyloid polypeptide*	*Published*	*56%. Concept, method development, data collection and analysis, and writing first draft*	*1. Yunxiang Sun; help in simulation 2%* *2. Monika Mortimer; read manuscript 1%* *3. Ritchlynn R. Aranha; help in experiment 1%* *4. Aparna Nandakumar; read manuscript 1%* *5. Yuhuan Li; help in experiment 1%* *6. Ibrahim Javed; help in experiment 1%* *7. Aleksandr Kakinen; help in experiment 1%* *8. Qingqing Fan; read manuscript 1%* *9. Anthony W. Purcell; proofreading manuscript 2%* *10. Thomas P. Davis; research supervision 5%* *11. Feng Ding; manuscript proofreading 1%* *12. Pouya Faridi; help in data analysis & manuscript proofreading 10%*	*1.No* *2.No* *3.Yes* *4.Yes* *5.No* *6.No* *7.No* *8.No* *9.No* *10.No* *11.No* *12.No* *13.No*

				13. Pu Chun Ke; research supervision and manuscript preparation 17%	

I have renumbered sections of submitted or published papers in order to generate a consistent presentation within the thesis.

Student signature: Ava Faridi **Date: 08/05/2020**

The undersigned hereby certify that the above declaration correctly reflects the nature and extent of the student's and co-authors' contributions to this work. In instances where I am not the responsible author I have consulted with the responsible author to agree on the respective contributions of the authors.

Main Supervisor signature: Thomas P Davis **Date: 08/05/2020**

Acknowledgment

I would like to express my deepest appreciation to my supervisors Profs Pu Chun Ke and Thomas P. Davis for supporting me though my scientific and personal goals during these three years and provided me all opportunities and facilities to make my PhD journey memorable, joyful and productive. None of the achieved scientific outcomes personal skills would be possible without their guidance. Over my PhD program, I have contributed in 13 publications and improved my management and leadership skills owing to their encouragement and supervision.

I am grateful to the group members Dr Aleksandr Kakinen, Dr Ibrahim Javed, Emily Pilkington, Aparna Nandakumar, Kairi Koppel, Nikolaos Andrikopoulos, whom I had pleasure working during my PhD. I would like to thank my panel members, Prof Justin Gooding, Dr Nicholas Veldhuis and Dr Ruirui Qiao who provided me extensive professional guidance.

I would like to thank Prof Reiko Oda and her team for providing nanomaterials, Prof Feng Ding and his team for computational inputs, Prof Sijie Lin and his group for their zebrafish facility, Dr Pouya Faridi and Prof Antony Purcell for proteomic facilities and data analyses, and Hannah Kelly and Prof Stephen Kent for assistance with flow cytometry. I appreciate the support and advice from Dr Kevin McPeak, my former supervisor at EHT Zurich, Dr Karen McConologue, my inspiring outreach mentor and Dr Natalie Jones for unique leadership opportunities. Faculty Graduate Research is acknowledged for their financial support and scholarship.

Last but not least, I would like to express my profound gratitude to my beloved parents, and my husband, Pouya, for their unconditional support and continuous encouragement.

Chapter 1

Introduction

1. Introduction

Molecular self-assembly, as a result of electrostatic interaction, hydrogen bonding and π–π stacking, is of central importance to biology. To reach desired configuration, structure and function, a delicate balance of forces in polypeptide chains and between the polypeptides and surrounding molecules is required.[1,2] As a result of these interactions, molecular self-assembly of the polypeptide can proceed spontaneously, through cradle to grave of the cell. This biophysical phenomenon plays a significant role in the origin of a wide range of diseases.[3-5] In the cell, molecular self-assembly is exemplified by the configuration of the lipid bilayer membrane, the architecture of DNA and histones into chromatin, or the polymerisation of tubulins and actins into microtubules and actin filaments.[6] During the folding process, reaching the lowest free energy is a deciding factor in forming proper final structure of the peptide along different pathways on the energy landscape. The conformational plasticity of the structures allows a protein to function properly, but at the same time can result in protein malfunction and diseases.[1,2,6,7]As part of biomolecular self-assembly, proteins and peptides, the key elements of living systems, undergo self-organisation and self-replication through controlled molecular interactions, which begin as aggregation of monomeric peptides and proteins to toxic oligomers, followed by protofibrils and amyloid fibrils and plaques.[8] Spontaneous conversion of soluble proteins or their fragments into cross-beta sheets of fibrils leads to protein "misfolding diseases", or the so-called "amyloid diseases", such as type 2 diabetes (T2D), Alzheimer's disease (AD), Parkinson's disease (PD), Huntington's disease (HD), Prions, arthritis, and atherosclerosis.[2] The pathologies of these disorders are in strong association with the self-assembly of amyloid proteins such as amyloid-β (Aβ), tau, α-synuclein (αS) and human islet polypeptide (IAPP) (Fig. 1). In general, protein fibrillation starts with a lag phase, followed by an elongation phase where proteins assemble into toxic oligomers and aggregates. The final stage is formation of mature tube-like helical fibrils comprising β-sheet structures in

the saturation phase.[6,9] Although the molecular mechanism of the monomeric to fibrillar form transition is poorly understood, it has been shown that the oligomers, instead of the fibrillar deposits, are the most toxic species derived from the intermediate aggregation pathway.[6,10-12]

In vitro, the development of amyloids and plaques depends on the type of the polypeptide, which can occur within hours or days. However, *in vivo*, fibrillar formation in the brain or pancreatic islets often takes decades. The important factors in determining the lengths of the lag time and rate of fibrillar growth include the initial concentration of the polypeptide, pH, seeding molecules, and catalysing surfaces.[13,14]

My PhD research concerned the mitigation of amyloid protein aggregation, such as Aβ and IAPP amyloidisis associated with AD and T2D. My first study implicated a close connection between Aβ amyloidosis and immunopathology in AD. My two separate studies demonstrated the potential of employing nanotechnologies against the mesoscopic enantioselectivity of amyloid proteins and their associated toxicity in an embryonic zebrafish model, and potency of NPs in mitigating protein dysregulation in pancreatic beta cells exposed to toxic IAPP species.

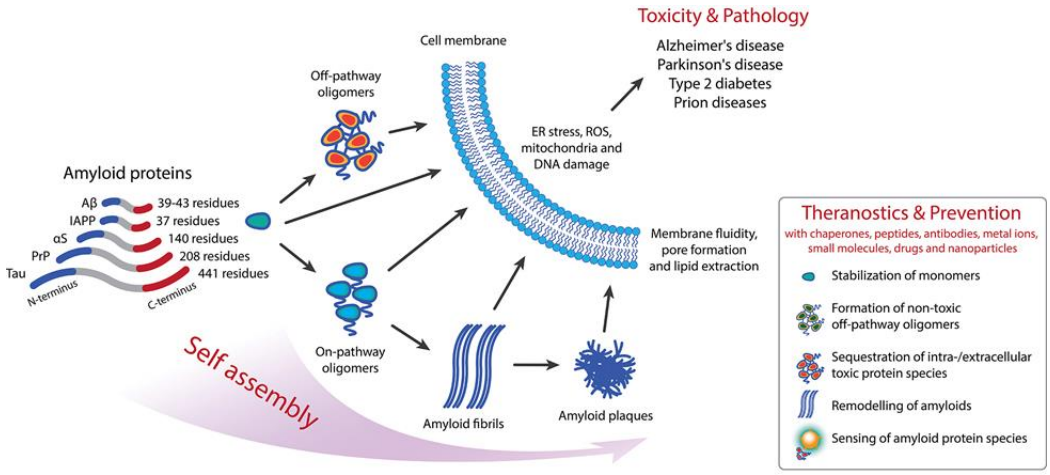

Figure 1. Fibrillation mechanisms of amyloid proteins and their pathological implications for amyloid diseases. The association of self-assembled toxic peptide structures with cell membranes result in ER (endoplasmic reticulum) stress, ROS (reactive oxygen species) production, apoptosis and cell degeneration. Aβ: amyloid-beta; IAPP: islet amyloid polypeptide; αS: alpha-synuclein; PrP: prion protein. Reproduced with permission from Ke et al.[6]

1.1. Amyloid diseases

1.1.1. Alzheimer's disease (AD)

Alzheimer's disease (AD) is a neurodegenerative disorder and the main cause of dementia. With the aging global population, this disease has become an epidemic grown substantially over the years in burden but with no cure available.[15-17] The underlying pathology of AD is the loss of synapses and neurons in the cerebral cortex and subcortical regions, which leads to generalised atrophy of the brain in the temporal and parietal lobes, frontal cortex and cingulate gyrus. Studies have shown degenerative atrophy in the nuclei of the brain stem and locus coeruleus. AD is also associated with mitochondrial abnormalities, unbalanced cell cycle and inflammatory reactions.[18,19] Granulovacuolar degeneration in the hippocampus and atrophic degeneration in the brain stem have been reported via magnetic resonance imaging and positron emission tomography in AD patients.[20] In addition, metals during exposure may play as seeds or nucleation cores to facilitate the formation of amyloid deposits.[21-23] Although many studies have been conducted on AD, the aetiology of the disease remains controversial. It has been proved that the high level of Aβ is a main cause of AD.[24] These observations on the neurotoxicity effect of fibrillar Aβ and its role for the pathogenesis in AD led to the 'amyloid hypothesis', which has been a main paradigm guiding research on AD during the past decades. In this case, precipitation of Aβ into plaques represents the presence of toxins in the brain.[25-27] Amyloid precursor protein (APP) is expressed in various tissues as an essential membrane protein, and is concentrated in the synapses of the brain as a regulator of synapse formation. Sequential cleavages of APP by β-secretase and then by γ-secretase lead to the production of Aβ,[28,29] which appears in two major forms of Aβ1-40 and Aβ1-42 (Fig.2). Compared to Aβ1-40, the two additional amino acids of isoleucine and alanine at the C-terminus of Aβ1-42 result in a more hydrophobic structure and, therefore, a higher tendency in aggregation and significantly higher cytotoxicity.[6] Secretion of Aβ into extracellular fluids may lead to self-

aggregation of the peptide.[26] The peptide can then diffuse into the cerebrospinal fluid or coalesce as a diffuse plaque. Aggregation of disordered proteins increases β-sheet secondary structure and alter the balance between the peptide production and clearance. Accumulation of Aβ and phosphorylated tau in the brain are associated with many neurodegenerative diseases, including AD.[25,30]

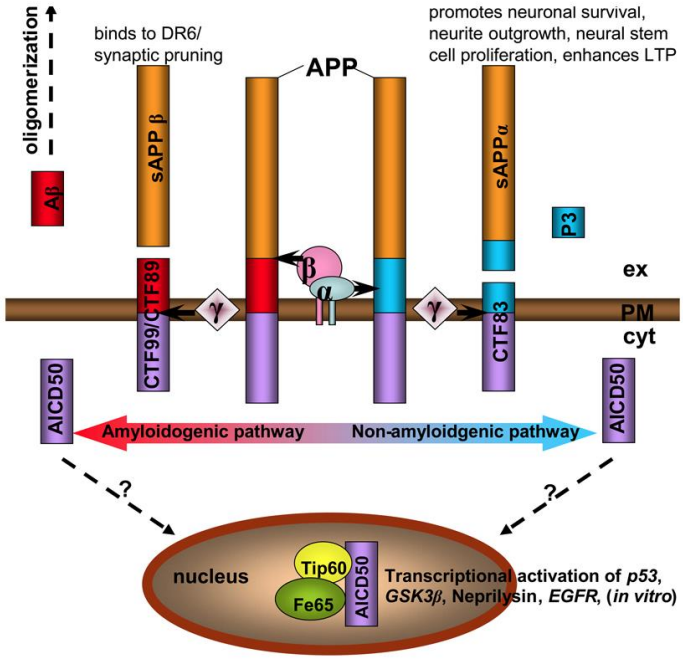

Figure 2. Aβ results from cleavage of amyloid precursor protein (APP) by β and γ-secretases. The process related to non-amyloidogenic APP (blue panel) cleaved by α and γ-secretases leads to formation of sAPPα and C-terminal fragments of CTF 83, p3 and AICD50. The process in association with amyloidogenic APP pathway (red panel) results in sAPPβ, C-terminal fragments of CTF 99, CTF 89 and Aβs. Fibrillation of Aβ (left side) is related to AD pathology. Reproduced with permission from Chow et al.[31]

Accumulation of Aβ in the brain induces loss of neurons, synapses and microglia. This phenomenon is also associated with compromised blood-brain barrier and function of choroid plexus, as well as hepatic failure. Interestingly, recent research strongly emphasises the role of neuroinflammation in the pathogeneses of AD and other neurodegenerative conditions. The involvement of immune system is certainly not limited to neuroinflammation in the brain but also generation of immune signals outside the brain per clinical studies.[32]

1.1.2. Type 2 Diabetes Mellitus (T2DM)

Diabetes as a group of metabolic diseases is characterized by hyperglycemia, resulting from autoimmune destruction of pancreatic β-cells with consequent insulin deficiency, which is due to either a decrease in insulin secretion or increased cell resistance to insulin. The chronic hyperglycemia of diabetes is known as one of the main causes of the disease and is associated with long-term dysfunction and failure of organs, especially the eyes (blurred vision or blindness), kidneys, myocardial infarction, nerves, blood vessels, high cardiovascular risk and stroke. In general, there are two primary forms of diabetes: type 1 diabetes mellitus (T1DM) with autoimmune destruction of β-cells in insulin secretion, and type 2 diabetes mellitus (T2DM) with insulin resistance followed by metabolic syndromes such as obesity, high blood pressure, high blood sugar and high serum triglycerides. While T1DM accounts for 5–10% of those with diabetes, T2DM is a global epidemic plaguing 90-95% of all diabetic patients, and the burden of the disease is projected to reach 439 million by 2030.[33-36] Genetic and environmental factors together play important roles in insulin resistance and β-cell dysfunction associated with T2DM. Peripheral insulin resistance, compensatory β-cell expansion and hyperinsulinaemia result in a higher demand for insulin, known as the core factor of T2DM.[37,38] Insulin deficiency gradually leads to gluco-toxicity of β-cells and, consequently, dysfunction and mass reduction of β-cells due to apoptosis (Fig. 3).[38,39]

Obese euglycaemic people require increased insulin secretion to maintain normal glucose tolerance (euglycaemic hyperinsulinaemia), due to the result of having ~30% reduced insulin sensitivity. Over time, this may be followed by a further drop in insulin sensitivity with no association to compensatory hyperinsulinemia and, therefore, excess of blood glucose concentration. In this situation, β-cells are no longer able to secrete enough insulin to trigger hyperglycaemia.[40]

Experimental results on β-cells from patients with T2DM offer evidence on the presence of aggregates and plaques of human islet amyloid polypeptide (IAPP, or amylin), which is co-

secreted with insulin from pancreatic β-cells.[41-43] The islets in T2DM are characterized by the occurrence of what is referred to as amyloid, per the "amyloid hypothesis". The term amyloid is associated with abnormal (mostly) extracellular composition of proteins, consisting of insoluble aggregation of monomers arranged in a β-sheet like architecture.[43]

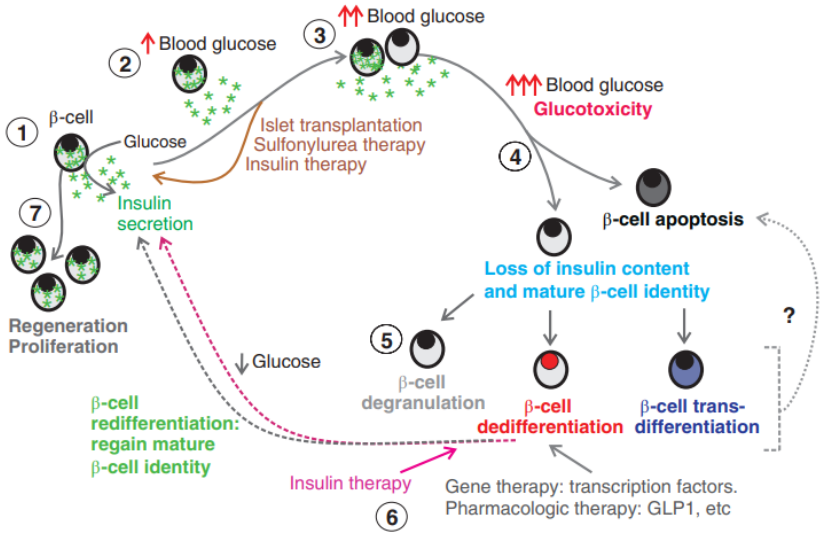

Figure 3. (1) Insulin secretion of β-cells in response to glucose. (2) Insufficient insulin leads to stress in β-cells. (3) In the case of insufficient insulin and high blood glucose, gluco-toxicity induces changes in β-cells. (4) Rising glucose level alters terminally differentiated state and causes apoptosis. (5) Cell degranulation, de-differentiation and transdifferentiation are induced by insulin deficiency. (6) Intensive insulin therapy relieves gluco-toxicity or gene therapy to restore transcription factors. (7) Under specific physiological conditions, proliferation and growth of the cells occur. Reproduced with permission from Remedi et al.[38]

1.1.3. Linkage between T2DM and AD

There exists evidence on diabetes-related dementia. However, the causative relation of such connection is not well understood. Statistical analysis shows that the risks of eventually developing Alzheimer's dementia are higher in diabetic patients.[44-46] AD and T2DM share a significant number of biochemical and physiological pathways. Previous studies emphasised on the role of insulin in cell-growth, including neurons in the CNS in addition to regulation of blood sugar.[47] Besides obesity, other mechanisms such as insulin resistance, inflammatory cytokines, and oxidative stress may explain this connection,[48] with the hypothesis that

accumulating oligomeric IAPP in the cerebrovascular system and brain parenchyma of patients is causative to the onset of diabetes.[49]

Epidemiological studies show the effect of hyperglycemia on the aggregation of Aβ in the brain, resulting in oxidative stress, neuroinflammation, and, consequently, neurodegenerative diseases.[50] Hyperglycemia is a potential risk factor for AD development.

1.2. Pathological amyloid proteins

The word "amylon" was first used in 1834 to describe the waxy starch in plants. Later, the word "amyloid" was used to describe tissue deposits that can be stained like cellulose after exposure to iodine.[51] Amyloid is fibrillar aggregates of folded peptides and proteins via hydrophobic interaction, π-π stacking and hydrogen bonding, assuming the ubiquitous cross β-sheet structure.[52]

1.2.1. Amyloid-beta (Aβ)

Aβ, as a transmembrane protein produced from APP, is expressed in the brain and tissues. The two major products of APP cleavage by β and γ secretases are Aβ1-40 and Aβ1-42, with Aβ1–42 *(DAEFRHDSGYEVHHQKLVFFAEDVGSNKGAIIGLMVGGVVIA)* entailing stronger neurotoxicity and faster aggregation.

Upon the production of Aβ by neurons, Aβ enters the blood and cerebrospinal fluid without any deposition due to the peptide clearance by the organism. Although the pathogenic role of the peptide is not entirely clear, it has been shown that the unbalancing rate of production, rate of clearance and, therefore, accumulation of soluble Aβ can damage synaptic junction and cause intracellular calcium homeostasis to give rise to neurovirulence and AD. The non-fibril structures of Aβ are known to be toxic to neurons[19,53], while three-dimensional arrangements of non amyloidogenic peptides often lead to proper functions such as storage, signalling,

enzymatic activity and sensing.[54] The accumulation of Aβ is a critical pathological phenomenon and a prime target to prevent and treat AD.

Studies by circular dichroism spectroscopy, Fourier-transform infrared spectroscopy, and X-ray powder diffraction microscopy have revealed structural transitions of Aβ, from disordered monomers to high-ordered dimeric and trimeric forms.[55] The oligomeric structures, known as the most neurotoxic, can be protofilaments with twisted structures around helical axes, which may be followed by hydrogen bonding along the β-sheet content. Amyloid fibrils possess significant β-sheets and less α-helical structures. Majority of oligomer species are disordered, with partially antiparallel β-structures. In comparison, majority of Aβ fibril structures consist of β-sheet components.[56] Atomic studies have shown that the amino acids of amyloid fibrils form β-strands orthogonal to the fibril axis, followed by β-sheets arranged parallel to the fibril axis towards the thermodynamic energy minima.[57] In this case, the hydrophobic parts of unfolded proteins are exposed. These conditions lead to formation of β-sheet structures through intermolecular hydrophobic interactions of proteins.[54,56] The Aβ peptide possessed two hydrophobic fragments at the 17–21 and 32-C terminus, both involved in the β-sheet conformation.[58]

One of the main factors in the aggregation of Aβ1–42 is pH.[59] The fibrillation of Aβ1–42 occurs at acidic pH as a result of the protonation of His6, His13 and His14,[60] while at higher pH of 9.5, uncharged Lys28 causes inhibition of the aggregation. It has been reported that other conditions besides pH, such as ionic strength, temperature, organic reagent and metal ions can each influence protein fibrillation.[54,61]

The role of metal ions in the aggregation of Aβ is well known. The balance and function of metal ions such as Zn^{2+} and Cu^{2+} which release from neurons in hippocampus play critical roles in mental activity.[62] Previous studies have revealed that associations of Aβ peptides with metals such as iron, zinc and copper induce oxidative stress in AD patients, resulting from metal

binding with Met35 and the N-terminal region during ROS production.[6,63] In other studies, release of metals such as zinc has been reported as a source of parenchymal and cerebrovascular amyloid in transgenic mice. In addition, unbalanced expression of APP and Aβ may damage the equilibrium of metals in the brain. While high level of metals like Cu in the brain could result in lower levels of Aβ and plaque formation in transgenic mice, expression of Aβ in the brain can sequester metals like Cu in the brain.[6] Although the pathway is not clear, it has been revealed that any imbalance in the critical level of metals in the brain would lead to the pathogenesis of AD.[23]

In recent years, advancements in methodologies and techniques have provided more information on the interaction of Aβ peptides and cell membrane, showing electrostatic and hydrophobic interactions as the main driving forces.[64] The lipid membrane interface as a potential nucleation site can alter the folding process of Aβ peptides.[65-67] The formation of random coil and helical structure of Aβ through its N-terminus binding with the membrane often serves as a start point of Aβ aggregation, leading to pore formation and membrane distruption.[68] Oligomeric structures are known as a major source of Aβ toxicity, manifested by the formation of β-barrel or prion-like structures in the cell membrane.[6]

1.2.1.1. Amyloid-beta and immune responses

Although much research has been focused on the toxicity mechanisms of Aβ, the involvement of immune systems in the pathogenesis of AD has been reported.[69,70] Neuronal inflammation and activation of innate immunity are also known as hallmarks of AD. Therefore, numerous clinical trials have been focused on developing vaccination for AD. Immunisation against Aβ has been shown as a successful AD therapeutic technique in murine models.[71] In the experiment by Marsh et al.,[70] genetic ablation of peripheral immune cell populations considerably suppressed amyloid pathogenesis, increased inflammation of nervous tissue, and caused disorders in microglial activation. In addition, the effect of IgG-producing B cell loss on

microglial phagocytosis malfunction, followed by a failure in proper Aβ deposition has been reported. In contrast, injection or transplantation of IgGs resulted in the reduction of Aβ pathology, validating the significant role of the immune system in AD.[70] Another evidence on the association of immune systems with AD is the degradation of Aβ by microglia, and autoreactive T cells are involved in the peptide clearance.[72]

Experiments have shown the aggregation of tau and Aβ plaques in association with AD, leading to microgliosis and elevated cytokine production as part of neuroinflammation.[73-76] Cytokines are known to affect the production and metabolism of APP expressed in most neuronal and extraneuronal tissues.[72,77] Effects of interleukin-1 (IL-1) on stimulating amyloidogenic metabolites of APP, accumulation of cellular APP, and promotion of amyloidogenesis have been reported.[78-80] Interferon g (IFNg) is known as the inhibitor of APP production.[79] However, in interaction with tumor necrosis factor (TNF), IFNg raises the production of APP. Such changes in cytokines increase the secretion of APP and consequently the amount of Aβ in the culture medium.[72] In addition, specific receptors on microglia and monocytes in the brain are involved in the clearance of extracellular Aβ peptides through non-inflammatory phagocytosis or pro-inflammatory cytokine secretion.[69,72,81,82] As shown in Fig. 4, complement C3b can adhere to complement receptor 1 (CR1) of erythrocytes in human, known as a mechanism for the peripheral clearance of Aβ.[83]

In literature the measurements of Aβ in the blood have been reported as a way towards early diagnosis of AD.[84] However, the association of Aβ with immune cells, in the presence of plasma proteins, remains unclear.

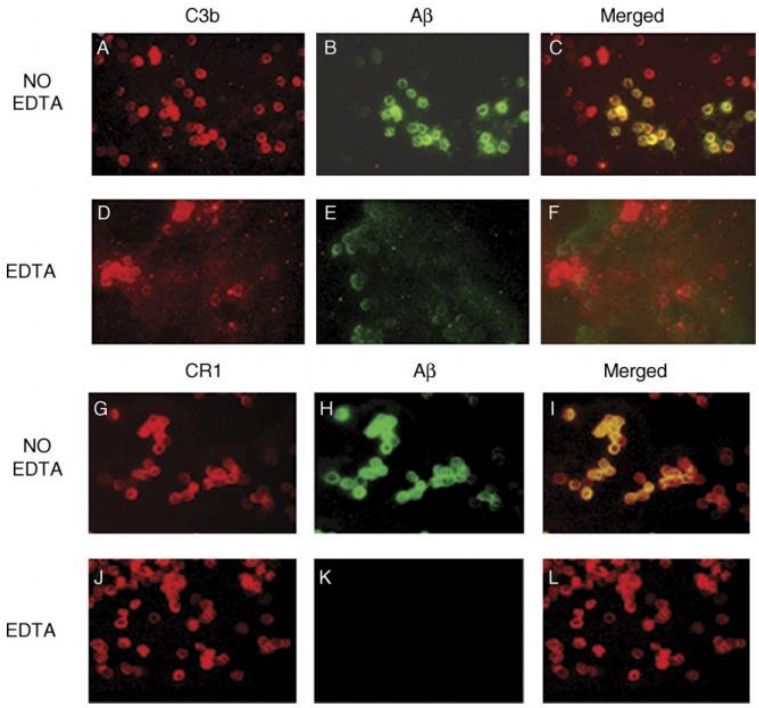

Figure 4. Interaction of Aβ42 with C3b and CR1 on erythrocytes after spiking blood samples with Aβ42, with and without EDTA. Reproduced with permission from Rogers et al.[83]

1.2.2. Human islet amyloid polypeptide (IAPP)

Human islet amyloid polypeptide (IAPP, a.k.a. amylin) is a peptide containing 37 amino acids (*KCNTATCATQRLANFLVHSSNNFGAILSSTNVGSNTY*) with a disulfide bridge between residues 2 and 7. IAPP is generated from a 67 amino acid precursor peptide, proIAPP, and is co-secreted with insulin by pancreatic β-cells to regulate glucose homeostasis.[85] IAPP also functions with other peptides, such as calcitonin and calcitonin gene-related peptides, in bone metabolism.[86]

IAPP is co-secreted with insulin inside the β-cell granules, at pH 5 and in high concentrations. Under these conditions, the His18 is protonated to fend off IAPP aggregation in pancreatic beta cell islets.[87] Therefore, IAPP acts as a synergistic partner of insulin and, through co-secretion,

controls the level of blood glucose.[6] At neutral pH, His18 becomes neutral. This condition has been cited as a cause of IAPP aggregation to render extracellular amyloid plaques.

Conversion of soluble proteins and peptides to insoluble amyloid fibrils leads to β-cell dysfunction, apoptosis and cell death. Several studies have indicated that β-cell failure in T2D correlates with the self-assembly and deposition of IAPP fibrillar plaques in the pancreatic islets. In T2D, insulin resistance leads to increment of insulin and concomitantly elevated IAPP production by β cells. Overexpression of IAPP may give rise to IAPP aggregation, which further evolves into amyloid fibrils while producing toxic species *en route*. (Fig. 5) In short, the toxicity of IAPP has been considered a main cause for the loss in function and mass of pancreatic islets.[88,89]

Due to the crucial need of designing potent therapeutics against amyloid diseases, many studies have been conducted to understand the structure, aggregation and toxicity of amyloid proteins. Various techniques, such as transmission electron microscopy (TEM) and atomic force microscopy (AFM), have been applied to investigate the structure of IAPP fibrils.[90-92] IAPP fibrils typically form left-handed coil structures with diameter of up to 20 nm and length of 0.1-10 μm. These fibrils are thermodynamically stable and may gradually develop amyloid plaques through hydrogen bonding.[88,93] At the mesoscopic scale, IAPP fibrils appear as ribbon-like structures. On the molecular scale, the β-sheets within the fibrils are formed by β-strand segments placed perpendicularly to the long fibril axis, linked by hydrogen bonds parallel to the fibril axis.[90] A handful of studies have detailed that oligomers and protofibrils, among all structures of IAPP aggregates, elicit the highest toxicity[94] through increased membrane porosity and fluidity, altered biometal concentration, ROS production, autophagy and apoptosis to damage the pancreas and evoke T2DM.[95-97]

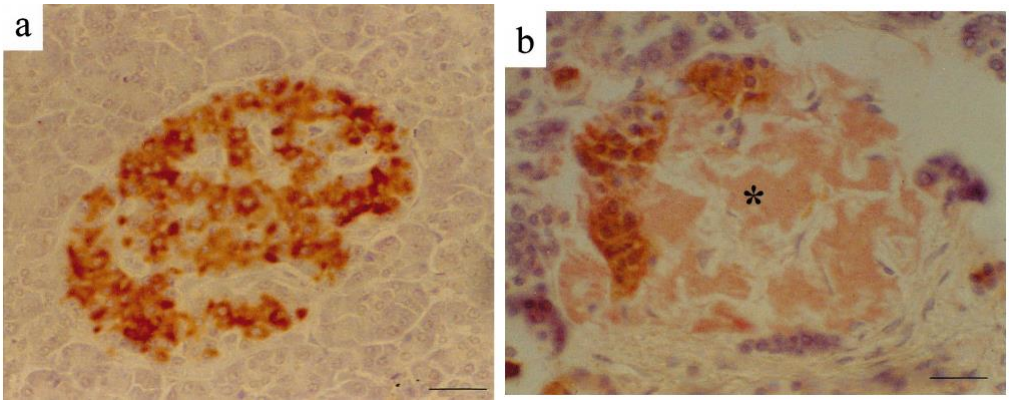

Figure 5. (a) A non-diabetic β-cells islet shows insulin (labelled in brown) covering more than 80% of the islet. (b) A diabetic β-cells islet shows insulin (brown) and amyloid protein (pink) with more than 50% coverage by amyloid protein. Scale bar: 20 μm. Reproduced with permission from Jaikaran et al.[98]

1.3. Nanoparticles for biomedicine

The Greek word nano means dwarf, which is now used to describe any material with at least one dimension on the scale of 1–100 nm.[99] The significant effect of size in the physicochemical properties and tunable surface properties make nanoparticles (NPs) a unique class of materials for biological and biomedical applications. Targeting a specific location in the body with small dosage and high specificity can be offered by NPs for drug delivery and theranostics.[100]

1.3.1. The protein corona

The physicochemical properties of NPs are significantly different from the same materials in bulk.[101] Nanomaterials possess much large surface areas with higher numbers of surface atoms, entailing greater adsorption and higher capacity in crossing the blood-brain barrier (BBB).[102]

The roles of NPs in immune response, vaccine development[103] or modification of protein fibrillation in amyloidosis have been confirmed.[104] However, despite of the advantages of NPs in medicine and drug delivery, interfacing the engineered surface chemistry of NPs with biological systems remains a considerable challenge in terms of nanomedicine and nanosafety.[105] Adsorption of biomolecules to nanomaterial surfaces for surface energy minimisation[106] dictates cellular response to the NPs.[107] Adsorption of environmental proteins to NPs leads to adjustments to the native protein structure[108] and formation of a "protein corona''.[109,110] This phenomenon begins with the acquisition of a layer of highly abundant but loosely bound proteins, or the "soft" corona, which overtime is replaced by proteins of lower abundance but higher affinity, or the "hard" corona (Fig.6).[111-114]

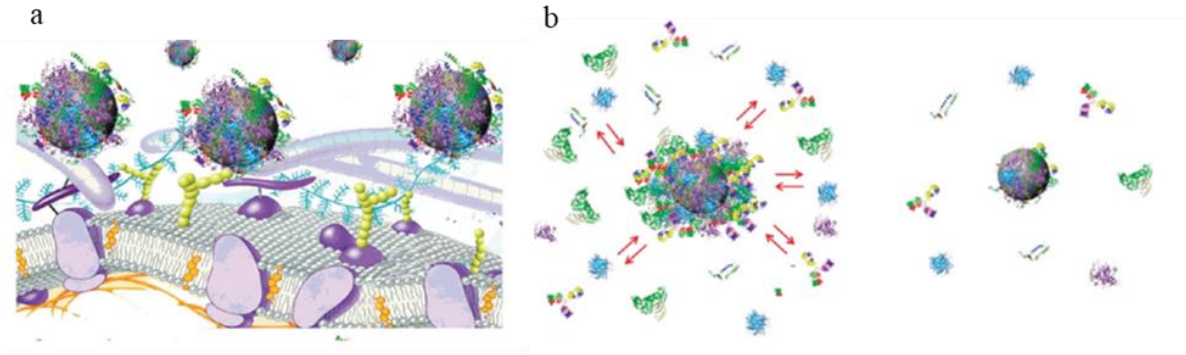

Figure 6. (a) Interaction of nanoparticles with cell membrane in biological environment. (b) Schematic of the NP-protein interaction in plasma where a core particle is covered with an outer layer of proteins forming the "soft" corona (red arrows on left). Stronger attraction of free proteins results in a "hard" protein corona. Reproduced with permission from Walkzyk et al.[112]

The NP-protein interaction is determined by a number of factors. One of the main factors is the correlation between the sizes of the proteins and the NPs. Protein would stretch to adjust to larger NPs. However, NPs with a significantly smaller size in comparison to proteins would lead to less significant changes in the protein structure due to the fewer amount interactions.[115] In addition to size, the surface charge of NPs plays a significant role in modifying the protein secondary structure. Gold NPs with various surface charges but similar properties adsorbed the same amount of bovine serum albumin. However, positively charged gold NPs interacted more with cell membranes, which led to a higher rate of cellular uptake than negatively charged gold

NPs.[108,116] TEM, dynamic light scattering (DLS), AFM and UV-Vis spectrophotometry documented the size effect in protein-NP interaction.[117,118] Exposure conditions including media composition, protein concentration, exposure time, temperature and pH of the biological fluid, plus the size, shape, surface charge, hydrophobicity and morphology of the NPs are all key factors in determining protein–NP interactions.[108]

NPs are promising candidates for drug delivery, as they possess the feasibility of shuttling through the BBB to target neurological, psychiatric and neurodegenerative disorders.[119] However, the effect of the protein corona in the interaction of NPs with the BBB and changes of corona post BBB translocation are unknown.[120] Higher stability of the protein corona in the brain compared to the corona in the blood has been reported by Cox. et al,[119] likely resulting from clearance/removal of some proteins on the blood side.[119] Despite challenges related to the protein corona, *in vivo* amyloidosis inhibition with nanomaterials has been demonstrated by a number of studies.[121,122]

NPs can impact cellular activities and provoke cell death through disruption to plasma membranes, ROS production, inflammation and mitochondrial and nuclear damage. Formation of the protein corona often renders the NPs more biocompatible to ameliorate immune response[123] and reduce cell damage induced by NPs. The protective effect of adsorbed proteins against cell damage induced by bare NPs has been investigated in a number of studies,[124,125] confirming enhanced biocompatibility.[108,126]

1.3.1.1. NP-amyloid protein interaction

Small molecules such as surfactants, copper or zinc ion chelators, polyphenols[127] such as epigallocatechin gallate (EGCG),[128] curcumin[129,130] and resveratrol[131] have been studied as inhibitors for the mitigation of protein aggregation.[132-134] Chemical modifications, including N-methylation utilizing β-sheet breaker (proline, D-peptides peptoid),[135,136] have been applied to improve the biocompatibility of the peptide inhibitors. NPs can significantly influence the

nucleation and aggregation of proteins via their strong interactions.[101,137] A summary of these effects by many NPs is shown in table 1.[102] Presence of proteins and NPs within the same biological environment gives rise to NP-protein and protein-protein interactions. NP-protein interaction may either result in acceleration of protein fibrillation, due to the accumulation of NPs around the protein, or inhibition of protein fibrillation due to isolation of proteins by their preferential binding to NPs.[138] Metal ions such as copper could shorten the lag time of Aβ fibrillation, due to their initiation of binding between the peptides. Here the presence of copper serves to increase the stability of peptide-peptide interaction.[139] The affinity of NPs-protein association is related to the surface chemistry and structure of the NPs.[140-142] For example, the protein corona around copolymer NPs is highly related to the hydrophobicity of the NP surface and exposure of their CH_3 groups to the environment. Apolipoproteins, specifically, show stronger interactions with NPs of greater hydrophobicity.[109,143] Copolymer particles, carbon nanotubes, cerium oxide particles and quantum dots, furthermore, have been applied to shorten the lag phase of the aggregation of human β2-microglobulin, exploiting the surface properties

Types of NPs	Results of NPs-Amyloid interactions
Au NPs	Amyloid- AuNPs complex is in unfavor of typical amyloid formation; GSH-covered AuNPs can disrupt amyloid aggregates; Peptide-AuNPs conjugates redissolve the deposits and inhibit the aggregation by applying MWs; Peptide-AuNPs activate microglial and help amyloid clearance;
Magnetic NPs	γ-Fe_2O_3 NPs selectively bind to and completely remove amyloid fibrils; SPIONs has a surface area dependent "dual" effect on amyloid fibrillization; Fluorinated magnetic core-shell NPs inhibit amyloid fibril formation;
Quantum dots	NAC capped CdTe QDs inhibit the fibrillization by quenching both nucleation and elongation process; TGA-stabilized CdTe NPs are similar with peptide inhibitors;
Dendrimers	PPI eliminates prion and cure infected cells; PAMAM shows potential against amyloid formation; GATG dendrimer reduces toxicity along with accelerated fibril formation process; Sialic acid conjugated dendrimer competes with Aβ for cell surface binding;
Polymeric NPs	NIPAM/BAM NPs retard/enhance fibrillization lying on protein stability; PolyA-FF-ME NPs inhibit Aβ fibrillization kinetics; PACA nanoparticulate platform inhibits amyloid aggregation and rescue toxicity;
Fullerenes	Fullerenes and derivatives inhibit amyloid aggregation and avoid cytotoxic effects;
Carbon nanotubes	CNTs inhibit amyloid fibrillization by destabilizing the β-sheet structure and evanishing proteins' natural propensity to collapse;
Graphene (oxide)	Graphene induces conformation transition and preferred adsorption of amyloid;
Bimolecular aggregates	KLVFF scaffold prevents Aβ aggregation into amyloid fibrils; Lipid-based NPs inhibit conformation transformation and reduce amyloid aggregation; CHP nanogels inhibit amyloid fibrils formation and suppress toxicity;

of the nanostructures.[144]

Table1. Effects of various NPs on amyloid protein fibrillation and their aggregation toxicity. Adapted with permission from Zhang et al.[102]

Towards amyloidosis inhibition, extensive studies have examined the interactions of silica NPs with amino acids.[145-147] Electrostatic interaction has been reported as the main binding force of spherical silica NPs or silica films with peptides and proteins.[148-151] Graphene quantum dots (GQDs) have been introduced as a potent inhibitor against the amyloidosis of IAPP and αS *in vivo*.[152,153] In another study, star polymer poly (2-hydroxyethyl acrylate) has been applied to accelerate the nucleation and elongation phases of IAPP fibrillation and reduction of IAPP toxicity as a result of depleted oligomer population.[154]

1.3.1.2. Chiral nanostructures in amyloidosis inhibition

Our left hand is the mirror image of our right hand. This phenomenon also exists in the world of biology and organic chemistry. In nature, many compounds, twisted protein fibrils or DNA appear in both forms of right-handed and left-handed. Such compounds are called "chiral" from the Greek word, cheir, which means the hand, and the mirror forms are called stereoisomers.[155-158]

The presence of chirality is prevalent, from physics and the pharmaceutical industry to drug design and biochemistry, from enantioselective catalysis to supramolecular assembly and protein folding. Chiral nanostructures have been applied such as nanosensors,[159] nanophotonics,[160] catalysis[161] and piezotronics systems.[162] Experimental results in drug enantioselectivity revealed that often just one of the enantiomers is effective, implicating chirality recognition as a strategy for drug design and treatment.

In biological environments, DNA mostly appears as right-handed double helices,[6,60] while IAPP fibrils exist mostly as left handed.[163] The effect of chiral nanostructures on the aggregation and fibrillation of chiral IAPP speices has rarely been exploited in the development of therapeutics associated with T2DM. Aβ fibrils show a dinstinct handness due to the inherent chiralities of α-helices and L-amino acids, and are sensitive to chiral environments as a result. This chirality may be utilised for designing an effective treatment of AD pathogenesis.[155,164] In

a previous study by Li et al.,[155] chiral molecules have been applied to selectively inhibit Aβ fibrillation.

Understanding the fundamental properties of amyloid structures, such as their chirality and their interactions with chiral NPs are crucial not only to gain a new insight into the biophysical and biochemcial aspects of amyloidosis and amyloid diseases, but also to the development of nanomedicine and bionanotechnology.[165]

1.4. Key techniques and model systems for the thesis

1.4.1. Commonly used techniques

1.4.1.1. For structural analysis

- ThT Kinetic Assay: The thioflavin T (ThT) dye is widely used to track and quantify protein aggregation and fibrillation both *in vitro* and *in vivo*. Amyloid fibrils can be readily detected in exposure to ThT dye, a small molecule which provides high fluorescence intensity upon binding to the surface grooves of amyloid structures through hydrophobic interaction and π-stacking.[166] Changes in ThT fluorescence intensity is known as an indicator of the β-sheet structure in amyloid fibrils.
- Fourier-transform infrared (FTIR) spectroscopy: FTIR spectroscopy is a well-known technique for structural characterizations of proteins and polypeptides, to provide molecular information for the identification of simple to complex bonds.
- Thermogravimetric analysis (TGA): TGA is a technique based on a thermal analysis of the mass of a sample over time, as water and organic constituents of a material gradually dissociate through heating.
- Zeta potential: From the Greek letter zeta (ζ), is widely used for the quantification of the surface charge of particles.

- Spectrofluorometry: For autofluorescent NPs, such as GQDs, the technique can offer information regarding quenching of the NP fluorescence upon binding with amyloid protein species.

1.4.1.2. Microscopy techniques

- Transmission electron microscopy (TEM): TEM is a commonly used imaging technique, which constructs images through the interference of electron beams transmitted through a sample, such as an inorganic material, or biomacromolecules and their complexes. Valuable information can be obtained about the sample morphology or mechanism of interaction between species. FiberApp, a statistical analysis tool based on the MATLAB platform, may be applied to extract parameters such as the width, pitch size, length, and height distribution of amyloid fibrils.[167]
- Scanning electron microscopy (SEM): SEM is another technique for imaging the structure and morphology of materials, including particles and peptides.
- Helium ion microscopy (HIM): HIM is an alternative imaging technique to SEM, based on focused ion beams. It overcomes challenges in SEM imaging of biological samples to avoid sample damage and provide high image contrast without surface metal coating.
- Confocal fluorescence microscopy: This optical technique has the advantages of sample sectioning and high signal-to-noise ratio, compared with conventional EPI fluorescence microscopy.

1.4.1.3. Cytotoxicity

- Cell culture and cell viability assay: *In vitro* experiments enable studies of biological responses to external factors in a more economical and convenient manner than *in vivo* animal studies. Here, to investigate the toxicities of NPs, peptides (IAPP and Aβ) and effects of NPs on peptide amyloidosis, pancreatic cell line (βTC-6) and neuronal cell line (SH-SY5Y cells) were cultured following proper protocols and viability assays were performed.

For the viability assays, treated cells were measured by a PerkinElmer Operetta system in a live cell chamber. Propidium iodide (PI) labelled dead cells, and cell viability was quantified by measuring cells which showed PI fluorescence relative to total cell count determined by a built-in bright-field mapping function of Harmony High-Content Imaging and Analysis software. MTT (3-(4,5-dimethylthiazol-2-yl)-2,5-diphenyltetrazolium bromide) assay was also performed as a complementary technique for the determination of cellular viability.

- Reactive oxygen species (ROS) assay: ROS are formed as natural byproducts of the metabolism of oxygen, and elevated production of ROS by biological systems under stress can result in apoptosis and cell death.[168] Here, ROS assay was performed to evaluate cell response to various peptides in the presence and absence of NP inhibitors.

In addition to the common techniques listed above, more specialised methods as described below were employed in the PhD project.

1.4.2. Proteomics and protein dysregulation analysis

Genomics and recently proteomics are modern profiling methods to identify novel genes and proteins related to complex diseases.[169] Recently, demands for more accurate analytical studies in protein biochemistry, drug development and biology have been rising significantly.[170,171] Proteomics is suited to provide new insights into the identification of proteins, and has been applied as a high-throughput technique to document the genes and proteins expressed in neurodegererative related disorders such as Glucoma[172] and AD-related neuronal tissues through enormous parallel analysis.[169] In previous studies proteomics has been applied for clinical management of people suffering from amyloidosis.[173] As yet, only a limited number of studies have so far investigated the adverse effects of amyloid proteins on interacellular protein and gene expressions upon neuronal cell exposure to Aβ.[174,175] With this approach, it was demonstrated that the induction of APP intracellular domain (AICD) resulted in higher gene expression in actin cytoskeleton such as α2-actin and transgelin. AICD exposed genes were

differentially regulated in the frontal cortex of AD patients compared with controls.[176] Among available information on the proteome of neuronal cells, the effects of Aβ on critical neuronal pathways and dysregulation in AD such as cell adhesion, vesicle trafficking, actin cytoskeleton dynamics and insulin signaling have been reported. Gene expression in human microglia was altered in brain tissues after exposure to the oligomeric structure of Aβ1-42.[174]

Compared with Aβ, little is known about the proteome of pancreatic β-cells and intracellular protein expression upon cell exposure to IAPP aggregation species.

Mass spectrometry (MS) is a powerful technique for the identification and quantification of protein species,[177-179] and was employed in this project to investigate the up/down regulation of pancreatic interacellular proteins upon exposure to IAPP species. MS was used to sequence proteins using magnetic fields and define protein by protein mass-to-charge ratio. Liquid chromatography–tandem mass spectrometry (LC–MS/MS) was used to analyse digested samples.

1.4.3. Blood assay and localised surface plasmon resonance

The association of AD with neuroinflammation, in direct relation to peripheral immune cells is well established.[180] There is evidence in literature implicating the interaction of senile Aβ plaques and microglia.[181,182] and secretion of proinflammatory components such as IL-1β and TNF upon Aβ exposure.[183,184] In addition, changes in Aβ in the blood of early-stage AD patients have been reported.[185,186] However, the blood consists of various cell types immersed in more than 3,700 different types of plasma proteins and other biomolecules.[187] The hydrophobic structure of Aβ can result in binding of the peptide to plasma proteins and blood cell membranes.[83,84,188,189] The interaction of free Aβ and plasma proteins may lead to the formation of the protein corona. This phenomenon affects the interaction of Aβ with cell membranes and consequently alters cytotoxicity, cytokine secretion and consequently, immune response. In addition to the protein corona, exposure to various Aβ structures may result in different immune

responses. As an example, changes in hagocytic responses of microglia have been reported upon their exposure to soluble oligomers or fibrillar plaques.[184,190]

Localized surface plasmon resonance (LSPR) is a state-of-the-art technique for achieving fast, stable, label-free, real-time detection of biological samples and components, including cytokines. In this technique the surface binding of a biological sample causes shifts in the absorbtion and scattering patterns of a gold NP-coated substrate, serving as a reporter on cell response to protein aggregation, among other phenomena.[191,192]

In this study, the roles of plasma protein corona on immune cell responses to Aβ oligomers and fibrils were revealed using a blood assay. A microfluidic-based LSPR platform was applied to characterise the cytokine secretion of blood cells upon their exposure to Aβ structures.

1.4.4. Zebrafish model in amyloidosis

The zebrafish (*Danio rerio*) was first employed as an animal model in the 1980s. According to zebrafish and human gene comparision, more than 70% of human genome and around 82% of disease-related genome have at least one orthologue gene in zebrafish. Also, 47% of human genome have a one-to-one relationship with a zebrafish orthologue.[193] Compared to *in vitro* experiments, zebrafish as a multicellular organism provides much needed biological complexity unavailable from cell lines. Robust reproductivity as well as high optical transparency are other advantages of the zebrafish model, especially suited for toxicity studies. The rapid development of zebrafish from the embroynic to adult stages offers advantages for drug screening and biodistribution studies.[194-196] Furthermore, easy manipulation of multiple genes is another advantage of zebrafish over rodent models.[197] Accordingly, the last few years have witnessed a significant growth of the zebrafish model for the characterisation of pharmaceuticals and therapeutics targeting metabolic diseases.[198,199] Diabetic zebrafish models

have been employed to study the therapeutics for T2DM.[198,200] Other studies have involved the zebrafish model for the investigation of neurodegenerative diseases.[201]

Despite the significant differences between the human and the zebrafish brain, behavioral tests on zebrafish have confirmed the value of using the zebrafish model for studying neurological disorders.[195] Rink et al. showed that the ventral telencephalon in zebrafish is related to striatum in humans.[202] Various orthologs of genes related to PD, such as parkin, pink1, dj-1 and lrrk2 have been found in zebrafish. The Parkin gene, a common autosomal recessive mutation in PD, in zebrafish shows 62% and up to 92% similarities in identification and function compared with human.[203] Both human and zebrafish Parkin are expressed during development and in adult tissues and both result in gene dysregulation through mitochondrial stress.[204]

The early stage of AD is related to mutation of three genes correlated with Aβ proteolysis in human – Aβ precursor protein (APP), presenilin 1 (PSEN1), and presenilin 2 (PSEN2). In zebrafish, the genes appa and appb are reported as similar to human APP, and can be expressed in the telencephalon, the ventral diencephalon, the trigeminal ganglia, or the posterior lateral line ganglia.[205] Similarities of human with zebrafish in PSEN1 and PSEN2 provide an opportunity for the investigation of presenilin function related to AD.[206] Expression of Aβ, APP, and γ secretase components including PSENEN37, NCTN38 and APH1b37 has been reported for zebrafish during development,[197] and dysregulation or imbalance in these proteins may lead to neurological disorders.[201,207,208] Mutant human tau protein in a zebrafish model was used as a primary indicator of AD.[209]

In general, these genetic similarities between zebrafish and human rationalise a wide range of applications of the zebrafish model for the study of the pathologies and therapeutic development of human neurodegenerative and metabolic diseases.

References

1 Dill, K. A. Polymer principles and protein folding. *Protein science : a publication of the Protein Society* **8**, 1166-1180, 1999.

2 Murphy, R. M., Tsai, A. M. & SpringerLink. *Misbehaving proteins : protein (mis)folding, aggregation, and stability*. 2006.

3 Lashuel, H. A., LaBrenz, S. R., Woo, L., Serpell, L. C. & Kelly, J. W. Protofilaments, Filaments, Ribbons, and Fibrils from Peptidomimetic Self-Assembly: Implications for Amyloid Fibril Formation and Materials Science. *Journal of the American Chemical Society* **122**, 5262-5277, 2000.

4 Yamada, K. A. Modulating excitatory synaptic neurotransmission: potential treatment for neurological disease? *Neurobiology of disease* **5**, 67-80, 1998.

5 Davies, R. P. W. *et al.* in *Advances in Chemical Engineering* **35**, 11-43, 2009

6 Ke, P. C. *et al.* Implications of peptide assemblies in amyloid diseases. *Chemical Society reviews* **46**, 6492-6531, 2017.

7 Chiti, F. & Dobson, C. M. Protein Misfolding, Amyloid Formation, and Human Disease: A Summary of Progress Over the Last Decade. *Annual review of biochemistry* **86**, 27-68, 2017.

8 Vendruscolo, M., Zurdo, J., MacPhee, C. E. & Dobson, C. M. Protein folding and misfolding: a paradigm of self-assembly and regulation in complex biological systems. *Philosophical transactions. Series A, Mathematical, physical, and engineering sciences* **361**, 1205-1222, 2003.

9 Dobson, C. M. Protein folding and misfolding. *Nature* **426**, 884-890, 2003.

10 Bucciantini, M. *et al.* Inherent toxicity of aggregates implies a common mechanism for protein misfolding diseases. *Nature* **416**, 507-511, 2002.

11 Gregersen, N., Bross, P., Vang, S. & Christensen, J. H. Protein Misfolding and Human Disease. *Annual Review of Genomics and Human Genetics* **7**, 103-124, 2006.

12 Mukai, H. *et al.* Formation of morphologically similar globular aggregates from diverse aggregation-prone proteins in mammalian cells. *Proceedings of the National Academy of Sciences of the United States of America* **102**, 10887-10892, 2005.

13 Lee, C.-C., Nayak, A., Sethuraman, A., Belfort, G. & McRae, G. J. A Three-Stage Kinetic Model of Amyloid Fibrillation. *Biophysical journal* **92**, 3448-3458, 2007.

14 Hartl, F. U. & Hayer-Hartl, M. Converging concepts of protein folding in vitro and in vivo. *Nature Structural & Molecular Biology* **16**, 574-581, 2009.

15 Weller, J. & Budson, A. Current understanding of Alzheimer's disease diagnosis and treatment **7**, 1161, 2018.

16 Bondi, M. W., Edmonds, E. C. & Salmon, D. P. Alzheimer's Disease: Past, Present, and Future. *Journal of the International Neuropsychological Society : JINS* **23**, 818-831, 2017.

17 Richards, S. S. & Hendrie, H. C. Diagnosis, management, and treatment of Alzheimer disease: a guide for the internist. *Archives of internal medicine* **159**, 789-798, 1999.

18 Kandimalla, R. & Reddy, P. H. Therapeutics of Neurotransmitters in Alzheimer's Disease. *Journal of Alzheimer's disease : JAD* **57**, 1049-1069, 2017.

19 Chen, Y.-G. Research Progress in the Pathogenesis of Alzheimer's Disease. *Chin Med J (Engl)* **131**, 1618-1624, 2018.

20 Kohler, C. Granulovacuolar degeneration: a neurodegenerative change that accompanies tau pathology. *Acta neuropathologica* **132**, 339-359, 2016.

21 Turner, P. R., O'Connor, K., Tate, W. P. & Abraham, W. C. Roles of amyloid precursor protein and its fragments in regulating neural activity, plasticity and memory. *Progress in neurobiology* **70**, 1-32, 2003.

22 Moir, R. D., Lathe, R. & Tanzi, R. E. The antimicrobial protection hypothesis of Alzheimer's disease. *Alzheimer's & dementia : the journal of the Alzheimer's Association* **14**, 1602-1614, 2018.

23 Maynard, C. J., Bush, A. I., Masters, C. L., Cappai, R. & Li, Q. X. Metals and amyloid-beta in Alzheimer's disease. *International journal of experimental pathology* **86**, 147-159, 2005.

24 Shankar, G. M. *et al.* Natural Oligomers of the Alzheimer Amyloid-β Protein Induce Reversible Synapse Loss by Modulating an NMDA-Type Glutamate Receptor-Dependent Signaling Pathway. *The Journal of Neuroscience* **27**, 2866, 2007.

25 Zolezzi, J. M., Bastías-Candia, S., Santos, M. J. & Inestrosa, N. C. Alzheimer's disease: relevant molecular and physiopathological events affecting amyloid-β brain balance and the putative role of PPARs. *Front Aging Neurosci* **6**, 176-176, 2014.

26 Robinson, S. R. & Bishop, G. M. Abeta as a bioflocculant: implications for the amyloid hypothesis of Alzheimer's disease. *Neurobiology of aging* **23**, 1051-1072, 2002.

27 Selkoe, D. J. Alzheimer's disease: genes, proteins, and therapy. *Physiol Rev* **81**, 741-766, 2001.

28 Hardy, J. & Selkoe, D. J. The amyloid hypothesis of Alzheimer's disease: progress and problems on the road to therapeutics. *Science (New York, N.Y.)* **297**, 353-356, 2002.

29 Zhang, Y. W., Thompson, R., Zhang, H. & Xu, H. APP processing in Alzheimer's disease. *Molecular brain* **4**, 3, 2011.

30 Ballard, C. *et al.* Alzheimer's disease. *Lancet (London, England)* **377**, 1019-1031, 2011.

31 Chow, V. W., Mattson, M. P., Wong, P. C. & Gleichmann, M. An overview of APP processing enzymes and products. *Neuromolecular Med* **12**, 1-12, 2010.

32 Cao, W. & Zheng, H. Peripheral immune system in aging and Alzheimer's disease. *Mol Neurodegener* **13**, 51, 2018.

33 Wu, Y., Ding, Y., Tanaka, Y. & Zhang, W. Risk factors contributing to type 2 diabetes and recent advances in the treatment and prevention. *International journal of medical sciences* **11**, 1185-1200, 2014.

34 Almeida, C. & Cruz, R. Diabetes Mellitus II an Epidemic of the 21st Century: Therapeutic Challenges. *European Journal of Public Health* **29**, 2019.

35 American Diabetes, A. Diagnosis and classification of diabetes mellitus. *Diabetes Care* **33 Suppl 1**, S62-S69, 2010.

36 Tuomi, T. *et al.* The many faces of diabetes: a disease with increasing heterogeneity. *Lancet (London, England)* **383**, 1084-1094, 2014.

37 Heit, J. J. *et al.* Calcineurin/NFAT signalling regulates pancreatic beta-cell growth and function. *Nature* **443**, 345-349, 2006.

38 Remedi, M. S. & Emfinger, C. Pancreatic beta-cell identity in diabetes. *Diabetes, obesity & metabolism* **18 Suppl 1**, 110-116, 2016.

39 Butler, A. E. *et al.* Beta-cell deficit and increased beta-cell apoptosis in humans with type 2 diabetes. *Diabetes* **52**, 102-110, 2003.

40 Zaccardi, F., Webb, D. R., Yates, T. & Davies, M. J. Pathophysiology of type 1 and type 2 diabetes mellitus: a 90-year perspective. *Postgraduate medical journal* **92**, 63-69, doi:10.1136/postgradmedj-2015-133281, 2016.

41 Hoppener, J. W., Ahren, B. & Lips, C. J. Islet amyloid and type 2 diabetes mellitus. *The New England journal of medicine* **343**, 411-419, 2000.

42 DeToma, A. S., Salamekh, S., Ramamoorthy, A. & Lim, M. H. Misfolded proteins in Alzheimer's disease and type II diabetes. *Chemical Society reviews* **41**, 608-621, 2012.

43 Haataja, L., Gurlo, T., Huang, C. J. & Butler, P. C. Islet amyloid in type 2 diabetes, and the toxic oligomer hypothesis. *Endocrine reviews* **29**, 303-316, 2008.

44 Wang, C. Y., Neil, D. L. & Home, P. 2020 vision - An overview of prospects for diabetes management and prevention in the next decade. *Diabetes research and clinical practice* **143**, 101-112, 2018.

45 Brookmeyer, R., Abdalla, N., Kawas, C. H. & Corrada, M. M. Forecasting the prevalence of preclinical and clinical Alzheimer's disease in the United States. *Alzheimer's & dementia : the journal of the Alzheimer's Association* **14**, 121-129, 2018.

46 Weuve, J., Hebert, L. E., Scherr, P. A. & Evans, D. A. Prevalence of Alzheimer disease in US states. *Epidemiology (Cambridge, Mass.)* **26**, 4-6, 2015.

47 Li, L. & Holscher, C. Common pathological processes in Alzheimer disease and type 2 diabetes: a review. *Brain research reviews* **56**, 384-402, 2007.

48 Haan, M. N. Therapy Insight: type 2 diabetes mellitus and the risk of late-onset Alzheimer's disease. *Nature clinical practice. Neurology* **2**, 159-166, 2006.

49 Jackson, K. *et al.* Amylin deposition in the brain: A second amyloid in Alzheimer disease? *Annals of neurology* **74**, 517-526, 2013.

50 Lee, H. J. *et al.* Diabetes and Alzheimer's Disease: Mechanisms and Nutritional Aspects. *Clinical nutrition research* **7**, 229-240, 2018.

51 Baker, K. R. & Rice, L. The amyloidoses: clinical features, diagnosis and treatment. *Methodist Debakey Cardiovasc J* **8**, 3-7, 2012.

52 Lednev, I. K. Amyloid fibrils: the eighth wonder of the world in protein folding and aggregation. *Biophysical journal* **106**, 1433-1435, 2014.

53 Yankner, B. A., Duffy, L. K. & Kirschner, D. A. Neurotrophic and neurotoxic effects of amyloid beta protein: reversal by tachykinin neuropeptides. *Science (New York, N.Y.)* **250**, 279-282, 1990.

54 Wei, G. *et al.* Self-assembling peptide and protein amyloids: from structure to tailored function in nanotechnology. *Chemical Society Reviews* **46**, 4661-4708, 2017.

55 Ono, K., Condron, M. M. & Teplow, D. B. Structure-neurotoxicity relationships of amyloid beta-protein oligomers. *Proceedings of the National Academy of Sciences of the United States of America* **106**, 14745-14750, 2009.

56 Stroud, J. C., Liu, C., Teng, P. K. & Eisenberg, D. Toxic fibrillar oligomers of amyloid-beta have cross-beta structure. *Proceedings of the National Academy of Sciences of the United States of America* **109**, 7717-7722, 2012.

57 Petkova, A. T. *et al.* A structural model for Alzheimer's beta -amyloid fibrils based on experimental constraints from solid state NMR. *Proc Natl Acad Sci U S A* **99**, 16742-16747, 2002.

58 Ahmed, M. *et al.* Structural conversion of neurotoxic amyloid-beta(1-42) oligomers to fibrils. *Nat Struct Mol Biol* **17**, 561-567, 2010.

59 Kobayashi, S. *et al.* Dependence pH and proposed mechanism for aggregation of Alzheimer's disease-related amyloid-β(1–42) protein. *Journal of Molecular Structure* **1094**, 109-117, 2015.

60 Ke, P. C. *et al.* Implications of peptide assemblies in amyloid diseases. *Chemical Society reviews*, **46**, 6492-6531, 2017.

61 Carrotta, R., Manno, M., Bulone, D., Martorana, V. & San Biagio, P. L. Protofibril formation of amyloid beta-protein at low pH via a non-cooperative elongation mechanism. *The Journal of biological chemistry* **280**, 30001-30008, 2005.

62 Tamano, H. & Takeda, A. Is interaction of amyloid beta-peptides with metals involved in cognitive activity? *Metallomics : integrated biometal science* **7**, 1205-1212, 2015.

63 Bush, A. I. *et al.* Rapid induction of Alzheimer A beta amyloid formation by zinc. *Science (New York, N.Y.)* **265**, 1464-1467, 1994.

64 Niu, Z., Zhang, Z., Zhao, W. & Yang, J. Interactions between amyloid β peptide and lipid membranes. *Biochimica et Biophysica Acta (BBA) - Biomembranes* **1860**, 1663-1669, 2018.

65 Aisenbrey, C. *et al.* How is protein aggregation in amyloidogenic diseases modulated by biological membranes? *European biophysics journal : EBJ* **37**, 247-255, 2008.

66 Bystrom, R. *et al.* Disordered proteins: biological membranes as two-dimensional aggregation matrices. *Cell biochemistry and biophysics* **52**, 175-189, 2008.

67 Wong, P. T. *et al.* Amyloid-beta membrane binding and permeabilization are distinct processes influenced separately by membrane charge and fluidity. *Journal of molecular biology* **386**, 81-96, 2009.

68 Korshavn, K. J., Bhunia, A., Lim, M. H. & Ramamoorthy, A. Amyloid-beta adopts a conserved, partially folded structure upon binding to zwitterionic lipid bilayers prior to amyloid formation. *Chemical communications (Cambridge, England)* **52**, 882-885, 2016.

69 Ramanathan, A., Nelson, A. R., Sagare, A. P. & Zlokovic, B. V. Impaired vascular-mediated clearance of brain amyloid beta in Alzheimer's disease: the role, regulation and restoration of LRP1. *Front Aging Neurosci* **7**, 136-136, 2015.

70 Marsh, S. E. *et al.* The adaptive immune system restrains Alzheimer's disease pathogenesis by modulating microglial function. *Proceedings of the National Academy of Sciences of the United States of America* **113**, E1316-1325, 2016.

71 Rosset, M. B., Lui, G., Dansokho, C., Chaigneau, T. & Dorothée, G. Vaccine-induced Aβ-specific CD8+ T cells do not trigger autoimmune neuroinflammation in a murine model of Alzheimer's disease. *J Neuroinflammation* **12**, 95-95, 2015.

72 Marx, F., Blasko, I., Pavelka, M. & Grubeck-Loebenstein, B. The possible role of the immune system in Alzheimer's disease. *Experimental gerontology* **33**, 871-881, 1998.

73 McAlpine, F. E. & Tansey, M. G. Neuroinflammation and tumor necrosis factor signaling in the pathophysiology of Alzheimer's disease. *Journal of inflammation research* **1**, 29-39, 2008.

74 Maier, M. *et al.* Complement C3 deficiency leads to accelerated amyloid beta plaque deposition and neurodegeneration and modulation of the microglia/macrophage phenotype in amyloid precursor protein transgenic mice. *The Journal of neuroscience : the official journal of the Society for Neuroscience* **28**, 6333-6341, 2008.

75 Wyss-Coray, T. & Rogers, J. Inflammation in Alzheimer disease-a brief review of the basic science and clinical literature. *Cold Spring Harbor perspectives in medicine* **2**, 2012.

76 Guillot-Sestier, M. V. & Town, T. Innate immunity in Alzheimer's disease: a complex affair. *CNS & neurological disorders drug targets* **12**, 593-607, 2013.

77 Seubert, P. *et al.* Isolation and quantification of soluble Alzheimer's β-peptide from biological fluids. *Nature* **359**, 325-327, 1992.

78 Vasilakos, J. P. *et al.* Interleukin-1β dissociates β-amyloid precursor protein and β-amyloid peptide secretion. *FEBS Letters* **354**, 289-292, 1994.

79 Schmitt, E., Blanquet, S. & Mechulam, Y. Structure of crystalline Escherichia coli methionyl-tRNA(f)Met formyltransferase: comparison with glycinamide ribonucleotide formyltransferase. *The EMBO journal* **15**, 4749-4758, 1996.

80 Wyss-Coray, T. *et al.* Amyloidogenic role of cytokine TGF-beta1 in transgenic mice and in Alzheimer's disease. *Nature* **389**, 603-606, 1997.

81 Rogers, J., Strohmeyer, R., Kovelowski, C. J. & Li, R. Microglia and inflammatory mechanisms in the clearance of amyloid beta peptide. *Glia* **40**, 260-269, 2002.

82 Wang, Z. T. *et al.* Association of lectin-like oxidized low density lipoprotein receptor 1 (OLR1) polymorphisms with late-onset Alzheimer disease in Han Chinese. *Ann Transl Med* **6**, 172, 2018.

83 Rogers, J. *et al.* Peripheral clearance of amyloid beta peptide by complement C3-dependent adherence to erythrocytes. *Neurobiol Aging* **27**, 1733-1739, 2006.

84 Pesini, P. *et al.* Reliable Measurements of the beta-Amyloid Pool in Blood Could Help in the Early Diagnosis of AD. *International journal of Alzheimer's disease* **2012**, 604141, 2012.

85 Yan, L. M., Tatarek-Nossol, M., Velkova, A., Kazantzis, A. & Kapurniotu, A. Design of a mimic of nonamyloidogenic and bioactive human islet amyloid polypeptide (IAPP) as nanomolar affinity inhibitor of IAPP cytotoxic fibrillogenesis. *Proceedings of the National Academy of Sciences of the United States of America* **103**, 2046-2051, 2006.

86 Naot, D. & Cornish, J. The role of peptides and receptors of the calcitonin family in the regulation of bone metabolism. *Bone* **43**, 813-818, 2008.

87 Khemtemourian, L., Domenech, E., Doux, J. P., Koorengevel, M. C. & Killian, J. A. Low pH acts as inhibitor of membrane damage induced by human islet amyloid polypeptide. *Journal of the American Chemical Society* **133**, 15598-15604, 2011.

88 Wiltzius, J. J., Sievers, S. A., Sawaya, M. R. & Eisenberg, D. Atomic structures of IAPP (amylin) fusions suggest a mechanism for fibrillation and the role of insulin in the process. *Protein science : a publication of the Protein Society* **18**, 1521-1530, 2009.

89 Zhang, X., St Clair, J. R., London, E. & Raleigh, D. P. Islet Amyloid Polypeptide Membrane Interactions: Effects of Membrane Composition. *Biochemistry* **56**, 376-390, 2017.

90 Luca, S., Yau, W. M., Leapman, R. & Tycko, R. Peptide conformation and supramolecular organization in amylin fibrils: constraints from solid-state NMR. *Biochemistry* **46**, 13505-13522, 2007.

91 Goldsbury, C., Kistler, J., Aebi, U., Arvinte, T. & Cooper, G. J. Watching amyloid fibrils grow by time-lapse atomic force microscopy. *Journal of molecular biology* **285**, 33-39, 1999.

92 Goldsbury, C. S. *et al.* Polymorphic fibrillar assembly of human amylin. *Journal of structural biology* **119**, 17-27, 1997.

93 Härd, T. Amyloid Fibrils: Formation, Polymorphism, and Inhibition. *The Journal of Physical Chemistry Letters* **5**, 607-614, 2014.

94 Ke, P. C. *et al.* Half a century of amyloids: past, present and future. *Chemical Society reviews*, 2020.

95 Last, N. B., Rhoades, E. & Miranker, A. D. Islet amyloid polypeptide demonstrates a persistent capacity to disrupt membrane integrity. *Proceedings of the National Academy of Sciences* **108**, 9460-9465, 2011.

96 Birol, M., Kumar, S., Rhoades, E. & Miranker, A. D. Structurally distinct oligomers of islet amyloid polypeptide mediate toxic and non-toxic membrane poration. *bioRxiv*, 095158, 2017.

97 Bram, Y. *et al.* Apoptosis induced by islet amyloid polypeptide soluble oligomers is neutralized by diabetes-associated specific antibodies. *Scientific reports* **4**, 4267-4267, 2014.

98 Jaikaran, E. T. A. S. & Clark, A. Islet amyloid and type 2 diabetes: from molecular misfolding to islet pathophysiology. *Biochimica et Biophysica Acta (BBA) - Molecular Basis of Disease* **1537**, 179-203, 2001.

99 Dreaden, E. C., Alkilany, A. M., Huang, X., Murphy, C. J. & El-Sayed, M. A. The golden age: gold nanoparticles for biomedicine. *Chemical Society reviews* **41**, 2740-2779, 2012.

100 Dobson, J. Magnetic nanoparticles for drug delivery. *Drug Development Research* **67**, 55-60, 2006.

101 Brancolini, G. *et al.* Probing the Influence of Citrate-Capped Gold Nanoparticles on an Amyloidogenic Protein. *ACS Nano* **9**, 2600-2613, 2015.

102 Zhang, M. *et al.* Nanomaterials for Reducing Amyloid Cytotoxicity. *Advanced Materials* **25**, 3780-3801, 2013.

103 Owens, D. E. & Peppas, N. A. Opsonization, biodistribution, and pharmacokinetics of polymeric nanoparticles. *International Journal of Pharmaceutics* **307**, 93-102, 2006.

104 Linse, S. *et al.* Nucleation of protein fibrillation by nanoparticles. *Proceedings of the National Academy of Sciences of the United States of America* **104**, 8691-8696, 2007.

105 Lundqvist, M. *et al.* Nanoparticle size and surface properties determine the protein corona with possible implications for biological impacts. *Proceedings of the National Academy of Sciences* **105**, 14265, 2008.

106 Oh, J. Y. *et al.* Cloaking nanoparticles with protein corona shield for targeted drug delivery. *Nature Communications* **9**, 4548, 2018.

107 Ke, P. C., Lin, S., Parak, W. J., Davis, T. P. & Caruso, F. A Decade of the Protein Corona. *ACS nano* **11**, 11773-11776, 2017.

108 Nguyen, V. H. & Lee, B. J. Protein corona: a new approach for nanomedicine design. *International journal of nanomedicine* **12**, 3137-3151, 2017.

109 Cedervall, T. *et al.* Understanding the nanoparticle–protein corona using methods to quantify exchange rates and affinities of proteins for nanoparticles. *Proceedings of the National Academy of Sciences* **104**, 2050, 2007.

110 Docter, D. *et al.* The nanoparticle biomolecule corona: lessons learned – challenge accepted? *Chemical Society reviews* **44**, 6094-6121, 2015.

111 Rocker, C., Potzl, M., Zhang, F., Parak, W. J. & Nienhaus, G. U. A quantitative fluorescence study of protein monolayer formation on colloidal nanoparticles. *Nat Nanotechnol* **4**, 577-580, 2009.

112 Walczyk, D., Bombelli, F. B., Monopoli, M. P., Lynch, I. & Dawson, K. A. What the Cell "Sees" in Bionanoscience. *Journal of the American Chemical Society* **132**, 5761-5768, 2010.

113 Casals, E., Pfaller, T., Duschl, A., Oostingh, G. J. & Puntes, V. Time Evolution of the Nanoparticle Protein Corona. *ACS Nano* **4**, 3623-3632, 2010.

114 Vroman, L. Effect of absorbed proteins on the wettability of hydrophilic and hydrophobic solids. *Nature* **196**, 476-477, 1962.

115 Koegler, P., Clayton, A., Thissen, H., Santos, G. N. & Kingshott, P. The influence of nanostructured materials on biointerfacial interactions. *Advanced drug delivery reviews* **64**, 1820-1839, 2012.

116 Huhn, D. *et al.* Polymer-coated nanoparticles interacting with proteins and cells: focusing on the sign of the net charge. *ACS Nano* **7**, 3253-3263, 2013.

117 Dobrovolskaia, M. A. *et al.* Interaction of colloidal gold nanoparticles with human blood: effects on particle size and analysis of plasma protein binding profiles. *Nanomedicine : nanotechnology, biology, and medicine* **5**, 106-117, 2009.

118 Joseph, D., Sachar, S., Kishore, N. & Chandra, S. Mechanistic insights into the interactions of magnetic nanoparticles with bovine serum albumin in presence of surfactants. *Colloids and surfaces. B, Biointerfaces* **135**, 596-603, 2015.

119 Cox, A. *et al.* Evolution of Nanoparticle Protein Corona across the Blood–Brain Barrier. *ACS Nano* **12**, 7292-7300, 2018.

120 Pardridge, W. M. Drug transport across the blood-brain barrier. *Journal of cerebral blood flow and metabolism : official journal of the International Society of Cerebral Blood Flow and Metabolism* **32**, 1959-1972, 2012.

121 Ke, P. C. *et al.* Mitigation of Amyloidosis with Nanomaterials. *Advanced Materials*, 1901690, 2019.

122 Faridi, A. *et al.* Mitigating Human IAPP Amyloidogenesis In Vivo with Chiral Silica Nanoribbons. *Small* **14**, 1802825, 2018.

123 Lee, Y. K., Choi, E. J., Webster, T. J., Kim, S. H. & Khang, D. Effect of the protein corona on nanoparticles for modulating cytotoxicity and immunotoxicity. *International journal of nanomedicine* **10**, 97-113, 2015.

124 Wang, F. *et al.* The biomolecular corona is retained during nanoparticle uptake and protects the cells from the damage induced by cationic nanoparticles until degraded in the lysosomes. *Nanomedicine : nanotechnology, biology, and medicine* **9**, 1159-1168, 2013.

125 Clift, M. J. D., Bhattacharjee, S., Brown, D. M. & Stone, V. The effects of serum on the toxicity of manufactured nanoparticles. *Toxicol Lett* **198**, 358-365, 2010.

126 Tedja, R., Lim, M., Amal, R. & Marquis, C. Effects of serum adsorption on cellular uptake profile and consequent impact of titanium dioxide nanoparticles on human lung cell lines. *ACS Nano* **6**, 4083-4093, 2012.

127 Cheng, B. *et al.* Silibinin inhibits the toxic aggregation of human islet amyloid polypeptide. *Biochemical and biophysical research communications* **419**, 495-499, 2012.

128 Ehrnhoefer, D. E. *et al.* EGCG redirects amyloidogenic polypeptides into unstructured, off-pathway oligomers. *Nature structural & molecular biology* **15**, 558-566, 2008.

129 Daval, M. *et al.* The effect of curcumin on human islet amyloid polypeptide misfolding and toxicity. *Amyloid : the international journal of experimental and clinical investigation : the official journal of the International Society of Amyloidosis* **17**, 118-128, 2010.

130 Sparks, S., Liu, G., Robbins, K. J. & Lazo, N. D. Curcumin modulates the self-assembly of the islet amyloid polypeptide by disassembling α-helix. *Biochemical and biophysical research communications* **422**, 551-555, 2012.

131 Ladiwala, A. R. *et al.* Resveratrol selectively remodels soluble oligomers and fibrils of amyloid Abeta into off-pathway conformers. *The Journal of biological chemistry* **285**, 24228-24237, 2010.

132 Re, F. *et al.* Beta amyloid aggregation inhibitors: small molecules as candidate drugs for therapy of Alzheimer's disease. *Current medicinal chemistry* **17**, 2990-3006, 2010.

133 Stains, C. I., Mondal, K. & Ghosh, I. Molecules that Target beta-Amyloid. *ChemMedChem* **2**, 1674-1692, 2007.

134 Saraogi, I. *et al.* Synthetic alpha-helix mimetics as agonists and antagonists of islet amyloid polypeptide aggregation. *Angewandte Chemie (International ed. in English)* **49**, 736-739, 2010.

135 Kokkoni, N., Stott, K., Amijee, H., Mason, J. M. & Doig, A. J. N-Methylated peptide inhibitors of beta-amyloid aggregation and toxicity. Optimization of the inhibitor structure. *Biochemistry* **45**, 9906-9918, 2006.

136 Ribarič, S. Peptides as Potential Therapeutics for Alzheimer's Disease. *Molecules* **23**, 283, 2018.

137 John, T. *et al.* Impact of nanoparticles on amyloid peptide and protein aggregation: a review with a focus on gold nanoparticles. *Nanoscale* **10**, 20894-20913, 2018.

138 Gladytz, A., Abel, B. & Risselada, H. J. Gold-Induced Fibril Growth: The Mechanism of Surface-Facilitated Amyloid Aggregation. *Angewandte Chemie (International ed. in English)* **55**, 11242-11246, 2016.

139 Hane, F., Tran, G., Attwood, S. J. & Leonenko, Z. Cu(2+) affects amyloid-beta (1-42) aggregation by increasing peptide-peptide binding forces. *PloS one* **8**, e59005, 2013.

140 Lück, M., Paulke, B. R., Schröder, W., Blunk, T. & Müller, R. H. Analysis of plasma protein adsorption on polymeric nanoparticles with different surface characteristics. *Journal of Biomedical Materials Research* **39**, 478-485, 1998.

141 Ehrenberg, M. & McGrath, J. L. Binding between particles and proteins in extracts: implications for microrheology and toxicity. *Acta Biomaterialia* **1**, 305-315, 2005.

142 Gessner, A., Lieske, A., Paulke, B. R. & Müller, R. H. Influence of surface charge density on protein adsorption on polymeric nanoparticles: analysis by two-dimensional electrophoresis. *European Journal of Pharmaceutics and Biopharmaceutics* **54**, 165-170, 2002.

143 Cedervall, T. *et al.* Detailed identification of plasma proteins adsorbed on copolymer nanoparticles. *Angewandte Chemie (International ed. in English)* **46**, 5754-5756, 2007.

144 Mahmoudi, M. *et al.* Protein−Nanoparticle Interactions: Opportunities and Challenges. *Chemical Reviews* **111**, 5610-5637, 2011.

145 Gao, Q. *et al.* Amino acid adsorption on mesoporous materials: influence of types of amino acids, modification of mesoporous materials, and solution conditions. *The journal of physical chemistry. B* **112**, 2261-2267, 2008.

146 Meng, M., Stievano, L. & Lambert, J.-F. Adsorption and Thermal Condensation Mechanisms of Amino Acids on Oxide Supports. 1. Glycine on Silica. *Langmuir* **20**, 914-923, 2004.

147 Willett, R. L., Baldwin, K. W., West, K. W. & Pfeiffer, L. N. Differential adhesion of amino acids to inorganic surfaces. *Proceedings of the National Academy of Sciences* **102**, 7817, 2005.

148 Naik, R. R., Brott, L. L., Clarson, S. J. & Stone, M. O. Silica-precipitating peptides isolated from a combinatorial phage display peptide library. *Journal of nanoscience and nanotechnology* **2**, 95-100, 2002.

149 Eteshola, E., Brillson, L. J. & Lee, S. C. Selection and characteristics of peptides that bind thermally grown silicon dioxide films. *Biomolecular Engineering* **22**, 201-204, 2005.

150 Oren, E. E. *et al.* A novel knowledge-based approach to design inorganic-binding peptides. *Bioinformatics (Oxford, England)* **23**, 2816-2822, 2007.

151 Puddu, V. & Perry, C. C. Peptide Adsorption on Silica Nanoparticles: Evidence of Hydrophobic Interactions. *ACS Nano* **6**, 6356-6363, 2012.

152 Wang, M. *et al.* Graphene quantum dots against human IAPP aggregation and toxicity in vivo. *Nanoscale* **10**, 19995-20006, 2018.

153 Kim, D. *et al.* Graphene quantum dots prevent α-synucleinopathy in Parkinson's disease. *Nature Nanotechnology* **13**, 812-818, 2018.

154 Pilkington, E. H. *et al.* Star Polymers Reduce Islet Amyloid Polypeptide Toxicity via Accelerated Amyloid Aggregation. *Biomacromolecules* **18**, 4249-4260, 2017.

155 Li, M. *et al.* Chiral Metallohelical Complexes Enantioselectively Target Amyloid β for Treating Alzheimer's Disease. *Journal of the American Chemical Society* **136**, 11655-11663, 2014.

156 Sharma, J. *et al.* Control of self-assembly of DNA tubules through integration of gold nanoparticles. *Science (New York, N.Y.)* **323**, 112-116, 2009.

157 Bedrood, S. *et al.* Fibril structure of human islet amyloid polypeptide. *The Journal of biological chemistry* **287**, 5235-5241, 2012.

158 Rzepa, H. S. The past, present and future of Scientific discourse. *Journal of Cheminformatics* **3**, 46-46, 2011.

159 Ariga, K., Richards, G. J., Ishihara, S., Izawa, H. & Hill, J. P. Intelligent Chiral Sensing Based on Supramolecular and Interfacial Concepts. *Sensors (Basel, Switzerland)* **10**, 6796-6820, 2010.

160 Li, Z. *et al.* Reversible Plasmonic Circular Dichroism of Au Nanorod and DNA Assemblies. *Journal of the American Chemical Society* **134**, 3322-3325, 2012.

161 Chen, X. & Mao, S. S. Titanium Dioxide Nanomaterials: Synthesis, Properties, Modifications, and Applications. *Chemical Reviews* **107**, 2891-2959, 2007.

162 Wang, Z. L. Nanopiezotronics. *Advanced Materials* **19**, 889-892, 2007.

163 Knowles, T. P., Vendruscolo, M. & Dobson, C. M. The amyloid state and its association with protein misfolding diseases. *Nature reviews. Molecular cell biology* **15**, 384-396, 2014.

164 Cabaleiro-Lago, C., Quinlan-Pluck, F., Lynch, I., Dawson, K. A. & Linse, S. Dual Effect of Amino Modified Polystyrene Nanoparticles on Amyloid β Protein Fibrillation. *ACS Chemical Neuroscience* **1**, 279-287, 2010.

165 Volpatti, L. R., Vendruscolo, M., Dobson, C. M. & Knowles, T. P. J. A Clear View of Polymorphism, Twist, and Chirality in Amyloid Fibril Formation. *ACS Nano* **7**, 10443-10448, 2013.

166 Xue, C., Lin, T. Y., Chang, D. & Guo, Z. Thioflavin T as an amyloid dye: fibril quantification, optimal concentration and effect on aggregation. *Royal Society open science* **4**, 160696, 2017.

167 Usov, I. & Mezzenga, R. FiberApp: An Open-Source Software for Tracking and Analyzing Polymers, Filaments, Biomacromolecules, and Fibrous Objects. *Macromolecules* **48**, 1269-1280, 2015.

168 Hampton, M. B. & Orrenius, S. Dual regulation of caspase activity by hydrogen peroxide: implications for apoptosis. *FEBS letters* **414**, 552-556, 1997.

169 Blalock, E. M. *et al.* Harnessing the power of gene microarrays for the study of brain aging and Alzheimer's disease: statistical reliability and functional correlation. *Ageing research reviews* **4**, 481-512, 2005.

170 Liu, T., Belov, M. E., Jaitly, N., Qian, W.-J. & Smith, R. D. Accurate mass measurements in proteomics. *Chemical reviews* **107**, 3621-3653, 2007.

171 Kennedy, S. The role of proteomics in toxicology: identification of biomarkers of toxicity by protein expression analysis. *Biomarkers* **7**, 269-290, 2002.

172 Mirzaei, M. *et al.* Age-related neurodegenerative disease associated pathways identified in retinal and vitreous proteome from human glaucoma eyes. *Scientific reports* **7**, 12685, 2017.

173 Dogan, A. Amyloidosis: Insights from Proteomics. *Annual review of pathology* **12**, 277-304, 2017.

174 Walker, D. G., Link, J., Lue, L. F., Dalsing-Hernandez, J. E. & Boyes, B. E. Gene expression changes by amyloid beta peptide-stimulated human postmortem brain microglia identify activation of multiple inflammatory processes. *Journal of leukocyte biology* **79**, 596-610, 2006.

175 Wang, S., Qaisar, U., Yin, X. & Grammas, P. Gene expression profiling in Alzheimer's disease brain microvessels. *Journal of Alzheimer's disease : JAD* **31**, 193-205, 2012.

176 Muller, T. *et al.* Modulation of gene expression and cytoskeletal dynamics by the amyloid precursor protein intracellular domain (AICD). *Molecular biology of the cell* **18**, 201-210, 2007.

177 de Godoy, L. M. F. *et al.* Comprehensive mass-spectrometry-based proteome quantification of haploid versus diploid yeast. *Nature* **455**, 1251-1254, 2008.

178 Schmidt, A., Claassen, M. & Aebersold, R. Directed mass spectrometry: towards hypothesis-driven proteomics. *Current Opinion in Chemical Biology* **13**, 510-517, 2009.

179 Brunner, E. *et al.* A high-quality catalog of the Drosophila melanogaster proteome. *Nature biotechnology* **25**, 576-583, 2007.

180 Unger, M. S., Schernthaner, P., Marschallinger, J., Mrowetz, H. & Aigner, L. Microglia prevent peripheral immune cell invasion and promote an anti-inflammatory environment in the brain of APP-PS1 transgenic mice. *Journal of neuroinflammation* **15**, 274, 2018.

181 Sheng, J. G. *et al.* Interleukin-1 promotion of MAPK-p38 overexpression in experimental animals and in Alzheimer's disease: potential significance for tau protein phosphorylation. *Neurochem Int* **39**, 341-348, 2001.

182 Hayes, A., Thaker, U., Iwatsubo, T., Pickering-Brown, S. M. & Mann, D. M. Pathological relationships between microglial cell activity and tau and amyloid beta protein in patients with Alzheimer's disease. *Neuroscience letters* **331**, 171-174, 2002.

183 Benzing, W. C. *et al.* Evidence for glial-mediated inflammation in aged APP(SW) transgenic mice. *Neurobiology of aging* **20**, 581-589, 1999.

184 Dionisio-Santos, D. A., Olschowka, J. A. & O'Banion, M. K. Exploiting microglial and peripheral immune cell crosstalk to treat Alzheimer's disease. *Journal of neuroinflammation* **16**, 74, 2019.

185 Schupf, N. *et al.* Elevated Plasma β-Amyloid Peptide Aβ42 Levels, Incident Dementia, and Mortality in Down Syndrome. *Archives of Neurology* **64**, 1007-1013, 2007.

186 Scheuner, D. *et al.* Secreted amyloid β–protein similar to that in the senile plaques of Alzheimer's disease is increased in vivo by the presenilin 1 and 2 and APP mutations linked to familial Alzheimer's disease. *Nature Medicine* **2**, 864-870, 1996.

187 Glass, J. J. *et al.* Charge Has a Marked Influence on Hyperbranched Polymer Nanoparticle Association in Whole Human Blood. *ACS Macro Letters* **6**, 586-592, 2017.

188 Biere, A. L. *et al.* Amyloid beta-peptide is transported on lipoproteins and albumin in human plasma. *The Journal of biological chemistry* **271**, 32916-32922, 1996.

189 Matsubara, E. *et al.* Soluble Abeta homeostasis in AD and DS: impairment of anti-amyloidogenic protection by lipoproteins. *Neurobiology of aging* **25**, 833-841, 2004.

190 Parvathy, S. *et al.* Abeta peptide conformation determines uptake and interleukin-1alpha expression by primary microglial cells. *Neurobiology of aging* **30**, 1792-1804, 2009.

191 Chen, P. *et al.* Multiplex Serum Cytokine Immunoassay Using Nanoplasmonic Biosensor Microarrays. *ACS Nano* **9**, 4173-4181, 2015.

192 Javed, I. *et al.* Probing the Aggregation and Immune Response of Human Islet Amyloid Polypeptides with Ligand-Stabilized Gold Nanoparticles. *ACS applied materials & interfaces* **11**, 10462-10471, 2019.

193 Howe, K. *et al.* The zebrafish reference genome sequence and its relationship to the human genome. *Nature* **496**, 498-503, 2013.

194 Lin, S., Zhao, Y., Nel, A. E. & Lin, S. Zebrafish: an in vivo model for nano EHS studies. *Small (Weinheim an der Bergstrasse, Germany)* **9**, 1608-1618, 2013.

195 Kalueff, A. V., Stewart, A. M. & Gerlai, R. Zebrafish as an emerging model for studying complex brain disorders. *Trends in pharmacological sciences* **35**, 63-75, 2014.

196 Best, J. D. & Alderton, W. K. Zebrafish: An in vivo model for the study of neurological diseases. *Neuropsychiatric disease and treatment* **4**, 567-576, 2008.

197 Newman, M., Ebrahimie, E. & Lardelli, M. Using the zebrafish model for Alzheimer's disease research. *Frontiers in Genetics* **5**, 2014.

198 Zang, L., Shimada, Y. & Nishimura, N. Development of a Novel Zebrafish Model for Type 2 Diabetes Mellitus. *Scientific reports* **7**, 1461, 2017.

199 Lieschke, G. J. & Currie, P. D. Animal models of human disease: zebrafish swim into view. *Nature Reviews Genetics* **8**, 353-367, 2007.

200 Dalgin, G. & Prince, V. E. Differential levels of Neurod establish zebrafish endocrine pancreas cell fates. *Developmental biology* **402**, 81-97, 2015.

201 Javed, I. *et al.* Inhibition of amyloid beta toxicity in zebrafish with a chaperone-gold nanoparticle dual strategy. *Nature communications* **10**, 3780, 2019.

202 Rink, E. & Wullimann, M. F. Connections of the ventral telencephalon and tyrosine hydroxylase distribution in the zebrafish brain (Danio rerio) lead to identification of an ascending dopaminergic system in a teleost. *Brain research bulletin* **57**, 385-387, 2002.

203 Flinn, L. *et al.* Complex I deficiency and dopaminergic neuronal cell loss in parkin-deficient zebrafish (Danio rerio). *Brain : a journal of neurology* **132**, 1613-1623, 2009.

204 Xi, Y., Noble, S. & Ekker, M. Modeling neurodegeneration in zebrafish. *Curr Neurol Neurosci Rep* **11**, 274-282, 2011.

205 Musa, A., Lehrach, H. & Russo, V. A. Distinct expression patterns of two zebrafish homologues of the human APP gene during embryonic development. *Development genes and evolution* **211**, 563-567, 2001.

206 Jiang, H., Newman, M. & Lardelli, M. The zebrafish orthologue of familial Alzheimer's disease gene PRESENILIN 2 is required for normal adult melanotic skin pigmentation. *PloS one* **13**, e0206155, 2018.

207 Geling, A., Steiner, H., Willem, M., Bally-Cuif, L. & Haass, C. A γ-secretase inhibitor blocks Notch signaling in vivo and causes a severe neurogenic phenotype in zebrafish. *EMBO reports* **3**, 688-694, 2002.

208 Joshi, P., Liang, J. O., DiMonte, K., Sullivan, J. & Pimplikar, S. W. Amyloid precursor protein is required for convergent-extension movements during Zebrafish development. *Developmental biology* **335**, 1-11, 2009.

209 Tomasiewicz, H. G., Flaherty, D. B., Soria, J. P. & Wood, J. G. Transgenic zebrafish model of neurodegeneration. *Journal of neuroscience research* **70**, 734-745, 2002.

210 Faridi, A. *et al.* Differential Roles of Plasma Protein Corona on Immune Cell Association and Cytokine Secretion of Oligomeric and Fibrillar Beta-Amyloid. *Biomacromolecules* **20**, 4208-4217, 2019.

Chapter 2

Differential roles of plasma protein corona on immune cell association and cytokine secretion of oligomeric and fibrillar beta amyloid

1. Declaration and rationale

“This chapter was published as Faridi, A., Yang, W., Kelly, H.G., Wang, C., Faridi, P., Purcell, A.W., Davis, T.P., Chen, P., Kent, S.J., Ke, P.C., Differential Roles of Plasma Protein Corona on Immune Cell Association and Cytokine Secretion of Oligomeric and Fibrillar Beta-Amyloid, (2019) **Biomacromolecules**. Reprinted with permission from reference[210] Copyright 2019 American Chemical Society."

In this study, the effect of plasma protein corona on the association of Aβ aggregates with immune cells and their cytokine secretion was reported. This study demonstrated a close connection between amyloidogenesis and the immune response of amyloid proteins, an important but overlooked aspect central to understanding the pathology of AD.

Article

Cite This: Biomacromolecules 2019, 20, 4208−4217

pubs.acs.org/Biomac

Differential Roles of Plasma Protein Corona on Immune Cell Association and Cytokine Secretion of Oligomeric and Fibrillar Beta-Amyloid

Ava Faridi,[†] Wen Yang,[‡] Hannah Gabrielle Kelly,[§,∥] Chuanyu Wang,[‡] Pouya Faridi,[⊥] Anthony Wayne Purcell,[⊥] Thomas P. Davis,[*,†,#] Pengyu Chen,[*,‡] Stephen J. Kent,[*,§,∥,▽] and Pu Chun Ke[*,†]

[†]ARC Centre of Excellence in Convergent Bio-Nano Science and Technology, Monash Institute of Pharmaceutical Sciences, Monash University, 381 Royal Parade, Parkville, Victoria 3052, Australia

[‡]Materials Research and Education Center, Auburn University, Auburn, Alabama 36849, United States

[§]Department of Microbiology and Immunology, Peter Doherty Institute for Infection and Immunity, University of Melbourne, Melbourne, Victoria 3052, Australia

[∥]ARC Centre for Excellence in Convergent Bio-Nano Science and Technology, University of Melbourne, Melbourne, Victoria 3052, Australia

[⊥]Infection and Immunity Program & Department of Biochemistry and Molecular Biology, Biomedicine Discovery Institute, Monash University, Clayton, Victoria 3800, Australia

[#]Australian Institute for Bioengineering and Nanotechnology, The University of Queensland, Brisbane, Queensland 4072, Australia

[▽]Melbourne Sexual Health Clinic and Infectious Diseases Department, Alfred Hospital, Monash University Central Clinical School, Carlton, Victoria 3053, Australia

Supporting Information

ABSTRACT: Alzheimer's disease (AD) is a primary neurological disease with no effective cure. A hallmark of AD is the presence of intracellular tangles and extracellular plaques derived from the aberrant aggregation of tau- and beta-amyloid ($A\beta$). $A\beta$ presents in the brain as well as in cerebrospinal fluid and the circulation, and $A\beta$ toxicity has been attributed to amyloidosis and inflammation, among other causes. In this study, the effects of the plasma protein corona have been investigated with regard to the blood cell association and cytokine secretion of oligomeric ($A\beta o$) and fibrillar $A\beta_{1-42}$($A\beta_f$), two major forms of the peptide aggregates. $A\beta o$ displayed little change in membrane association in whole blood or washed blood (i.e., cells in the absence of plasma proteins) at 37 °C, while $A\beta_f$ showed a clear preference for binding with all cell types sans plasma proteins. Immune cells exposed to $A\beta o$, but not to $A\beta_f$, resulted in significant expression of cytokines IL-6 and TNF measured in real-time by a localized surface plasmon resonance sensor. These observations indicate greater immune cell association and cytokine stimulation of $A\beta o$ than $A\beta_f$ and shed new light on the contrasting toxicities of $A\beta o$ and $A\beta_f$ resulting from their differential capacities in acquiring a plasma protein corona. These results further implicate a close connection between $A\beta$ amyloidosis and immunopathology in AD.

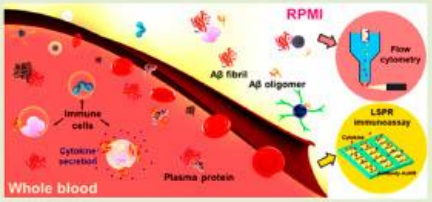

INTRODUCTION

Beta amyloid ($A\beta$) originates from amyloid precursor protein (APP), an integral membrane protein expressed in tissues and especially in the brain. The APP is cleaved off by β and γ secretases, yielding two major peptide products $A\beta_{1-40}$ and $A\beta_{1-42}$.[1] Among the two peptides, $A\beta_{1-42}$ is more hydrophobic due to the two additional amino acids of isoleucine and alanine at the C-terminus and is considerably more cytotoxic due to its higher tendency in aberrant aggregation. The extracellular amyloid deposits of $A\beta$ and the intracellular tangles of tau are two histopathological hallmarks of Alzheimer's disease (AD), a primary form of neurological disorder in aging populations.[2]

While $A\beta$ plaques are often located in the brain tissues of AD patients postmortem, the peptide itself can also be traced in cerebrospinal fluid (CSF) and the circulation.[3] The relationship between the peptide levels in the brain, CSF, and plasma in healthy and diseased individuals, however,

Received: August 13, 2019
Revised: October 2, 2019
Published: October 10, 2019

DOI: 10.1021/acs.biomac.9b01116
Biomacromolecules 2019, 20, 4208−4217

remains unclear.[4] Compelling evidence has shown the transport of Aβ by serum albumin and apolipoproteins in the blood plasma,[5,6] likely due to the poor solubility of the peptide as well as the chaperone-like capacity of serum albumin[7−9] against the conformational changes of Aβ. Furthermore, while specific receptors on microglia and monocytes/macrophages in the brain may determine the clearance of extracellular Aβ peptides through noninflammatory phagocytosis or pro-inflammatory cytokine secretion,[10−14] adherence of complement C3b to complement receptor 1 (CR1) of erythrocytes is a mechanism hypothesized for the peripheral clearance of Aβ.[15]

The literature has suggested the use of Aβ in the blood as an effective indicator for the early diagnosis of AD.[16] The effect of human serum albumin (HSA) on the reduction of α-synuclein aggregation (associated with Parkinson's disease) has been reported recently.[17] However, the associations of plasma proteins and blood cells with Aβ in its major aggregation forms, namely, oligomers and amyloid fibrils (abbreviated as $A\beta_O$ and $A\beta_f$ hereafter, to refer to the chiefly oligomeric and fibrillar forms of the peptide), remain unclear. Furthermore, the immune responses of blood cells to amyloidogenic peptides and their aggregates have not been systematically investigated. To understand the transformation of Aβ in circulation, here we examined the binding of human blood cells with $A\beta_O$ and $A\beta_f$ with a special attention to plasma proteins, using a high-throughput blood association assay.[18,19] We further characterized real-time secretion of cytokines, i.e., interleukin 6 (IL-6) and tumor necrosis factor alpha (TNF), by human monocytes and lymphocytes exposed to $A\beta_O$ and $A\beta_f$ using a localized surface plasmon resonance (LSPR) immunoassay.[20] Both our blood cell and LSPR immune assays implicated a significant role of plasma protein corona in shaping the cell binding affinity and toxicity of amyloid-protein aggregates and demonstrated a convoluted relationship between amyloidosis and inflammation in AD.

■ MATERIALS AND METHODS

Aβ preparation. Hexafluoro-2-propanol (HFIP)-treated human $A\beta_{1-42}$ (AnaSpec, sequence, AIAEGDSHVLKEGAYMEIFDVQGHVFGGKIFRVVDLGSHNVA; purity, HPLC ≥ 95%; abbreviated as Aβ hereafter) was used in preparation of the two aggregating states of Aβ. Specifically, $A\beta_O$ was rendered by incubating the freshly dissolved Aβ in 0.003% NH_4OH buffer at room temperature for 30 h, while $A\beta_f$ was obtained by incubating the peptide at 37 °C for more than 60 h. The two aggregation states were confirmed by a ThT kinetic assay and TEM imaging.

Transmission Electron Microscopy (TEM). For TEM imaging, 5 μL of $A\beta_O$ and $A\beta_f$ (each of 50 μM), plasma proteins, Aβo, and $A\beta_f$ in interaction with plasma proteins were pipetted onto copper grids (400 mesh, glow-discharged for 15 s; Formvar film, ProSciTech) and let to adsorb for 1 min. After removing unbound samples by filter paper the grids were rinsed with 10 μL of Milli-Q water. The grids were then negatively stained with 5 μL of 1% uranyl acetate (UA) for 30 s and blown dry. The samples were imaged by a transmission electron microscope (Tecnai G2 F20, FEI, Eindhoven, The Netherlands) under an electric potential of 200 kV. Images were acquired with a CCD camera (UltraScan 1000, Gatan).

Thioflavin T (ThT) Kinetic Assay. A kinetic assay on peptide fibrillization was conducted using 50 μM Aβ and 100 μM ThT dye pipetted into a 96-well plate (Costar). Changes in ThT fluorescence, indicating the β-sheet content in the sample, were recorded at 37 °C until the saturation phase after 60 h by a plate reader (PerkinElmer EnSight HH33400; Ex/Em, 440/485 nm). The assay was done with triplicate for each sample condition.

Cell Culture and Toxicity Assay. SH-SY5Y neuroblastoma cells were cultured in Dulbecco's modified Eagle's medium: Nutrient Mixture F-12 (DMED/F12, ATCC) with 10% fetal bovine serum (FBS). For the viability assay, a 96-well plate (Costar) was pretreated with poly-L-lysine (Sigma, 0.01%), incubated at 37 °C (5% CO_2) for 30 min, and washed with phosphate buffered saline (PBS) thrice. Approximately 60 000 cells were added to each well and incubated at 37 °C and 5% CO_2 to reach 80% confluency. Propidium iodide (PI, 1 μM) dye in fresh DMEM/F12 was added and incubated with the cells for 30 min. After optimization of concentrations, samples of 20 μM Aβ in the form of oligomers or fibrils were added to the wells. After 15 h of treatment, the cell viability was read by an Operetta instrument (PerkinElmer, 20× lens; numerical aperture, 0.7) at 37 °C with 5% CO_2. The PI-positive apoptotic cells were counted by the mapping function of the instrument. Nine reads per well for samples of triplicate were acquired. Untreated cells were imaged as the control.

Helium Ion Microscopy (HIM). Whole and washed blood cells were treated with 10 μM $A\beta_O$ and $A\beta_f$ with and without plasma proteins. The samples were then treated by 2.5% paraformaldehyde and incubated at 4 °C for 10 h. After the incubation, the samples were centrifuged, and paraformaldehyde/medium was replaced every 2 h with gradient concentrations of ethanol (20%, 40%, 60%, 80%, and 95%). A 30 μL portion of each sample was transferred to a carbon tape and air-dried. The cell morphologies were visualized by Orion NanoFab (Zeiss).

Association of Aβ Species with Human Immune Cells. Fresh blood was drawn from a healthy donor into sodium heparin Vacuettes (Greiner Bio-One) in accordance with the University of Melbourne Human ethics approval 1443420 and the Australian National Health and Medical Research Council Statement on Ethical Conduct in Human Research. The blood cells were counted using a CELL-DYN Emerald analyzer (Abbott). To prepare washed blood cells, 10 mL of whole blood was topped up to 50 mL with PBS and spun down at 950g, for 10 min, with slow brake. The process was repeated four more times to collect washed blood cells. The removal of plasma proteins from the cells was indicated using a UV−vis spectrophotometer (Nanodrop 2000, Thermo Fisher), where the protein absorbance at 280 nm was absent to confirm their removal. The cells were resuspended in serum-free RPMI 1640 (Gibco) to keep the cell concentration of whole and washed blood consistent. ThT-labeled $A\beta_O$ or $A\beta_f$ was added to 100 μL of blood in triplicate at 5, 10, and 15 μM and incubated at 4 and 37 °C for 1 h. Pharm Lyse buffer (BD) was added to lyse red blood cells at 40× blood volume, followed by washing twice with 4 mL of PBS (500g, 7 min). The cells were phenotyped for 1 h on ice by titrating antibodies against CD3 AF700 (SP34-2, BD), CD14 APC-H7 (MΦP9, BD), CD56 PE (B159, BD), lineage-1 cocktail FITC (BD), HLA-DR PerCP-Cy5.5 (G46−6, BD), and CD19 BV650 (HIB19, Biolegend). Free antibodies were washed and removed by centrifugation (500g, 7 min) with a PBS buffer containing 0.5% w/v BSA and 2 mM EDTA at 4 °C. The cells were fixed by formaldehyde in PBS at 1% weight to volume ratio. The samples were analyzed for cell association using flow cytometry (LSRFortessa, BD Biosciences) and software FlowJo V10.

LSPR Detection of Immune Cell Responses to Aβ Species. *Cell Culture.* Jurkat human T cells (ATCCCRL-2901) were cultured in RPMI-1640 medium (ATCC) with 200 μg/mL G428 and 10% FBS (ATCC). The cells were incubated at 37 °C with 5% CO_2 (Thermo Scientific). Epstein−Barr virus transformed human B lymphoblasts (ATCC) were cultured in RPMI-1640 medium with 10% FBS. Human monocytic THP-1 cells (ATCC) were cultured in RPMI-1640 medium with 50 μM mercaptoethanol and 10% FBS. The cell culture was maintained by replenishing the medium every 2−3 days at 1×10^5 to 1×10^6 cells/mL. The cells were collected by centrifugation (125g, 5 min) and resuspended in fresh culture medium.

LSPR Immunoassay. The human immune cell lines (T cells, B cells, or THP-1 cells) were resuspended in human plasma proteins (Innovative Research) and RPMI-1640 medium at 1×10^6 cells/mL, respectively. The immune cells were incubated with Aβo and $A\beta_f$ of 5, 10, and 15 μM final concentrations for 2 h at 4 and 37 °C. The

DOI: 10.1021/acs.biomac.9b01116
Biomacromolecules 2019, 20, 4208−4217

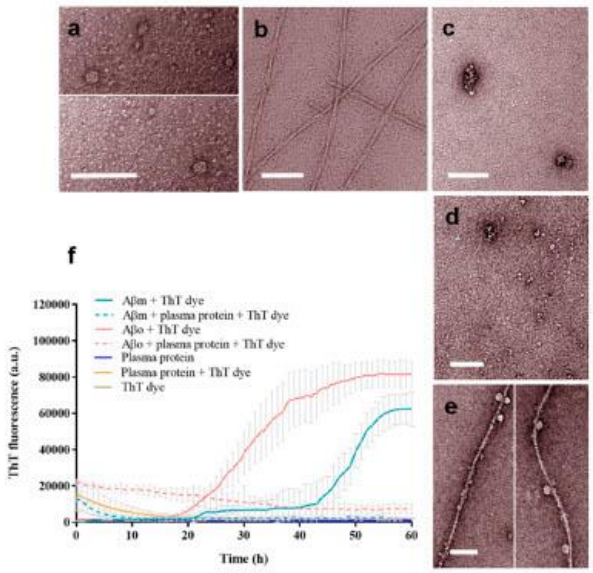

Figure 1. TEM imaging and ThT kinetic assay of Aβ fibrillization. TEM images show the following structures: (a) Aβo, (b) Aβf, (c) plasma proteins, (d) Aβo with plasma proteins, and (e) Aβf with plasma proteins. The experiments were performed in triplicate. The error bars indicate the standard deviations of averaged data sets. Aβ concentration: 50 μM (ThT assay, 37 °C) and 20 μM (TEM, at room temperature). Scale bars: 100 nm. (f) ThT kinetic assay of Aβm and Aβo fibrillization with and without plasma proteins.

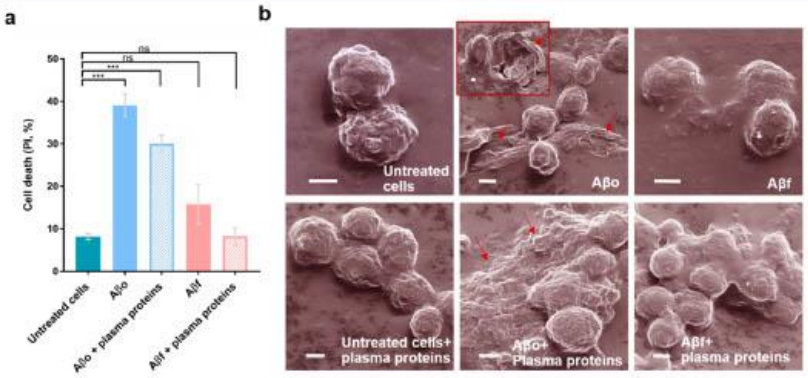

Figure 2. Viability and morphology of neuronal cells exposed to the Aβ species with or without plasma proteins. (a) SY5Y cell toxicities exposed to Aβo and Aβf. PI: propidium iodide. (b) Helium ion microscopy indicates the toxicity of Aβ species with and without plasma proteins. Arrows indicate the deformation of cell membranes induced by Aβo. Cells were treated with the Aβ species for 2 h, with or without plasma proteins. The experiment was performed in triplicate, and error bars indicate standard deviations (ns, $P > 0.05$; and ***, $P \leq 0.001$). Aβ concentration: 20 μM. Scale bars: 2 μm.

immune responses of human THP-1 cells, human Jurkat T cells, and human B cells were investigated after stimulations with $A\beta_O$ and $A\beta_f$. After 2 h of incubation, the culture medium was extracted and pipetted into an LSPR immunoassay chip (for fabrication and measurement details, see the description in the Supporting Information, as well as Figure S1) for the detection of secretory cytokines from the immune cells. A total of more than 100 chips were used for this assay.

RESULTS AND DISCUSSION

Interactions of Aβ Aggregates with Plasma Proteins. Due to the kinetic nature of amyloidosis, which is a convolution of both primary and secondary nucleation

DOI: 10.1021/acs.biomac.9b01116
Biomacromolecules 2019, 20, 4208−4217

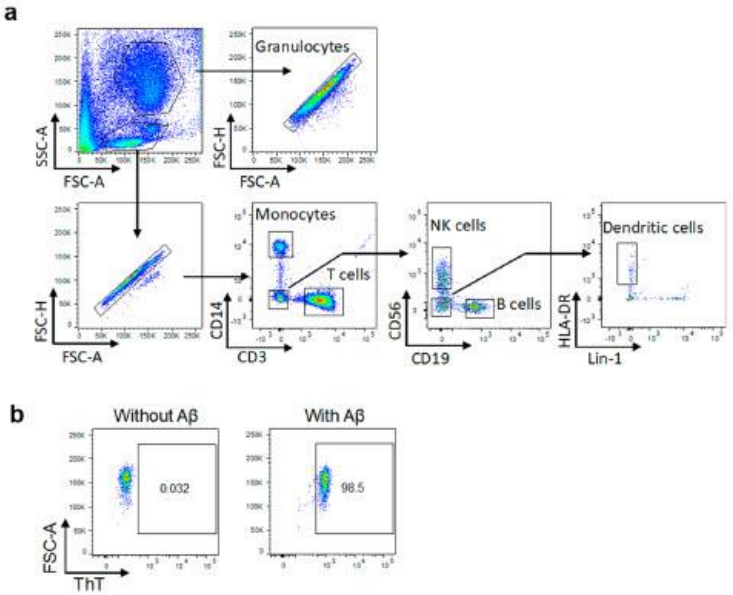

Figure 3. Gating strategy used to determine white blood cell populations and amyloid association. (a) Representative gating strategy used to determine white blood cell populations. Forward scatter area (FSC-A) and side scatter area (SSC-A) were first analyzed to locate white blood cells. Doublets were excluded based on the FSC-A vs FSC-H of single cells gated. The following cell types were identified using sequential gating based on expression of surface markers or light scatter: high SSC-A granulocytes; CD3+ T cells; CD14+ monocytes; CD56+ NK cells; CD19+ B cells; and Lin1-veHLA-DR+ dendritic cells. (b) Cell association with ThT-labeled Aβ was then measured, and an example of the gating is shown for the monocyte population. Further examples can be found in the Supporting Information, Figure S3.

followed by elongation and saturation,[1] the $A\beta_O$ and $A\beta_f$ samples were not pure oligomers or fibrils but were inclusive of a collection of minor heterogeneous aggregates. Indeed, the reverse phase HPLC (RP-HPLC; for the method, see the Supporting Information) revealed formation of slightly hydrophobic Aβo from its hydrophilic monomeric origin (centered on the retention time of ~20 min). As for the $A\beta_f$ sample, the monomeric and oligomeric species were depleted and converted into fibrillar structures of varying hydrophobicity (Figure S2).

The interaction of Aβ with blood components is of intense interest as it offers a model to understand the immune response to amyloid proteins. Previously, Kuo et al. reported the interactions of fresh $A\beta_{1-40}$ and $A\beta_{1-42}$ with plasma proteins.[21] Here, our TEM imaging of plasma proteins, and Aβo and $A\beta_f$ with and without plasma proteins confirmed the two aggregation states as globules and fibrils (Figure 1a,b), respectively. TEM imaging showed the morphologies of plasma proteins (Figure 1c) and their associations with the Aβ species (Figure 1d,e). Specifically, in the case of $A\beta_f$, a protein "corona" was rendered upon the peptide incubation with plasma proteins, mediated by H-bonding and electrostatic interactions between the $A\beta_f$ surface moieties and the amphiphilic plasma proteins.[22]

Aβ Aggregation Kinetics and Cytotoxicity. The ThT kinetics of $A\beta_m$ and $A\beta_O$ displayed a nucleation phase, followed by an elongation phase to a saturation phase of the peptide after ~60 h (Figure 1f). This result is consistent with the Aβ fibrillization in the literature.[23−25] In the presence of plasma proteins, interactions of both $A\beta_m$ and $A\beta_O$ with the proteins blocked the addition of Aβ monomers to inhibit the further assembly of the oligomers into amyloid fibrils.

Aggregation of amyloid proteins is a hallmark of neurodegenerative diseases and type 2 diabetes. Aβ aggregation is associated with neuronal cell degeneration,[26−28] and the Aβ oligomers are considered to be the most toxic species.[29,30] The cytotoxicity of Aβ in this study was consistent with the literature and with the aggregation inhibition of Aβ in interaction with plasma proteins (Figure 2a), revealing suppressed toxicity of $A\beta_O$ with plasma proteins (39 ± 2.6% without plasma proteins down to 30 ± 2% with plasma proteins). In comparison, $A\beta_f$ induced a modest 13% cytotoxicity which was not affected by plasma proteins.

Aβ Aggregation-Induced Membrane Damage. The morphologies of SH-SY5Y neuronal cells exposed to the two Aβ aggregating species were examined with helium ion microscopy (HIM). HIM utilizes a helium ion source to excite a small sample volume with a large depth and is advantageous to conventional scanning electron microscopy in both resolution and image brightness. Consistent with the viability assay, significant damage including membrane deformation and blebbing of the SH-SY5Y cells was observed upon their exposure to $A\beta_O$ (Figure 2b), while such damage was reduced in the presence of Aβo incubated with plasma proteins. In comparison, no damage was evident when the cells were exposed to $A\beta_f$ with or without plasma proteins.

DOI: 10.1021/acs.biomac.9b01116
Biomacromolecules 2019, 20, 4208−4217

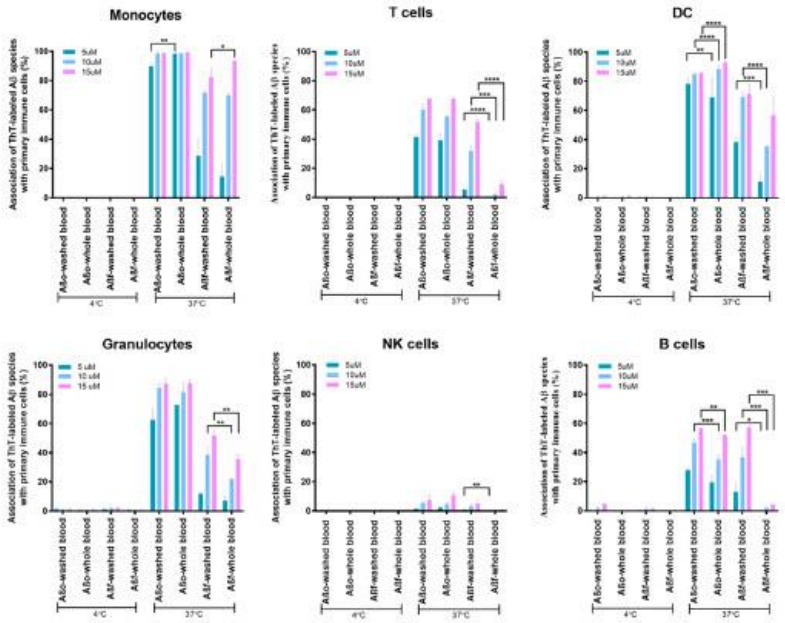

Figure 4. Association of the Aβ species with immune cells. The graphs show the association of immune cells as monocytes, T cells, dendritic cells, granulocytes, NK cells, and B cells with ThT-labeled $A\beta_O$ and $A\beta_f$ in 3 different concentration of 5, 10, and 15 μM. The treatments with $A\beta_O$ and $A\beta_f$ were applied at 4 and 37 °C in whole blood (with plasma proteins) and washed blood (plasma proteins removed). Association of Aβ with cell membranes was significantly lower in whole blood than washed blood. The assay was performed in triplicate. The error bars show standard deviations (*, $P < 0.05$; **, $P < 0.01$; ***, $P < 0.001$; and ****, $P < 0.0001$).

Cell Associations with Aβ Aggregates. In recent research, AD is considered as more than a neural-centric disease but has its origin in the immune system and inflammation.[31,32] To better understand the interaction between Aβ and blood immune cells, the association of fresh human blood phagocytes (granulocytes, monocytes, and dendritic cells) and lymphocytes (T cells, B cells, and natural killer/NK cells) with $A\beta_O$ and $A\beta_f$ in the presence and absence of plasma proteins was assessed by flow cytometry (Figures 3 and 4). The Aβ structures displayed no apparent association with any type of the immune cells at 4 °C in either whole blood or washed blood. An increment of temperature from 4 to 37 °C, which elevated biomolecular diffusion as well as the biological processes of endocytosis and phagocytosis uptake,[19] gave rise to increased association of Aβ with all types of the immune cells. Although the most prominent association of the Aβ proteins was with blood immune cells of phagocytic nature (granulocytes, monocytes, and dendritic cells), substantial association was also observed for B and T lymphocytes (Figure 4).

The amphiphilic structures of oligomers and protofibrils, known as the most toxic species of Aβ,[1] are less prone to interact with the hydrophilic surfaces of plasma proteins and biomolecules. On the other hand, amyloid peptides and proteins show a high propensity for cell membranes by initiating contact via the N termini of their functional monomers, which triggers their structural transition from monomers to alpha helices, toxic oligomers, and protofibrils, and, eventually, β-sheet rich amyloid fibrils.[1] Consistent with these known biochemical properties, we found that $A\beta_O$ displayed strong and comparable associations with the neuronal cells in both whole blood and washed blood cells (i.e., with plasma proteins removed, Figure 4). In contrast, $A\beta_f$ showed less association with the immune cells compared to $A\beta_O$. We hypothesized that this is likely due to the high capacity of $A\beta_f$ to establish hydrogen bonds with free plasma proteins, forming a nonspecific protein corona around the $A\beta_f$ when incubated with whole blood.[33] Indeed, we observed that $A\beta_f$ association with immune cells in whole blood (with plasma proteins) was generally greater than that observed in washed blood (without plasma proteins). This was particularly evident in the lymphocyte population (T, B, NK cells) where association was almost completely abrogated, with a less marked effect on granulocytes and dendritic cells.

The association of Aβ aggregates with plasma proteins entails both physical and toxicological implications. Serum albumin, the most abundant protein in the plasma, has been shown to inhibit $A\beta_{1-40}$ aggregation.[34,35] The higher level of toxic Aβ association with cell membranes can result in an elevated response from monocytes among immune cells.[34] Previous studies showed that the accumulations of Aβ, microglia, as well as blood monocyte macrophages were significantly involved in anti-inflammatory response to excess Aβ.[36,37] In this study, we noted a high level of interaction

DOI: 10.1021/acs.biomac.9b01116
Biomacromolecules 2019, 20, 4208−4217

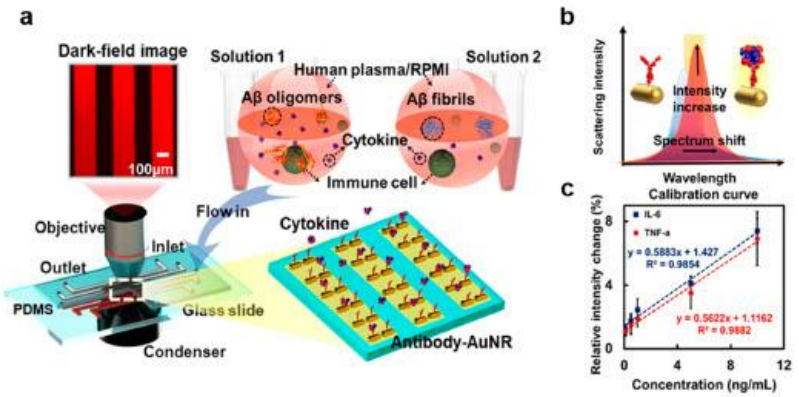

Figure 5. Schematics of the LSPR immunoassay. (a) LSPR immunoassay on Aβo- and Aβf-induced immune responses. Human immune cells (T cells, B cells, or THP-1 cells) were incubated with Aβo and $A\beta_f$ in human plasma or RPIM medium, respectively. The cellular responses were compared by detecting secreted concentrations of TNF and IL-6 in the medium using LSPR microfluidic chips in dark field. (b) Cytokine binding with AuNR–antibody conjugates altered the local refractive index and scattering cross section of the nanostructure, giving rise to a red shift in the SRP peak coupled with an elevated scattering intensity. The cytokines secreted were determined by changes to the scattering light intensity using an EMCCD. (c) Calibrations of cytokines TNF and IL-6 showing the relative intensity changes of the LSPR barcode with varied cytokine concentrations. The trendline equations and R^2 values are indicated. AuNR: gold nanorod.

between the Aβ species and monocytes for all conditions (i.e., 90–100% for all concentrations of $A\beta_O$ and 20–40% and 60–80% for low and high concentrations of $A\beta_f$, respectively; Figure 4). Overall, the monocytes displayed the highest association with Aβo compared to other types of blood cells.

In addition to monocytes, recruitment of T cells at Aβ plaques has been reported.[38] T cells play a major role in the pathophysiology of AD,[39] where the cellular response induced a near complete clearance of Aβ.[38] In addition, research has shown that AD patients exhibit an elevated T cell response to Aβ as compared to middle-aged healthy individuals.[40] The telomere length of T cells is dysregulated in AD patients, which may have consequential effects on the immune system and the brain.[41] In the present study, strong associations of $A\beta_O$ (i.e., 37–41%, 55–60%, and 66–67% for the three chosen concentrations) with T cells, independent of the presence of plasma proteins, were observed. In comparison, $A\beta_f$ showed lower interactions with the T cells (5.2 ± 0.1%, 38.2 ± 3.2%, and 51.8 ± 1.5% for the three chosen concentrations) without plasma proteins, and no significant interactions (<10%) with plasma proteins (Figure 4).

Dendritic cells (DCs), an initiator of adaptive immune responses, were reported to endocytose amyloid fibrils.[14] While the age-related behavior of DCs in enhancing peripheral inflammation has been documented, no significant changes in the secretion of chemokines or cytokines have been recorded with Aβ fibrils.[42] Here, association of 78–85% of $A\beta_O$ in the absence of plasma proteins and stronger association of 69–93% of Aβo with DCs were recorded in whole blood cells. $A\beta_f$, in contrast, showed weaker interactions with DCs than Aβo at 11.1 ± 3.7%, 35 ± 0.7%, and 56.5 ± 13% and 38.2 ± 3.3%, 69.2 ± 3.1%, and 71.2 ± 6.4% for the three concentrations with and without plasma proteins, respectively (Figure 4).

Previous studies revealed hindered circulation of low-density granulocytes in AD-type dementia patients, suggesting a damaging effect of AD on inflammatory cells in the periphery.[43] In the current study, a strong association of $A\beta_O$ with granulocytes (80–90%) was recorded with no considerable difference with and without plasma proteins. In the case of $A\beta_f$, the associations were determined to be 7.0 ± 2.9%, 21.6 ± 1.2%, and 35.7 ± 2.6% and 11.7 ± 0.4%, 38.5 ± 5.4%, and 51.8 ± 3.1% with and without plasma proteins, respectively (Figure 4). In addition to the blood cells characterized, a very low association of NK cells with $A\beta_O$ and no association with $A\beta_f$, especially with plasma proteins, were observed.

The production of antibodies by B cells toward $A\beta_{42}$ protofibrils has been shown to be much enhanced in AD patients as compared to healthy individuals.[44] In the present study, both Aβ species displayed interactions with B cells. Specifically, association of Aβo with B cells slightly decreased from whole blood to washed cells for the 3 concentrations of Aβo and significantly dropped from 12.8 ± 5.9%, 36.6 ± 6.0%, and 57.1 ± 0.9% to below 5% for the 3 concentrations of $A\beta_f$, respectively (Figure 4).

Aβo- and $A\beta_f$-Induced Immune Responses with and without Plasma Proteins. The deposition of Aβ peptide has been revealed to trigger a range of inflammation responses from immune cells to express cytokines and chemokines.[45] Laboratory and clinical investigations have shown evidence of increased release of pro-inflammatory cytokines in both the brain and plasma of AD patients.[46] In addition, plasma proteins including HSA have been demonstrated to mitigate Aβ amyloidosis and participate in AD-incited inflammatory responses in the brain. HSA binds 90% of plasma Aβ and could potentially affect their molecular distribution and pharmacokinetics.[47] Unveiling the influence of plasma proteins on the Aβ peptide-induced immune response and understanding the pro-inflammatory cytokine release profiles upon stimulation may offer new insights into Aβ-induced cytotoxicity to facilitate the development of AD therapy. Conventional cytokine detection methods such as enzyme-linked immunosorbent assay (ELISA) usually require laborious regent

DOI: 10.1021/acs.biomac.9b01116
Biomacromolecules 2019, 20, 4208–4217

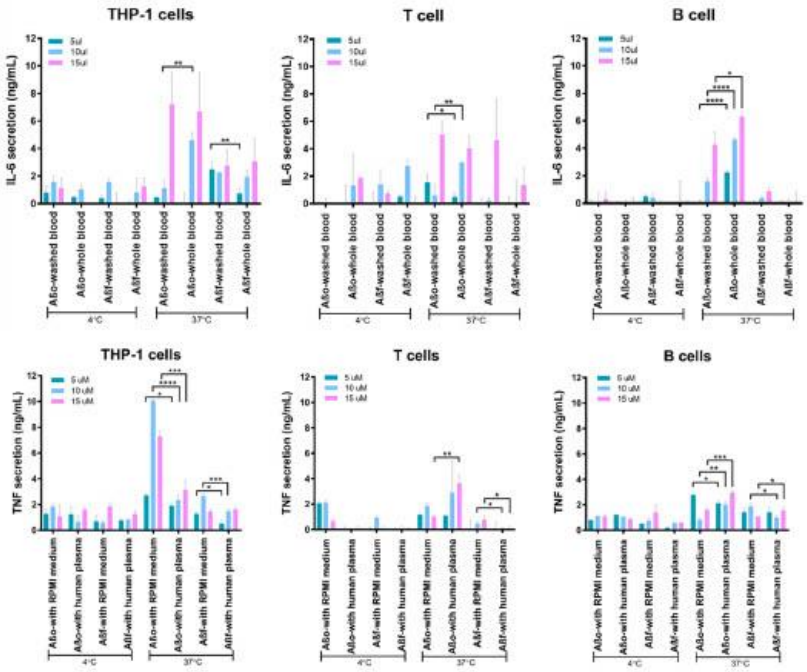

Figure 6. Aβ-induced immune responses of human immune cells. Cytokine secretion profiles for THP-1 cells, T cells, and B cells incubated with $A\beta_O$ and $A\beta_f$ in human plasma or RPMI-1640 medium. The assay was performed in triplicate. The error bars indicate standard deviations (*, $P < 0.05$; **, $P < 0.01$; ***, $P < 0.001$; and ****, $P < 0.0001$).

processing procedures, including multiple steps of staining, washing, and blocking, and posing challenges in real-time analysis of dynamic molecular release processes.[20] In this study, we performed a label-free microfluidic-based LSPR immunoassay for real-time detection of multiple cytokines secreted by three types of immune cells, after coculturing the cells with $A\beta_O$ or $A\beta_f$. The immune responses induced by $A\beta_O$ and $A\beta_f$ with and without plasma proteins were assessed by the levels of cytokine secretion.

Immune cell lines (T cells, B cells, or monocytic cells) were incubated with the two types of Aβ aggregates in human plasma and RPMI medium at 4 and 37 °C, respectively. LSPR immunoassay chips consisting of antibody-functionalized gold nanorods (AuNRs) were used to detect TNF and IL-6 secreted by the immune cells (Figure 5a). Cytokine binding with AuNR−antibody conjugate altered the localized-refractive index and enlarged the scattering cross section of the nanostructure. The plasmon resonance gave rise to a red shift in the scattering spectrum, coupled with an increased scattering intensity (Figure 5b). Images of the sensing spot arrays were acquired in real-time by an ultrasensitive electron multiplying CCD (EMCCD, Photometrics). The scattering intensities of the sensing spots were processed by MATLAB and converted to cytokine concentrations based on pre-established calibrations (Figure 5c). More pronounced inflammatory responses were observed for immune cells exposed to the Aβ species at 37 °C than at 4 °C due to higher cell activity and metabolism (Figure 6). Specifically, $A\beta_O$ induced overall heightened immune responses as compared to $A\beta_f$ at 37 °C, suggesting stronger interaction and toxicity of the former with the immune cells. THP-1 cells (as a model system for monocytes), in particular, displayed a prominent pro-inflammatory cytokine secretion upon exposure to $A\beta_O$, consistent with the observed monocyte association with the Aβ aggregate (Figure 4).

Contrasting effects of plasma proteins on $A\beta_O$- and $A\beta_f$-induced immune responses were observed at 37 °C. Whereas $A\beta_f$ displayed overall suppressed immune responses after interacting with plasma proteins for all three types of immune cells, $A\beta_O$-associated immune toxicity was mostly promoted in the presence of plasma proteins, except for TNF expression from the THP-1 cells. Such differential immune toxicity of Aβ depositions can be attributed to two main factors: size and hydrophobicity, correlating to the capacities of the Aβ species and their protein-coronae to bind and penetrate the immune cell membranes. It was reported that amylin oligomers of smaller size and higher hydrophobicity elicited a stronger immune response than their counterparts with similar size but less solvent-exposed hydrophobic residues.[48,49] As such, binding of $A\beta_O$ with serum albumin in plasma proteins inhibited the peptide aggregation to maintain their small size and surface hydrophobicity, facilitating immune cell inter-

DOI: 10.1021/acs.biomac.9b01116
Biomacromolecules 2019, 20, 4208−4217

actions to elevate immune responses.[35] In contrast, $A\beta_f$ with lower structural plasticity and less exposed hydrophobic residues tends to bind to plasma proteins via charged and polar groups, resulting in a larger colloidal-like amyloid-protein corona while displaying weaker toxicity. It should be noted that TNF expression from THP-1 cells could be promoted through receptor-specific signaling pathways such as the Mac-1 receptor.[50] Hence, the formation of an $A\beta_O$-plasma protein corona could potentially shield the exposed $A\beta_O$ activation motifs and drastically prohibit TNF secretion. Such a phenomenon was not observed for Mac-1 receptor-negative T-cells and B-cells.

CONCLUSION

Amyloidosis has been extensively investigated for the past decades, driven by the urgent need to find a cure for amyloid diseases.[1] Much of this research emphasis has been centered on the amyloid hypothesis[51] and its pathological implications. The oligomers are widely viewed as the most toxic products of protein aggregation as established by extensive *in vitro* and *in vivo* data,[52,53] while amyloid fibrils are generally considered as benign despite experimental discrepancies.[54] Here, we have revealed a convoluted relationship between the amyloidosis and immunogenicity of $A\beta_{1-42}$, using a high-throughput blood assay and a label-free microfluidic-based LSPR immunoassay. Specifically, $A\beta_O$ displayed strong blood cell association independent of plasma proteins. In contrast, binding of $A\beta_f$ with the cells was weaker and was further dampened in whole blood as a result of a protein corona. Consistently, the LSPR immunoassay revealed elevated cytokine secretion of immune cells against both $A\beta_O$ and $A\beta_\theta$ especially more so for the oligomers. The $A\beta_f$-elicited immune response was screened by plasma proteins, via a protein corona mediated by nonspecific forces. The oligomers, on the other hand, maintained their capacity for immune cell association due to their small size and finite hydrophobicity. This study has implicated the intertwined relationship between the amyloidosis and immunogenicity of $A\beta$, two aspects underlining the pathological cascade and therapeutic solution of AD.

ASSOCIATED CONTENT

Supporting Information

The Supporting Information is available free of charge on the ACS Publications website at DOI: 10.1021/acs.biomac.9b01116.

Fabrication and measurement details of LSPR immunoassay; RP-HPLC elution of $A\beta$m, $A\beta$o, and $A\beta_f$ structures; and examples of gating related to cell association with ThT-labeled $A\beta$ (PDF)

AUTHOR INFORMATION

Corresponding Authors

*E-mail: thomas.p.davis@monash.edu.
*E-mail: pengyuc@auburn.edu.
*E-mail: skent@unimelb.edu.au.
*E-mail: pu-chun.ke@monash.edu.

ORCID

Anthony Wayne Purcell: 0000-0003-0532-8331
Thomas P. Davis: 0000-0003-2581-4986
Pengyu Chen: 0000-0003-3380-872X
Stephen J. Kent: 0000-0002-8539-4891
Pu Chun Ke: 0000-0003-2134-0859

Author Contributions

P.C.K. and P.C. designed the project. A.F. performed the TEM, ThT, and cell viability assays. S.J.K. and H.G.K. designed the blood assay. H.G.K. and A.F. performed the blood assay and data analysis. W.Y., C.W., and P.C. designed and performed the LSPR immunoassay and conducted data analysis. All authors provided feedback and agreed on the content of the manuscript.

Notes

The authors declare no competing financial interest.

ACKNOWLEDGMENTS

This work was supported by ARC Grant CE140100036 (T.P.D.), the National Science Foundation Grant CBET-1701363 (P.C.), the National Institutes of Health Grant R35GM133795 (P.C.), and AFTAM Research Collaboration Award (T.P.D. and P.C.K.). HIM imaging was performed by Anders Barlow at the MCFP platform, University of Melbourne.

REFERENCES

(1) Ke, P. C.; Sani, M. A.; Ding, F.; Kakinen, A.; Javed, I.; Separovic, F.; Davis, T. P.; Mezzenga, R. Implications of Peptide Assemblies in Amyloid Diseases. *Chem. Soc. Rev.* **2017**, *46*, 6492−6531.

(2) Ballard, C.; Gauthier, S.; Corbett, A.; Brayne, C.; Aarsland, D.; Jones, E. Alzheimer's Disease. *Lancet* **2011**, *377*, 1019−1031.

(3) Tublin, J. M.; Adelstein, J. M.; Del Monte, F.; Combs, C. K.; Wold, L. E. Getting to the Heart of Alzheimer Disease. *Circ. Res.* **2019**, *124*, 142−149.

(4) Mackic, J. B.; Bading, J.; Ghiso, J.; Walker, L.; Wisniewski, T.; Frangione, B.; Zlokovic, B. V. Circulating Amyloid-Beta Peptide Crosses the Blood-Brain Barrier in Aged Monkeys and Contributes to Alzheimer's Disease Lesions. *Vasc. Pharmacol.* **2002**, *38*, 303−313.

(5) Biere, A. L.; Ostaszewski, B.; Stimson, E. R.; Hyman, B. T.; Maggio, J. E.; Selkoe, D. J. Amyloid Beta-Peptide is Transported on Lipoproteins and Albumin in Human Plasma. *J. Biol. Chem.* **1996**, *271*, 32916−32922.

(6) Matsubara, E.; Sekijima, Y.; Tokuda, T.; Urakami, K.; Amari, M.; Shizuka-Ikeda, M.; Tomidokoro, Y.; Ikeda, M.; Kawarabayashi, T.; Harigaya, Y.; Ikeda, S.; Murakami, T.; Abe, K.; Otomo, E.; Hirai, S.; Frangione, B.; Ghiso, J.; Shoji, M. Soluble Abeta Homeostasis in AD and DS: Impairment of Anti-Amyloidogenic Protection by Lipoproteins. *Neurobiol. Aging* **2004**, *25*, 833−841.

(7) Finn, T. E.; Nunez, A. C.; Sunde, M.; Easterbrook-Smith, S. B. Serum Albumin Prevents Protein Aggregation and Amyloid Formation and Retains Chaperone-like Activity in the Presence of Physiological Ligands. *J. Biol. Chem.* **2012**, *287*, 21530−21540.

(8) Algamal, M.; Milojevic, J.; Jafari, N.; Zhang, W.; Melacini, G. Mapping the Interactions between the Alzheimer's Abeta-peptide and Human Serum Albumin beyond Domain Resolution. *Biophys. J.* **2013**, *105*, 1700−1709.

(9) Kakinen, A.; Javed, I.; Faridi, A.; Davis, T. P.; Ke, P. C. Serum Albumin Impedes the Amyloid Aggregation and Hemolysis of Human Islet Amyloid Polypeptide and Alpha Synuclein. *Biochim. Biophys. Acta, Biomembr.* **2018**, *1860*, 1803−1809.

(10) Ramanathan, A.; Nelson, A. R.; Sagare, A. P.; Zlokovic, B. V. Impaired Vascular-Mediated Clearance of Brain Amyloid Beta in Alzheimer's Disease: the Role, Regulation and Restoration of LRP1. *Front. Aging Neurosci.* **2015**, *7*, 136.

(11) Marsh, S. E.; Abud, E. M.; Lakatos, A.; Karimzadeh, A.; Yeung, S. T.; Davtyan, H.; Fote, G. M.; Lau, L.; Weinger, J. G.; Lane, T. E.; Inlay, M. A.; Poon, W. W.; Blurton-Jones, M. The Adaptive Immune System Restrains Alzheimer's Disease Pathogenesis by Modulating Microglial Function. *Proc. Natl. Acad. Sci. U. S. A.* **2016**, *113*, E1316−E1325.

DOI: 10.1021/acs.biomac.9b01116
Biomacromolecules 2019, 20, 4208−4217

(12) Rogers, J.; Strohmeyer, R.; Kovelowski, C. J.; Li, R. Microglia and Inflammatory Mechanisms in the Clearance of Amyloid Beta Peptide. *Glia* **2002**, *40*, 260−269.
(13) Wang, Z. T.; Zhong, X. L.; Tan, M. S.; Wang, H. F.; Tan, C. C.; Zhang, W.; Zheng, Z. J.; Kong, L. L.; Tan, L.; Sun, L. Association of Lectin-like Oxidized Low Density Lipoprotein Receptor 1 (OLR1) Polymorphisms with Late-Onset Alzheimer Disease in Han Chinese. *Ann. Transl. Med.* **2018**, *6*, 172.
(14) Marx, F.; Blasko, I.; Pavelka, M.; Grubeck-Loebenstein, B. The Possible Role of the Immune System in Alzheimer's Disease. *Exp. Gerontol.* **1998**, *33*, 871−881.
(15) Rogers, J.; Li, R.; Mastroeni, D.; Grover, A.; Leonard, B.; Ahern, G.; Cao, P.; Kolody, H.; Vedders, L.; Kolb, W. P.; Sabbagh, M. Peripheral Clearance of Amyloid Beta Peptide by Complement C3-Dependent Adherence to Erythrocytes. *Neurobiol. Aging* **2006**, *27*, 1733−1739.
(16) Pesini, P.; Perez-Grijalba, V.; Monleon, I.; Boada, M.; Tarraga, L.; Martinez-Lage, P.; San-Jose, I.; Sarasa, M. Reliable Measurements of the Beta-Amyloid Pool in Blood Could Help in the Early Diagnosis of AD. *Int. J. Alzheimer's Dis.* **2012**, *2012*, 604141.
(17) Bellomo, G.; Bologna, S.; Cerofolini, L.; Paciotti, S.; Gatticchi, L.; Ravera, E.; Parnetti, L.; Fragai, M.; Luchinat, C. Dissecting the Interactions between Human Serum Albumin and α-Synuclein: New Insights on the Factors Influencing α-Synuclein Aggregation in Biological Fluids. *J. Phys. Chem. B* **2019**, *123*, 4380−4386.
(18) Weiss, A. C. G.; Kelly, H. G.; Faria, M.; Besford, Q. A.; Wheatley, A. K.; Ang, C. S.; Crampin, E. J.; Caruso, F.; Kent, S. J. Link between Low-Fouling and Stealth: A Whole Blood Biomolecular Corona and Cellular Association Analysis on Nanoengineered Particles. *ACS Nano* **2019**, *13*, 4980−4991.
(19) Glass, J. J.; Chen, L.; Alcantara, S.; Crampin, E. J.; Thurecht, K. J.; De Rose, R.; Kent, S. J. Charge Has a Marked Influence on Hyperbranched Polymer Nanoparticle Association in Whole Human Blood. *ACS Macro Lett.* **2017**, *6*, 586−592.
(20) Javed, I.; He, J.; Kakinen, A.; Faridi, A.; Yang, W.; Davis, T. P.; Ke, P. C.; Chen, P. Probing the Aggregation and Immune Response of Human Islet Amyloid Polypeptides with Ligand-Stabilized Gold Nanoparticles. *ACS Appl. Mater. Interfaces* **2019**, *11*, 10462−10471.
(21) Kuo, Y. M.; Kokjohn, T. A.; Kalback, W.; Luehrs, D.; Galasko, D. R.; Chevallier, N.; Koo, E. H.; Emmerling, M. R.; Roher, A. E. Amyloid-Beta Peptides Interact with Plasma Proteins and Erythrocytes: Implications for Their Quantitation in Plasma. *Biochem. Biophys. Res. Commun.* **2000**, *268*, 750−756.
(22) Pilkington, E. H.; Gustafsson, O. J. R.; Xing, Y.; Hernandez-Fernaud, J.; Zampronio, C.; Kakinen, A.; Faridi, A.; Ding, F.; Wilson, P.; Ke, P. C.; Davis, T. P. Profiling the Serum Protein Corona of Fibrillar Human Islet Amyloid Polypeptide. *ACS Nano* **2018**, *12*, 6066−6078.
(23) Sudhakar, S.; Kalipillai, P.; Santhosh, P. B.; Mani, E. Role of Surface Charge of Inhibitors on Amyloid Beta Fibrillation. *J. Phys. Chem. C* **2017**, *121*, 6339−6348.
(24) Knowles, T. P.; Vendruscolo, M.; Dobson, C. M. The Amyloid State and Its Association with Protein Misfolding Diseases. *Nat. Rev. Mol. Cell Biol.* **2014**, *15*, 384−396.
(25) Shozawa, H.; Oguchi, T.; Tsuji, M.; Yano, S.; Kiuchi, Y.; Ono, K. Supratherapeutic Concentrations of Cilostazol Inhibits Beta-Amyloid Oligomerization in Vitro. *Neurosci. Lett.* **2018**, *677*, 19−25.
(26) Wiltzius, J. J.; Sievers, S. A.; Sawaya, M. R.; Eisenberg, D. Atomic structures of IAPP (amylin) Fusions Suggest a Mechanism for Fibrillation and the Role of Insulin in the Process. *Protein Sci.* **2009**, *18*, 1521−1530.
(27) Zhang, X.; St. Clair, J. R.; London, E.; Raleigh, D. P. Islet Amyloid Polypeptide Membrane Interactions: Effects of Membrane Composition. *Biochemistry* **2017**, *56*, 376−390.
(28) Pilkington, E. H.; Lai, M.; Ge, X.; Stanley, W. J.; Wang, B.; Wang, M.; Kakinen, A.; Sani, M. A.; Whittaker, M. R.; Gurzov, E. N.; Ding, F.; Quinn, J. F.; Davis, T. P.; Ke, P. C. Star Polymers Reduce Islet Amyloid Polypeptide Toxicity via Accelerated Amyloid Aggregation. *Biomacromolecules* **2017**, *18*, 4249−4260.
(29) Haataja, L.; Gurlo, T.; Huang, C. J.; Butler, P. C. Islet Amyloid in Type 2 Diabetes, and the Toxic Oligomer Hypothesis. *Endocr. Rev.* **2008**, *29*, 303−316.
(30) Faridi, A.; Sun, Y.; Okazaki, Y.; Peng, G.; Gao, J.; Kakinen, A.; Faridi, P.; Zhao, M.; Javed, I.; Purcell, A. W.; Davis, T. P.; Lin, S.; Oda, R.; Ding, F.; Ke, P. C. Mitigating Human IAPP Amyloidogenesis In Vivo with Chiral Silica Nanoribbons. *Small* **2018**, *14*, No. 1802825.
(31) Cao, W.; Zheng, H. Peripheral Immune System in Aging and Alzheimer's Disease. *Mol. Neurodegener.* **2018**, *13*, 51.
(32) Solana, C.; Tarazona, R.; Solana, R. Immunosenescence of Natural Killer Cells, Inflammation, and Alzheimer's Disease. *Int. J. Alzheimer's Dis.* **2018**, *2018*, 3128758.
(33) Cedervall, T.; Lynch, I.; Lindman, S.; Berggård, T.; Thulin, E.; Nilsson, H.; Dawson, K. A.; Linse, S. Understanding the Nanoparticle-Protein Corona Using Methods to Quantify Exchange Rates and Affinities of Proteins for Nanoparticles. *Proc. Natl. Acad. Sci. U. S. A.* **2007**, *104*, 2050−2055.
(34) Reyes Barcelo, A. A.; Gonzalez-Velasquez, F. J.; Moss, M. A. Soluble Aggregates of the Amyloid-Beta Peptide are Trapped by Serum Albumin to Enhance Amyloid-Beta Activation of Endothelial Cells. *J. Biol. Eng.* **2009**, *3*, 5.
(35) Milojevic, J.; Esposito, V.; Das, R.; Melacini, G. Understanding the Molecular Basis for the Inhibition of the Alzheimer's Abeta-Peptide Oligomerization by Human Serum Albumin Using Saturation Transfer Difference and Off-resonance Relaxation NMR Spectroscopy. *J. Am. Chem. Soc.* **2007**, *129*, 4282−4290.
(36) Wang, M. M.; Miao, D.; Cao, X. P.; Tan, L.; Tan, L. Innate Immune Activation in Alzheimer's Disease. *Ann. Transl. Med.* **2018**, *6*, 177.
(37) Michaud, J. P.; Bellavance, M. A.; Prefontaine, P.; Rivest, S. Real-Time in Vivo Imaging Reveals the Ability of Monocytes to Clear Vascular Amyloid Beta. *Cell Rep.* **2013**, *5*, 646−653.
(38) Fisher, Y.; Nemirovsky, A.; Baron, R.; Monsonego, A. T Cells Specifically Targeted to Amyloid Plaques Enhance Plaque Clearance in a Mouse Model of Alzheimer's Disease. *PLoS One* **2010**, *5*, No. e10830.
(39) Bondy, B.; Hofmann, M.; Muller-Spahn, F.; Witzko, M.; Hock, C. Reduced Beta-Amyloid Response in Lymphocytes of Patients with Alzheimer's Disease. *Pharmacopsychiatry* **1995**, *28*, 143−146.
(40) Monsonego, A.; Zota, V.; Karni, A.; Krieger, J. I.; Bar-Or, A.; Bitan, G.; Budson, A. E.; Sperling, R.; Selkoe, D. J.; Weiner, H. L. Increased T Cell Reactivity to Amyloid Beta Protein in Older Humans and Patients with Alzheimer Disease. *J. Clin. Invest.* **2003**, *112*, 415−422.
(41) Panossian, L. A.; Porter, V. R.; Valenzuela, H. F.; Zhu, X.; Reback, E.; Masterman, D.; Cummings, J. L.; Effros, R. B. Telomere Shortening in T Cells Correlates with Alzheimer's Disease Status. *Neurobiol. Aging* **2003**, *24*, 77−84.
(42) Agrawal, S.; Abud, E. M.; Snigdha, S.; Agrawal, A. IgM Response against Amyloid-Beta in Aging: a Potential Peripheral Protective Mechanism. *Alzheimer's Res. Ther.* **2018**, *10*, 81.
(43) Jaremo, P.; Milovanovic, M.; Buller, C.; Nilsson, S.; Winblad, B. Alzheimer's Disease and Granulocyte Density Diversity. *Eur. J. Clin. Invest.* **2013**, *43*, 545−548.
(44) Sollvander, S.; Ekholm-Pettersson, F.; Brundin, R. M.; Westman, G.; Kilander, L.; Paulie, S.; Lannfelt, L.; Sehlin, D. Increased Number of Plasma B Cells Producing Autoantibodies Against Abeta42 Protofibrils in Alzheimer's Disease. *J. Alzheimer's Dis.* **2015**, *48*, 63−72.
(45) Cao, W.; Zheng, H. Peripheral Immune System in Aging and Alzheimer's Disease. *Mol. Neurodegener.* **2018**, *13*, 51.
(46) Zheng, C.; Zhou, X. W.; Wang, J. Z. The Dual Roles of Cytokines in Alzheimer's Disease: Update on Interleukins, TNF-alpha, TGF-beta and IFN-gamma. *Transl. Neurodegener.* **2016**, *5*, 7.
(47) Lexa, K. W.; Dolghih, E.; Jacobson, M. P. A Structure-based Model for Predicting Serum Albumin Binding. *PLoS One* **2014**, *9*, No. e93323.
(48) Mannini, B.; Mulvihill, E.; Sgromo, C.; Cascella, R.; Khodarahmi, R.; Ramazzotti, M.; Dobson, C. M.; Cecchi, C.; Chiti,

DOI: 10.1021/acs.biomac.9b01116
Biomacromolecules 2019, 20, 4208−4217

F. Toxicity of Protein Oligomers is Rationalized by A Function Combining Size and Surface Hydrophobicity. *ACS Chem. Biol.* **2014**, *9*, 2309−2317.
(49) Campioni, S.; Mannini, B.; Zampagni, M.; Pensalfini, A.; Parrini, C.; Evangelisti, E.; Relini, A.; Stefani, M.; Dobson, C. M.; Cecchi, C.; Chiti, F. A Causative Link between the Structure of Aberrant Protein Oligomers and Their Toxicity. *Nat. Chem. Biol.* **2010**, *6*, 140−147.
(50) Deng, Z. J.; Liang, M.; Monteiro, M.; Toth, I.; Minchin, R. F. Nanoparticle-induced Unfolding of Fibrinogen Promotes Mac-1 Receptor Activation and Inflammation. *Nat. Nanotechnol.* **2011**, *6*, 39−44.
(51) Hardy, J.; Selkoe, D. J. The Amyloid Hypothesis of Alzheimer's Disease: Progress and Problems on the Road to Therapeutics. *Science* **2002**, *297*, 353−356.
(52) Kayed, R.; Head, E.; Thompson, J. L.; McIntire, T. M.; Milton, S. C.; Cotman, C. W.; Glabe, C. G. Common Structure of Soluble Amyloid Oligomers Implies Common Mechanism of Pathogenesis. *Science* **2003**, *300*, 486−489.
(53) Benilova, I.; Karran, E.; De Strooper, B. The Toxic Aβ Oligomer and Alzheimer's Disease: An Emperor in Need of Clothes. *Nat. Neurosci.* **2012**, *15*, 349−357.
(54) Krotee, P.; Rodriguez, J. A.; Sawaya, M. R.; Cascio, D.; Reyes, F. E.; Shi, D.; Hattne, J.; Nannenga, B. L.; Oskarsson, M. E.; Philipp, S.; Griner, S.; Jiang, L.; Glabe, C. G.; Westermark, G. T.; Gonen, T.; Eisenberg, D. S. Atomic Structures of Fibrillar Segments of hIAPP Suggest Tightly Mated β-sheets are Important for Cytotoxicity. *eLife* **2017**, *6*, No. e19273.

DOI: 10.1021/acs.biomac.9b01116
Biomacromolecules 2019, 20, 4208−4217

Supporting Information

Differential roles of plasma protein corona on immune cell association and cytokine secretion of oligomeric and fibrillar beta-amyloid

Ava Faridi,[1] Wen Yang,[2] Hannah Gabrielle Kelly,[3,4] Chuanyu Wang,[2] Pouya Faridi,[5] Anthony W. Purcell,[5] Thomas P. Davis,[1,6*] Pengyu Chen,[2*] Stephen J. Kent[3,4,7*] and Pu Chun Ke[1*]

[1]ARC Centre of Excellence in Convergent Bio-Nano Science and Technology, Monash Institute of Pharmaceutical Sciences, Monash University, 381 Royal Parade, Parkville, VIC 3052, Australia

[2]Materials Research and Education Center, Auburn University, Auburn, AL 36849, United States

[3]Department of Microbiology and Immunology, Peter Doherty Institute for Infection and Immunity, University of Melbourne, Melbourne, Victoria, Australia

[4]ARC Centre for Excellence in Convergent Bio-Nano Science and Technology, University of Melbourne, Melbourne, Australia

[5]Infection and Immunity Program & Department of Biochemistry and Molecular Biology, Biomedicine Discovery Institute, Monash University, Clayton, Victoria 3800, Australia

[6]Australian Institute for Bioengineering and Nanotechnology, The University of Queensland, Brisbane Qld 4072, Australia

[7]Melbourne Sexual Health Clinic and Infectious Diseases Department, Alfred Hospital, Monash University Central Clinical School, Carlton, Victoria, Australia

Corresponding Authors

Pengyu Chen: pengyuc@auburn.edu; Thomas P. Davis: thomas.p.davis@monash.edu; Stephen Kent: skent@unimelb.edu.au; Pu Chun Ke: pu-chun.ke@monash.edu.

Localized surface plasmon resonance (LSPR) immunoassay chip fabrication

PDMS microfluidic-pattering layer preparation

The mold wafer for parallel microfluidic channels (200 μm (W) × 2.5 cm (L) × 50 μm) was fabricated on a silicon substrate by photolithography. A liquid PDMS (polydimethylsiloxane, Sylgard-184, Dow Corning) pre-polymer and cross linker were then mixed (10:1) and degassed twice, and poured onto the silicon mode wafer. The device was incubated over 6 h at 70 °C. After that, the PDMS microfluidic-pattering layer was peeled off from the mold wafer. Inlets and outlets of the follow channels were created by a hole puncher with a diameter of 1 mm.

Au nanorod barcode patterning

Glass slides were first washed by deionized (DI) water and immersed in Piranha solution (H_2SO_4:H_2O_2 = 3:1 v/v) for 10 min. The cleaned slides were rinsed with DI water and kept in an ultrasonic bath for 15 min, and then thoroughly washed with DI water. The prepared glass slides were fully dried at 80 °C. To create a negatively charged surface, oxygen plasma at 60 W (PE-50, Plasma Etch Inc.) was applied onto a glass substrate for 4 min. The PDMS microfluidic-pattering layer was quickly attached onto the surface of plasma-treated glass for Au nanorod (AuNR) barcode patterning. A suspension of CTAB-coated AuNRs (Nanoseedz, NR-40-650-10) was loaded into the channels and incubated overnight. The positively charged AuNRs were immobilized onto the glass surface through electrostatic interaction to form the barcode pattern on the glass substrate. Unbound AuNRs were washed away by DI water. The PDMS patterning layer was then carefully removed and a free PDMS flow channel layer (from the same mask) was attached perpendicularly to the AuNRs barcode patterns. Approximately 1 mM of 11-mercaptoundecanoic acid (Sigma-Aldrich, USA) was loaded into the channels to replace the CTAB layer on the AuNRs surface and incubated overnight. 0.1 M NHS (*N*-hydroxysuccinimide, Thermo Scientific) and 0.4 M EDC (1-ethyl-3-[3-(dimethylamino)propyl] carbodiimide hydrochloride, Thermo Scientific) prepared in 0.1 M MES (1-ethyl-3-[3-

(dimethylamino)propyl] carbodiimide hydrochloride Thermo Scientific) were mixed in equal volume. The mixture was then loaded into microfluidics channels, and incubated for 40 min. Probe antibody solutions (anti-human IL-6 or anti-human TNF-α, eBioscience, USA) in 50 μg/mL were injected into the channels and incubated for 1 h. All the excessive chemicals and molecules in each step were washed away by 1× PBS at 1.5 μL/min for 6 min (**Fig. S1**).

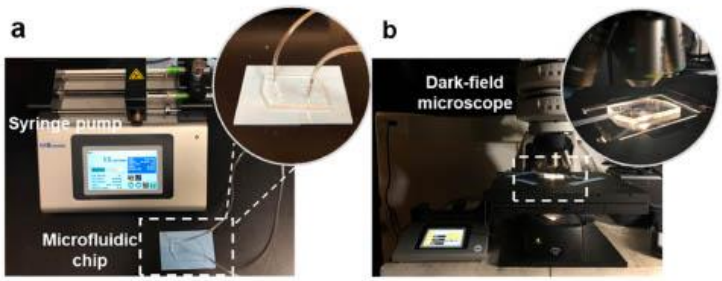

Figure S1. (a) Au nanorod (AuNR) barcode patterning. AuNRs and functional chemical solution were loaded into a microfluidic chip using a syringe. The liquid speed was precisely controlled by a syringe pump. (b) LSPR immunoassay under a dark-field microscope. A prepared LSPR chip was mounted on the sample stage. Scattering light was collected by a 10× objective lens. Dark-field images were captured by an EMCCD camera and analyzed by a customized Matlab code.

Reversed-phase high performance liquid chromatography (RP-HPLC). Samples of Aβm, Aβo and $A\beta_f$ (300 μM) were dissolved in 10% acetic acid and ran on a 4.6-mm (internal diameter) × 100-mm (length) monolithic reversed-phase C18 high-performance liquid chromatography (HPLC) column of Chromolith SpeedROD; Merck Millipore, Darmstadt, Germany, using an ÄKTAmicro HPLC system (GE Healthcare, Little Chalfont, UK). Buffer A (0.1% trifluoroacetic acid; Thermo Fisher Scientific) and buffer B (80% acetonitrile, 0.1% trifluoroacetic acid; Thermo Fisher Scientific) were used in the mobile phase. After a blank

run, the Aβ peptide samples were injected into the column and separated using the following chromatographic conditions: 2-15% buffer B over 0.25 min (2 mL/min), 15-30% buffer B over 4 min (2 mL/min), 30-40% buffer B over 8 min (2 mL/min), 40-45% buffer B over 10 min (2 mL/min), 45-99% buffer B over 2 min (1 mL/min), 99-100% over 2 min (1mL/min), and re-equilibrated 6 min in 2% buffer B at 2 mL/min.

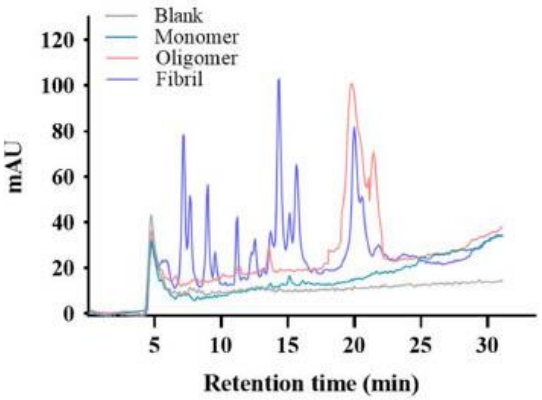

Fig. S2. RP-HPLC elution of Aβm, Aβo and $A\beta_f$ structures. Longer retention time corresponded to increased hydrophobicity. Compared with Aβo, the oligomeric structures in the sample of $A\beta_f$ were mostly depleted and converted into various heterogeneous and highly hydrophilic structures especially at earlier retention times. The overall data confirmed a conformational conversion of Aβm to $A\beta_f$ over time, from disordered to β-sheet-dominant structures. mAU: milli-absorbance unit. Aβ concentration: 300 μM. For simplicity of comparison, this figure represents the first 30 min of HPLC runs (as there were no major differences between the curves after 30 min).

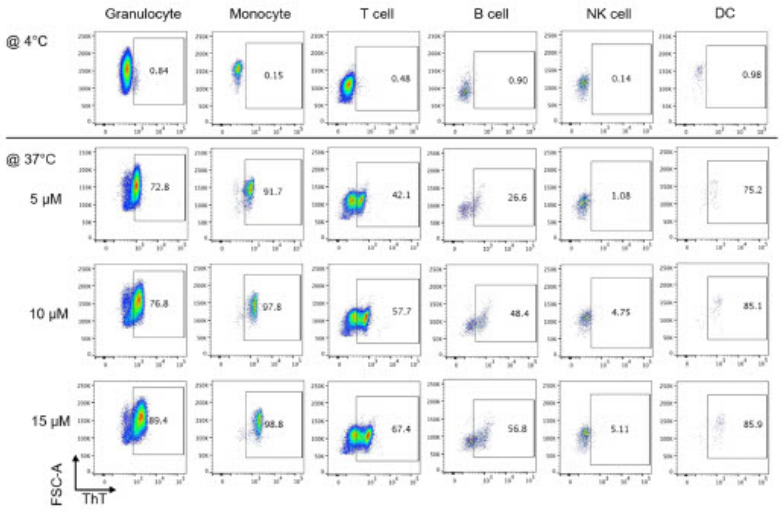

Figure S3. Gating was applied to identify the population of immune cells with ThT-labelled Aβo. Side and forward scatter were used to locate white blood cells before doublets were excluded. The following cell types were identified based on expression of surface markers or scatter: high side scatter granulocytes; CD3+ T cells; CD14+ monocytes; CD56+ NK cells; CD19+ B cells; and Lin1-HLA-DR+ dendritic cells. The percentage of each cell type positive for the ThT-labelled Aβ was recorded.

Chapter 3

Mitigating human IAPP amyloidogenesis in vivo with chiral silica nanoribbons

1. Declaration and rationale

“This chapter was published as Faridi, A., Sun, Y., Okazaki, Y., Peng, G., Gao, J., Kakinen, A., Faridi, P., Zhao, M., Javed, I., Purcell, A.W., Davis, T.P., Lin, S., Oda, R., Ding, F., Ke, P.C., Mitigating Human IAPP Amyloidogenesis In Vivo with Chiral Silica Nanoribbons, (2018) ***Small***. Reprinted with permission from reference[122] Copyright 2018Wiley."

In this chapter, the use of mesoscopic chiral silica nanostructures against IAPP aggregation was studied for the first time *in vitro* and in an embryonic zebrafish model. This study offered a new strategy for amyloidosis inhibition with chiral nanomaterials.

NANO · MICRO small
www.small-journal.com

Mitigating Human IAPP Amyloidogenesis In Vivo with Chiral Silica Nanoribbons

Ava Faridi, Yunxiang Sun, Yutaka Okazaki, Guotao Peng, Jie Gao, Aleksandr Kakinen, Pouya Faridi, Mei Zhao, Ibrahim Javed, Anthony W. Purcell, Thomas P. Davis, Sijie Lin,* Reiko Oda,* Feng Ding, and Pu Chun Ke**

Amyloid fibrils generally display chirality, a feature which has rarely been exploited in the development of therapeutics against amyloid diseases. This study reports, for the first time, the use of mesoscopic chiral silica nanoribbons against the in vivo amyloidogenesis of human islet amyloid polypeptide (IAPP), the peptide whose aggregation is implicated in type 2 diabetes. The thioflavin T assay and transmission electron microscopy show accelerated IAPP fibrillization through elimination of the nucleation phase and shortening of the elongation phase by the nanostructures. Coarse-grained simulations offer complementary molecular insights into the acceleration of amyloid aggregation through their nonspecific binding and directional seeding with the nanostructures. This accelerated IAPP fibrillization translates to reduced toxicity, especially for the right-handed silica nanoribbons, as revealed by cell viability, helium ion microscopy, as well as zebrafish embryo survival, developmental, and behavioral assays. This study has implicated the potential of employing chiral nanotechnologies against the mesoscopic enantioselectivity of amyloid proteins and their associated diseases.

1. Introduction

The aggregation of human islet amyloid polypeptide (IAPP) into insoluble amyloid fibrils and plaques is a hallmark of type 2 diabetes,[1,2] a metabolic disease and a global epidemic impacting an estimated population of 360 million. IAPP is a 37-residue amphiphilic peptide secreted by pancreatic beta cell islets, and is stabilized intracellularly by the presence of insulin, low pH, physiological metal ions (such as zinc), as well as zinc-coordinated complexation of C-peptide and IAPP at a specific stoichiometric ratio.[3–7] A major strategy against IAPP amyloidogenesis has involved the use of small molecules (e.g., polyphenols such as curcumin, resveratrol, and epigallocatechin gallate), chaperone proteins, or engineered nanostructures of dendritic polymers, graphene oxide nanosheets, and gold nanoparticles, exploiting the capacities of these "ligands" in mediating hydrogen-bonding, hydrophobic interaction, or π-stacking with the amyloid protein.[8] While these approaches are designed to simultaneously inhibit protein aggregation and toxicity, and almost exclusively in vitro, we have recently shown that star polymer poly (2-hydroxyethyl acrylate) could accelerate the nucleation and elongation phases of IAPP fibrillization, while eliminating the production of toxic IAPP oligomers in vitro and ex vivo.[9] In addition, we have demonstrated that the

A. Faridi, Dr. A. Kakinen, I. Javed, Prof. T. P. Davis, Prof. P. C. Ke
ARC Centre of Excellence in Convergent Bio-Nano Science and Technology
Monash Institute of Pharmaceutical Sciences
Monash University
381 Royal Parade, Parkville, VIC 3052, Australia
E-mail: thomas.p.davis@monash.edu; pu-chun.ke@monash.edu
A. Faridi, Dr. G. Peng, M. Zhao, Prof. S. Lin
College of Environmental Science and Engineering
Shanghai Institute of Pollution Control and Ecological Security
Biomedical Multidisciplinary Innovation Research Institute
Shanghai East Hospital
State Key Laboratory of Pollution Control and Resource Reuse
Tongji University
1239 Siping Road, Shanghai 200092, China
E-mail: lin.sijie@tongji.edu.cn
The ORCID identification number(s) for the author(s) of this article can be found under https://doi.org/10.1002/smll.201802825.
Dr. Y. Sun, Prof. F. Ding
Department of Physics and Astronomy
Clemson University
Clemson, SC 29634, USA
Dr. Y. Okazaki, J. Gao, Prof. R. Oda
Institut Européen de Chimie et Biologie
2 rue Robert Escarpit 33607, Pessac, France
E-mail: r.oda@cbmn.u-bordeaux.fr
Dr. P. Faridi, Prof. A. W. Purcell
Infection and Immunity Program & Department of Biochemistry and Molecular Biology
Biomedicine Discovery Institute
Monash University
Clayton, VIC 3800, Australia

DOI: 10.1002/smll.201802825

amyloid fragments of beta-lactoglobulin coated on multiwalled carbon nanotubes, sequestered toxic IAPP in vivo in an embryonic zebrafish model.[10] However, strategies aiming at in vivo mitigation of amyloidogenesis remain extremely limited.

Chiral structures are prevalent in nature, ranging from phospholipids in cell membranes to D-sugars, L-amino acids, and B-, A-, and Z-form deoxyribonucleic acids. These chiral structures are building blocks of biological systems and play essential roles in cell recognition and uptake, metabolism, protein synthesis, and genetic coding. Recently, chiral molecules such as the enantiomers of tartaric acid,[11] *N*-isobutyryl cysteine,[12] cysteine,[13] lysine, phenylalanine, and monometallic units have been used to functionalize mica, gold, carbon dots, and graphene oxide nanosheets, and the resulting surfaces have elicited differential effects on the aggregation of insulin and amyloid-β (Aβ) as well as on cell response.[14–16] While much remains to be understood, salt-bridge interaction, for example, has been proposed as a major mechanism for serum albumin interacting with gold nanoparticles coated with L- and D-penicillamine.[17] The implications of this type of research range from catalysis, sensing, and bioengineering to the inhibition of amyloid protein aggregation at pseudohomochiral interfaces, such as ligand-modified surfaces and cell membranes. However, the use of chirality of either the inhibitors or the amyloid fibrils against amyloidogenesis, especially chirality on the nanoscale, remains a rarity.

In this study, we synthesized both left- and right-handed silica nanoribbons (L/R-SiO_2), whose pitch sizes (≈90 nm) were on the same order of magnitude as that of IAPP amyloid fibrils (20–50 nm).[8,18] It is known from the literature that IAPP fibrils, as well as fibrils of Aβ and tau, generally adopt left-handedness, although right-handed IAPP fibrils have been observed occasionally.[8,18] This biased amyloid chirality is understood as a result of the dominance of left-handed amino acid species, the building blocks of amyloid peptides and proteins. On the other hand, silica nanostructures, including silica nanoribbons, have been widely applied in electronics, drug delivery, sensing, and catalysis.[19,20] The combination of inorganic nano-objects and chirality, either by grafting chiral molecules to silica nanoparticles or forming silica nanostructures of chiral shapes, along with the well-known surface chemistry of silica and their easy functionalization by other molecules or nanoparticles, enables chiral recognition or chiral separation,[21,22] meme of nanoperiodic patterns in biology,[23] chiroptical nanomaterials,[24,25] nanosensors,[26] or chiral catalysis.[27]

Here the mesoscopic chirality of silica nanoribbons is utilized for the first time to inhibit IAPP toxicity. The effects of the nanoribbons on IAPP aggregation were first evaluated using a thioflavin T (ThT) kinetic assay and transmission electron microscopy (TEM). The efficacies of the L/R-SiO_2 on IAPP toxicity inhibition were examined with βTC-6 pancreatic beta cells and a high-throughput in vivo embryonic zebrafish model. The R-SiO_2 were more potent than the L-SiO_2 in inhibiting IAPP aggregation and toxicity, due to fibrillization along the perpendicular direction and hence a higher density of seeding IAPP on the silica nanostructures, as corroborated by TEM and coarse-grained computer simulations. This study points to the potential of exploiting the mesoscopic enantioselectivity of amyloid proteins for the prevention and treatment of a range of human amyloid diseases.

2. Results and Discussion

2.1. Characterization of Chiral Silica Nanoribbons

The morphology and dimensions of the L/R-SiO_2 are summarized in **Figure 1**, which appeared highly comparable except for the handedness. Specifically, the average width and half pitch size were 19.5 ± 2 nm and 44.7 ± 3.9 nm for L-SiO_2 and 19.4 ± 1.9 nm and 44.3 ± 3.5 nm for R-SiO_2, respectively. The L/R-SiO_2 were negatively charged at −23 ± 0.4 mV and −22.2 ± 0.5 mV, which enabled their electrostatic interactions with the cationic IAPP peptide.[8]

2.2. IAPP Fibrillization Inhibition and Remodeling by Chiral Silica Nanoribbons

TEM imaging revealed associations of the L/R-SiO_2 with IAPP monomers, oligomers, and amyloid fibrils (**Figure 2**). Comparison of IAPP in the presence of the L/R-SiO_2 with control IAPP fibrils clearly indicates that the peptides were attracted to the nanoribbons, causing an increase in local IAPP concentration and hence a rapid transition from nucleation to elongation. This attraction markedly affected the formation of fibrils. In the case of the silica nanoribbons with preformed IAPP protofibrils/fibrils (48 h IAPP), the R-SiO_2 showed more interaction with the helical IAPP fibrils than the L-SiO_2 (Figure 2H–I).

Statistics analysis of the TEM images using FiberApp[45] offered additional insights into IAPP aggregation and fibril remodeling by the nanostructures. Both the L-SiO_2 and R-SiO_2 were effective in preventing the formation of full IAPP fibrils of micrometers in length[18] and, instead, yielded IAPP protofibrils and short fibrils of 100–150 nm in length. Regular IAPP fibrils, 13.6 ± 2.9 nm in width, were split into much thinner fibrils of 6.7 ± 1.8 nm in the presence of the R-SiO_2, indicating strong remodeling by the mismatched pitches (90 nm for R-SiO_2 vs 20–50 nm for IAPP fibrils[18]) and opposite handedness of the two interactants, while L-SiO_2 did not show notable remodeling of the established IAPP fibrils. The greater capacity of the R-SiO_2 in remodeling IAPP amyloid fibrils, in comparison with the L-SiO_2, can be attributed to their morphological mismatches than with the latter, and hence breakage of H-bonding and hydrophobic interactions within the IAPP fibrils to render protofibrils. More discussion on this aspect can be found in the following simulation section concerning fibril remodeling by the L/R-SiO_2.

In the absence of the chiral nanoribbons, the ThT kinetics displayed an initial lag phase due to IAPP nucleation, followed by a rapid aggregation of the peptide before reaching the saturation phase in ≈8 h (Figure 2J). This result is consistent with IAPP fibrillization kinetics reported in literature.[28,29] In the presence of the L/R-SiO_2, the ThT intensity significantly dropped compared to the IAPP control, indicating the lower β-sheet contents due to the inhibition of fibril formation. In addition, in the presence of the nanoribbons, the lag time of IAPP fibrillization was significantly shortened. This phenomenon is related to charge attraction between the N-terminus of the peptide and the anionic silica nanoribbons, in addition to hydrogen bonding and hydrophobic interaction between

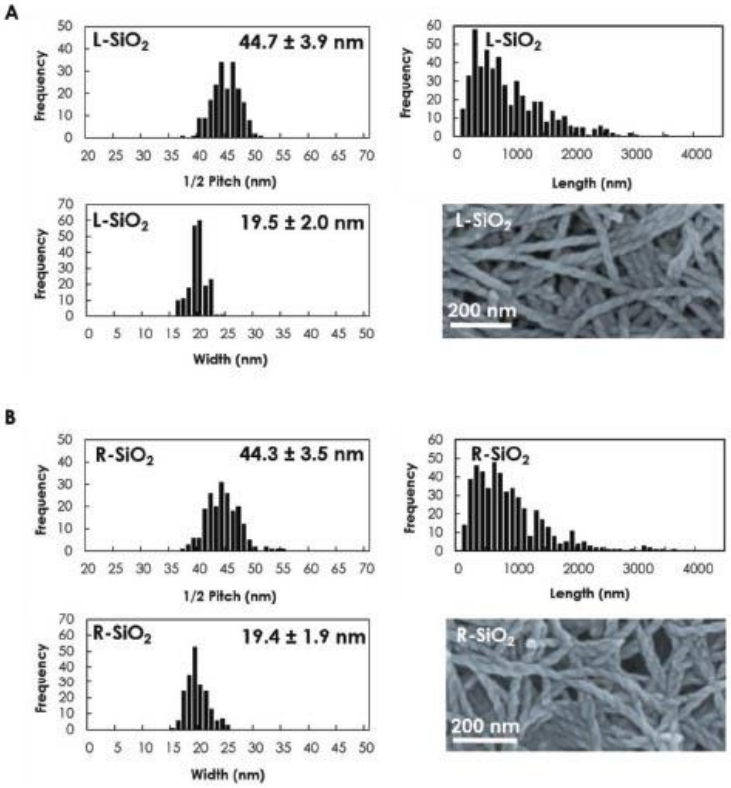

Figure 1. Characterizations of the silica nanoribbons show half pitch size, length, and width of the A) L-SiO_2 and B) R-SiO_2. Images acquired with scanning electron microscopy.

the two species, which elevated local peptide concentration to accelerate their nucleation through seeding[48,29] on the silica surfaces, similarly to the catalytic role of lipid membranes for amyloid protein aggregation.[2,8] Such interactions converted IAPP from disordered monomers to α-helix and then β-sheet rich oligomers and protofibrils and, eventually, cross-beta amyloid fibrils of compromised lengths (Figure S6, Supporting Information). TEM imaging corroborated the observation, revealing less densely populated IAPP fibrils. The rigidity of the IAPP protofibrils and fibrils in the presence of the nanoribbons was difficult to determine by statistical analysis, however, due to the much shorter lengths of the peptide structures (compared to the micrometer lengths of full IAPP fibrils). Interestingly, IAPP fibrillization in the presence of the L-SiO_2 exhibited higher ThT intensities than with the R-SiO_2. In the saturation phase, specifically, the ThT fluorescence intensity was ≈36% lower with the R-SiO_2 than with the L-SiO_2, indicating a higher efficiency of IAPP aggregation inhibition with the oppositely handed silica nanoribbons. A plausible reason for such discrepancy is provided in later sections.

2.3. Coarse-Grained Simulation of Fibrillization and Fibril Remodeling by L/R-SiO_2 Nanoribbons

To understand the different effects of the L/R-SiO_2 on IAPP oligomerization and fibrillization at the molecular level, we developed a coarse-grained 11-bead peptide model capable of capturing general features of amyloid aggregation, including peptide conformational changes upon aggregation, the mesoscopic morphology of amyloid fibrils, and aggregation kinetics, which cannot be fully captured by existing coarse-grained models (details of the peptide model, discrete molecular dynamics (DMD) simulation, and data analysis in the Experimental Section). DMD simulations with 100 coarse-grained model peptides were performed for peptides alone and in the presence of either an L- or R-SiO_2. A peptide in our model can adopt either the aggregation-incompetent π-state representing random coil or helical conformations (Figure S3B, Supporting Information), or the aggregation-prone β-state representing β-sheets (Figure S3C, Supporting Information). We assigned the π-state with a lower free energy than the β-state

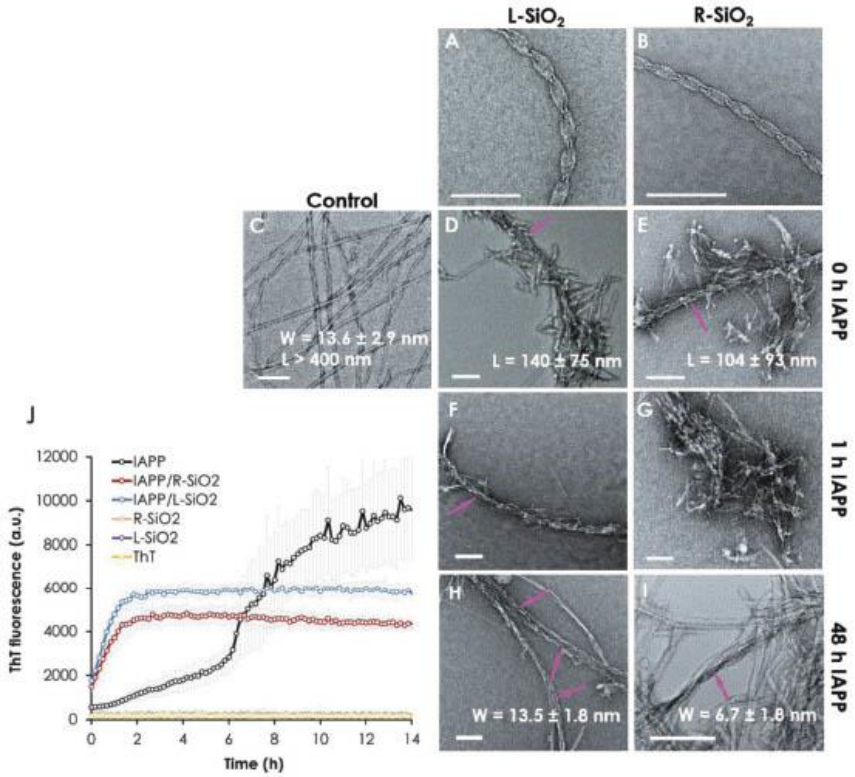

Figure 2. Transmission electron microscopy images of A,B) the L/R-SiO_2 and C) IAPP control. D–G) Attractions between the peptide and the nanoribbons caused shortening and inhibition of the fibrils compared with the control. H,I) The R-SiO_2 was effective in remodeling the IAPP fibrils. All samples were incubated for 24 h. J) ThT kinetic assay of IAPP fibrillization over 14 h show a shortened lag phase and inhibition of fibrillization in the presence of the L/R-SiO_2. Arrows in panels (D)–(F), (H), and (I) indicate discernible L/R-SiO_2 in contact with IAPP protofibrils/fibrils. Scale bars: 100 nm. The experiments were carried out in triplicate and error bars show the standard deviations of the averaged data sets. IAPP concentration: 50×10^{-6} M for the ThT assay and 20×10^{-6} M for TEM, at room temperature and pH 7.

(Figure S3D, Supporting Information). Isolated peptides before aggregation in our simulations mainly adopted the aggregation-incompetent π-state (Figure S4, Supporting Information). The time evolution of the total number of hydrogen bonds (**Figure 3**A) and the number of peptides in β-sheet conformations (Figure 3B) indicated the nanoribbons accelerated peptide aggregation by significantly reducing the initial lag phase of the peptide alone (0–0.3 μs). The peptide in the presence of L-SiO_2 reached its saturation state faster than those with R-SiO_2. Hence, the aggregation kinetics results from the simulations were consistent with the ThT assay (Figure 2J). The time evolution of the average size of fibril aggregates was computed, by estimating the β-state aggregates weighted by their aggregate sizes (i.e., the number of peptide in an aggregate). Peptides in the presence of the R-SiO_2 tended to form smaller aggregates compared to both the control and the L-SiO_2 (Figure 3C). The final aggregates of peptide alone or in the presence of the L-SiO_2 could reach the size of ≈80, corresponding to the majority of the simulated peptides, while remained at ≈40 in the presence of the R-SiO_2. Since the final aggregates were about the same for different systems (Figure 3B), these results suggest that the R-SiO_2 promoted the formation of multiple smaller aggregates than the control or the L-SiO_2.

Snapshots taken along the simulation trajectories (Figure 3D; Video S1, Supporting Information) indicated that peptides in solution first formed smaller aggregates, which then merged into larger fibrillar oligomers either along the elongation direction or on the nanostructure surface, forming left-twisted multilayer aggregates. In the presence of the L-SiO_2 (Figure 3E; Video S2, Supporting Information), peptides first bound to the nanostructure surface in the forms of both fibrillar and non-fibrillar oligomers, which further rearranged and merged into a single fibrillar aggregate on the nanostructure surface and along its axis due to their matching left-handed morphologies.

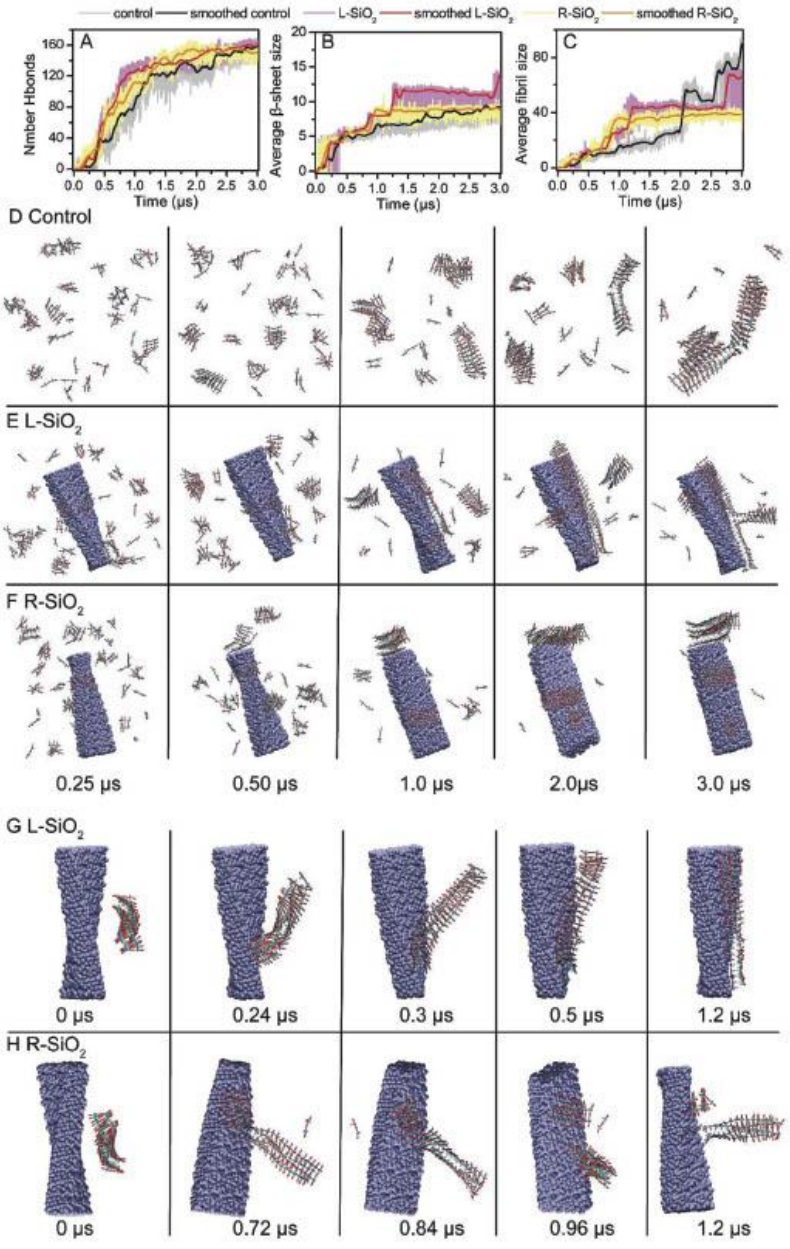

Figure 3. Coarse-grained modelling of fibrillization and fibril remodeling in the presence of chiral silica nanoribbons. A–C) Time evolution of total number of hydrogen bonds, average β-sheet sizes, and average fibrillar aggregate sizes. D–F) Fibrillization in the absence and presence of the L/R-SiO_2 during 3 μs of simulation. G,H) Remodeling of preformed fibril in the presence of the L/R-SiO_2.

Interestingly, the fibrils could form branches upon binding and conformational rearrangement (e.g., 2.4–3 μs in Figure 3E). Due to the morphological mismatch between fibrils and the R-SiO_2, small aggregates formed on the nanoparticles surface preferred to align perpendicularly to the nanostructure axis and did not self-assemble into larger aggregates as in the control or with the L-SiO_2 (Figure 3F; Video S3, Supporting Information). These small aggregates on the nanoparticle surfaces could function independently as seeds for further elongation. With the same total number of peptides but more independently formed fibrils, the average size/length of fibrils in the presence of the R-SiO_2 were smaller than with L-SiO_2, consistent with the contour length analysis of the IAPP fibrils (Figure 2). Comparison of fibrils originated from nanostructure surfaces in TEM imaging also suggests that fibrils near the R-SiO_2 surface tended to be perpendicular to the nanostructure axes (Figure 2E,G) while fibrils near the L-SiO_2 surface were more aligned along the nanostructure axes (Figure 2D,F), as predicted by the coarse-grained DMD simulations (Figure 3).

In addition, we performed simulations of a preformed fibril interacting with the L/R-SiO_2 in order to understand their differential capacities of remodeling fibrils (Figure 3G,H). A preformed fibril was initially positioned away from the nanoribbons with randomly generated orientation. The preformed fibril could first adsorb onto the surfaces of both the L- and R-SiO_2. Due to the morphological match between the fibril and the L-SiO_2, the left-handed fibril could rearrange itself and align with the nanoribbon to increase the fibril–nanoparticle contacts (Figure 3G). On the other hand, the fibril on the surface of the R-SiO_2 could not fully align with the nanoparticle due to the mismatch of morphologies, and instead broke into shorter fibrils bound to the nanoparticle surface perpendicularly (Figure 3H). The latter phenomenon took place because the energy gain of surface contact between shorter fibrils and the R-SiO_2 was more favorable than the energetic cost of breaking the fibril (e.g., local interactions between stacked peptides in the fibril). In cases of excessive fibrils with respect to silica nanoribbons, as in the experiments, the L-SiO_2 surfaces were fully covered by fibrils aligned along the nanoribbon axes due to matching morphologies. Fibrils, on the other hand, tended to bind the R-SiO_2 without alignments, as shown in simulations (Figure 3). Hence, the R-SiO_2 had more available surface areas for interacting with fibrils than the L-SiO_2. Fibrils in solution undergo constant dynamics,[18] including the bundling/unbundling equilibrium between thin protofibrils and thick fibrils. Compared to the L-SiO_2, more available surface areas on the R-SiO2 for fibril binding shifted the bundling/unbundling equilibrium toward thin protofibrils. Hence, the coarse-grained simulations offered molecular insights to the differential capabilities of the L- and R-SiO_2 in remodeling amyloid fibrils, as observed in TEM imaging (Figure 2H,J).

2.4. In Vitro IAPP Toxicity with Silica Nanoribbons

The toxicity of IAPP is a main cause for the degeneration of pancreatic beta cell islets[30,31] and, as with amyloid proteins such as Aβ and alpha synuclein, the oligomeric forms of IAPP are believed to be the most toxic species.[1] Therefore, a viability assay was performed using pancreatic βTC-6 cells exposed to the L/R-SiO_2 in interaction with various IAPP structures. The results of 14 h cell treatment are shown in **Figure 4**A for IAPP monomers, oligomers, and amyloid fibrils. In the case of IAPP monomers, silica nanoribbons were potent in alleviating

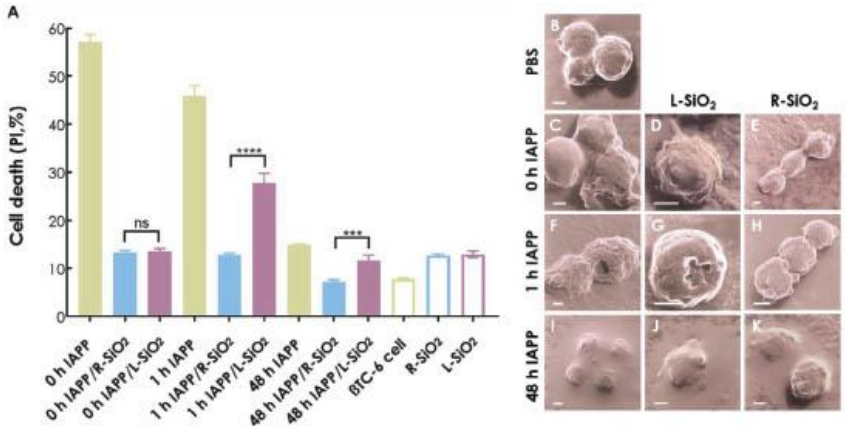

Figure 4. A) Determination of in vitro toxicities of 0, 1, and 48 h aged IAPP on βTC-6 cells in the presence and absence of L/R-SiO_2 (ns: $P > 0.05$, ***: $P \leq 0.001$ and ****: $P \leq 0.0001$). Visualization of B) βTC-6 cell damage induced by C) 0 h IAPP, F) 1 h IAPP, and I) 48 h IAPP and their mitigation by the L/R-SiO_2 with helium ion microscopy (D, E; G, H; J, K). Scale bars: 2 μm. Here the 0, 1, and 48 h aged IAPP refer to IAPP freshly dissolved in water (0 h IAPP), oligomers/protofibrils (1 h into fibrillization), and fibrils (48 h into fibrillization), respectively. The incubation time of the IAPP species in the cell toxicity assay was 14 h. The experiments was carried out in triplicate and error bars show the standard deviations of the averaged data sets. IAPP concentration: 20×10^{-6} M, at room temperature and pH 7.

IAPP toxicity, by ≈75% for both the L/R-SiO_2. As monomeric IAPP possessed no handedness, the effect of nanostructure chirality was understandably negligible. With IAPP protofibrils, in contrast, their interactions with chiral nanoparticles appeared handedness dependent. Specifically, the R-SiO_2 were over twice more effective than the L-SiO_2 in reducing IAPP cytotoxicity, indicating a stronger binding affinity between the R-SiO_2 and toxic IAPP species. In the case of IAPP amyloid fibrils, the R-SiO_2 were 1.7 times more efficient than the L-SiO_2 in suppressing IAPP toxicity, suggesting cooperative binding between the R-SiO_2 and the oppositely handed IAPP fibrils over length scales of tens to hundreds of nanometers (Figure 2I,H). Consistently, a colorimetric 3-(4,5-dimethylthiazol-2-yl)-2,5-diphenyltetrazolium bromide assay revealed that preformed IAPP fibrils were less toxic than monomeric and oligomeric IAPP. In the presence of the silica nanostructures, the R-SiO_2 was effective in decreasing the toxicity of oligomeric and preformed IAPP, while both the L/R-SiO_2 were effective in reducing the toxicity of monomeric IAPP (Figure S7, Supporting Information).

As expected, helium ion microscopy revealed significant damage (including pore formation) and deformation of βTC-6 cell membranes exposed to IAPP monomers and oligomers (Figure 4C,F). No remarkable cell damage was found in exposure to IAPP amyloid fibrils, and coating of cell surfaces by the protein was notable due to attraction between the anionic lipid membranes and cationic IAPP. The damage was un-noticeable when the cells were exposed to IAPP in the presence of the L/R-SiO_2, especially for the R-SiO_2 (Figure 4I–K). Some cells displayed rugged morphologies in exposure to IAPP oligomers/amyloid fibrils together with the L-SiO_2 (Figure 4D,G). However, no cell deformation was observed in exposure to IAPP oligomers/fibrils together with the R-SiO_2 (Figure 4E–K), which is consistent with the viability results (Figure 4A).

2.5. In Vivo IAPP Toxicity with Silica Nanoribbons

The use of zebrafish embryos as an in vivo model has led to remarkable progress in toxicology and genetic studies,[32] and has recently been applied to the study of amyloidogenesis taking advantage of its high fecundity, well characterized developmental stages, transparency of embryos, and multicellular and multiorgan compositions.[10,33,34] Here an in vivo toxicity assay was performed by microinjecting the L/R-SiO_2 and the three IAPP species into the yolk of 2 hpf zebrafish embryos. The results on the survival and phenotypic abnormalities are shown in **Figure 5**A–C. In the case of the 0 h IAPP, silica nanoribbons increased the survival of the embryos, from 25 ± 6% for the control to 43.7 ± 5.2% and 51.2 ± 5.5% in the presence of the L/R-SiO_2, respectively. In the case of the 1 h IAPP, where unstructured monomers were converting into oligomers and protofibrils,[8] the survival rate increased from 19 ± 6% for the control to 40 ± 9% and 66 ± 9% in the presence of the L-SiO_2 and R-SiO_2, respectively. In the case of the 48 h IAPP fibrils, the R-SiO_2 were 100 ± 8.5% more efficient in suppressing IAPP cytotoxicity than the control, while the L-SiO_2 decreased the survival of the embryos induced by IAPP fibrils by 40% in comparison with the control. Consistent with the survival results, the R-SiO_2 in interaction with all IAPP structures showed lower abnormalities compared to the control and with the L-SiO_2.

Figure 6 compares nontreated embryos with the treated embryos based on the green fluorescence of ThT from 4 hpf until 4 dpf (A)–(E). The strongest signal (corresponding to the highest IAPP aggregation) occurred in the absence of the silica helices, which was concomitant with the appearance of phenotypic abnormalities (panel (B)). Consistent with the ThT assay, the IAPP fluorescence intensity was decreased upon interaction with the L-SiO_2, and in the presence of the R-SiO_2 the ThT intensity remained comparable to that of the control. In general, the strongest ThT intensity was observed at 4 dpf indicating saturation of IAPP fibrillization.

Many studies have shown the physiological mechanisms of zebrafish larvae behaviors in terms of their vision, swimming activity, and responses to touching resulting from early toxicant exposure.[35–37] In this study, the effects of IAPP in the presence and absence of the L/R-SiO_2 on the swimming behavior of larvae, in the observable forms of swimming distance and rotation, were recorded (Figure 6F). The 96 hpf larvae were able to freely swim in linear paths and change their swimming directions spontaneously. The zebrafish larvae (4 dpf) treated with 0 h IAPP and 0 h IAPP/L-SiO_2 showed more rotational movement (<180°, Video S4, Supporting Information) compared with the control (Video S5, Supporting Information) and with the R-SiO_2. One plausible cause for the elevated rotational movement is IAPP-induced stress. The larvae displaying more pronounced rotations were visually deformed due to the impact of the peptide toxicity on their development. Such behavioral abnormality may be closely related to the phenotype but not necessary damage to the neurons. Interestingly, the larvae injected with 48 h IAPP/L-SiO_2 exhibited the lowest activities both in rotation and swimming distance (Video S6, Supporting Information), indicating the highest toxicity upon interactions between peptide fibrils and nanoribbons of the same handedness (refer to Figure 4A). However, the larvae treated with 48 h IAPP and the R-SiO_2 showed significant improvements on activities, signifying their recovery from the amyloid toxicity.

3. Conclusion

The mesoscopic-scale chirality of silica nanoribbons strongly influenced IAPP fibrillization and toxicity in vitro and in vivo, especially in the case of the R-SiO_2. The nanoribbons attracted IAPP monomers through H-bonding and electrostatic and hydrophobic interactions and acted as nucleation sites for the conversion of IAPP monomers to oligomers and protofibrils, thereby reducing the concentrations of these species in solution to mitigate IAPP toxicity. Due to steric constraints, the R-SiO_2 nanoribbons allowed their surface-associated IAPP to elongate into left-handed amyloid fibrils in the directions away from or perpendicular to the silica backbone, while IAPP fibrils formed along the L-SiO_2 surfaces, as evidenced by TEM and DMD simulations. As a result of such directional IAPP aggregation on the nanoribbon surfaces, the R-SiO_2 possessed more binding and nucleation sites per surface area than the L-SiO_2 in sequestering toxic IAPP species from the solution (**Figure 7**). In addition, the R-SiO_2 was significantly more

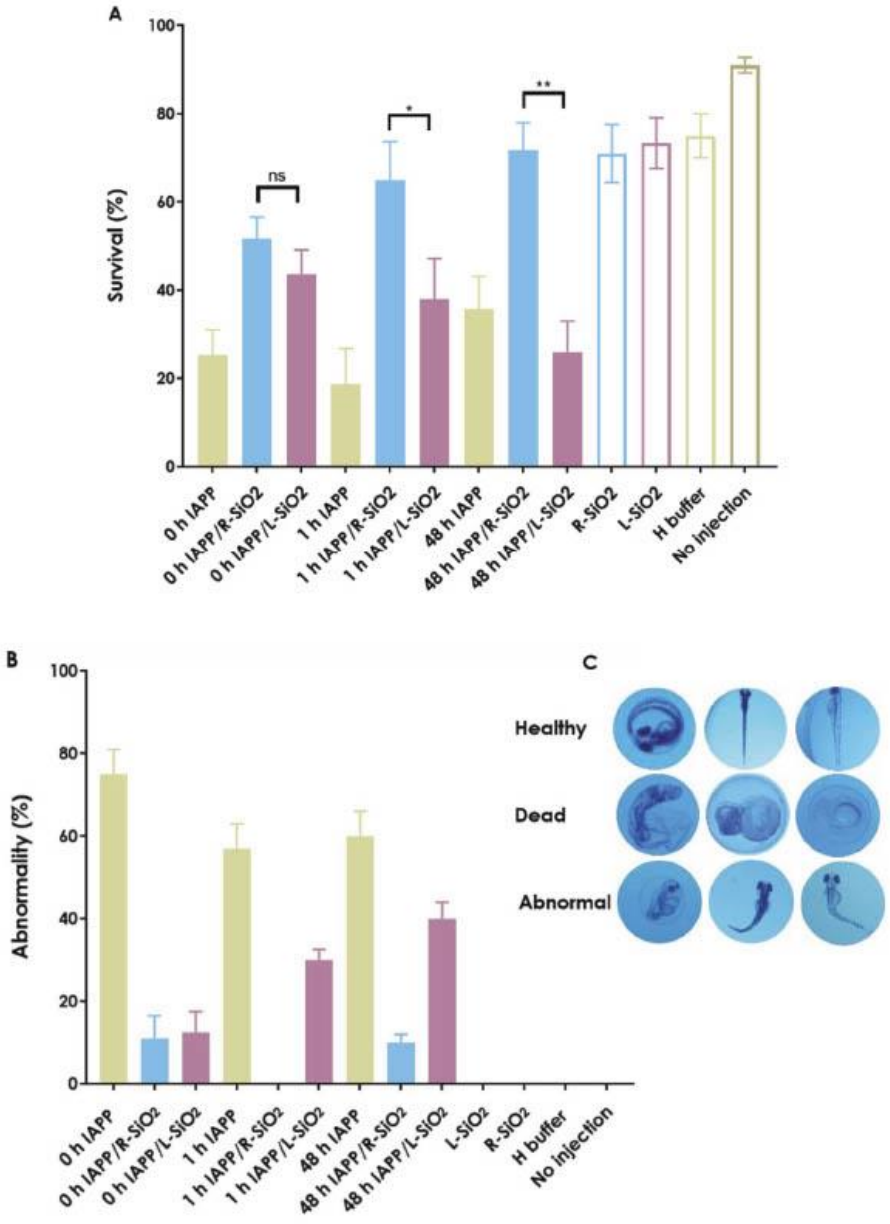

Figure 5. Determination of in vivo toxicity assay A) survival, B) abnormality on 2 hpf zebrafish embryos 80 h after treatments (related to fully hatched, untreated embryos) by microinjection of 1 nL of 10×10^{-6} M IAPP of 0, 1, and 48 h in the presence and absence of the L/R-SiO_2 (40 µg mL^{-1}) to the yolk of 2 hpf zebrafish embryos. C) Representative images of healthy, dead, and abnormal embryos. The experiments were carried out in triplicate and error bars show the standard deviations of the averaged data sets (ns: $P > 0.05$, *: $P \leq 0.05$ and **: $P \leq 0.01$).

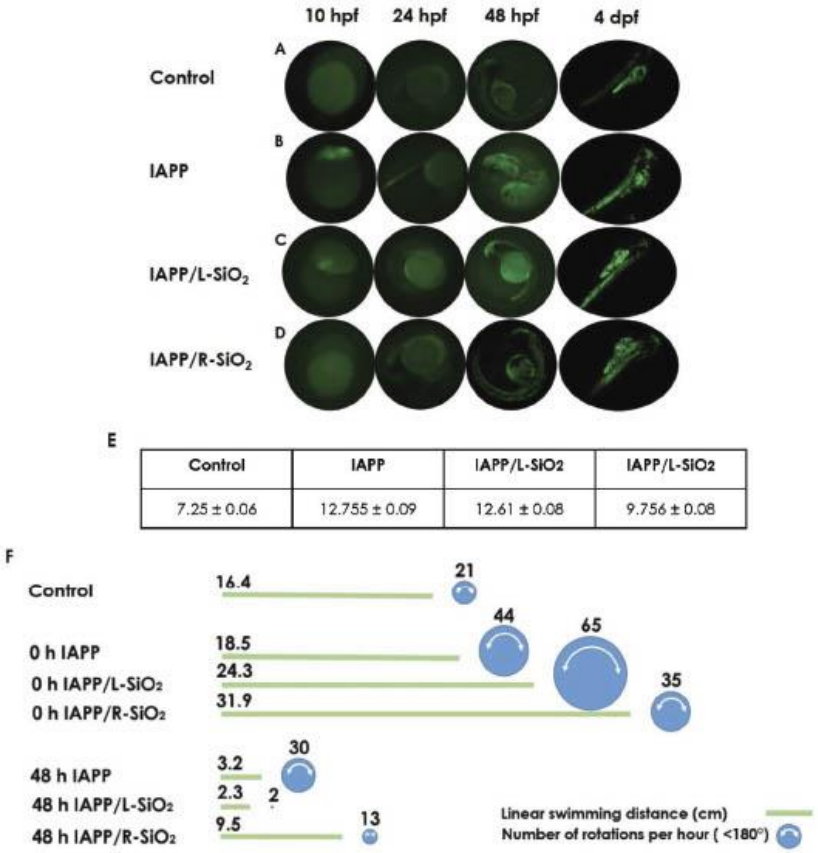

Figure 6. Fluorescence imaging of A) untreated and B–D) treated embryos during 4 days after treatment (saturation phase of IAPP fibrillization in embryos). IAPP (10×10^{-6} M) dissolved in ThT dye (20×10^{-6} M) preincubated w/o L/R-SiO_2 (40 μg mL^{-1}) was microinjected to the yolks of 2 hpf embryos. The intensities of ThT fluorescence were indicative of IAPP fibrillization in embryonic development from 10 hpf to 4 dpf. E) The mean intensities (a.u.) of ThT fluorescence were measured for IAPP preincubated w/o L/R-SiO_2. F) Linear swimming distance and number of rotations per hour for untreated and treated embryos 4 days after microinjection. The area of circle is proportional to the frequency of rotation per hour.

effective than their left-handed counterpart in remodeling mature IAPP fibrils, through complementary handedness of the interactants, mismatch of their pitch sizes, and directional aggregation of the peptide on the nanostructures. On-pathway protein aggregation, from disordered monomers to toxic oligomers and protofibrils and eventually to mostly left-handed β-sheet rich fibrils, may be steered off-pathway by interference from chiral molecules,[11–15,17,38] as shown in the literature, or from chiral nanostructures, as first demonstrated by this study through biophysical, toxicological, and behavioral characterizations. In light of the nonspecific nature of nanoparticle–amyloid protein binding, it is conceivable that the current findings may be applicable to other classes of chiral nanostructures (e.g., plasmonic chiral gold nanoparticles[39–41]) and other types of amyloid proteins (e.g., Aβ associated with Alzheimer's disease and alpha synuclein associated with Parkinson's disease). Hence, exploiting mesoscopic-scale chirality may prove an exciting new avenue for the synthesis and development of potent nanostructures against the aggregation and toxicity of a range of amyloid diseases.

4. Experimental Section

Chiral silica nanoribbons were fabricated as previously described.[42,43] Briefly, the self-assembly of dicationic surfactant, 1,2-ethane-bis(dimethyldecylammonium) with chiral counterions, L or D tartrate forming nanometric helices (right-handed or left-handed, respectively), were used as templates to form silica nanoribbons through sol–gel polycondensation with controlled dimensions and handedness. The silica nanoribbons were cut and individualized by sonication

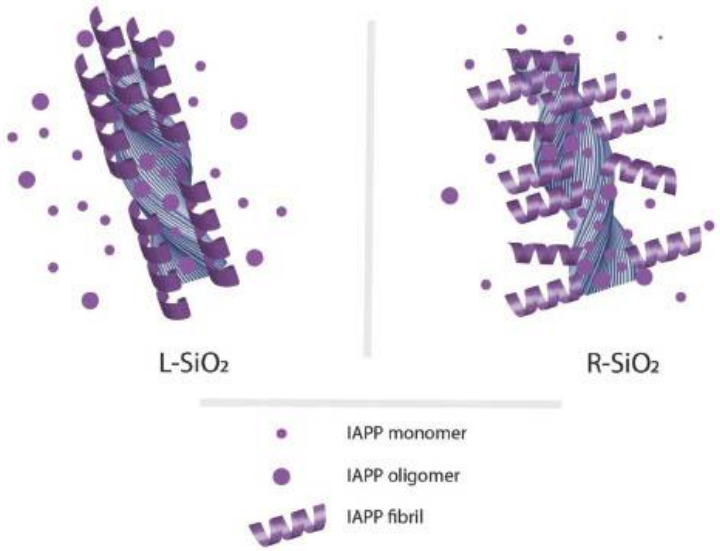

Figure 7. Adsorption of IAPP monomers and oligomers accelerated their nucleation and aggregation on silica nanoribbon surfaces. Such interactions decreased the net concentrations of free IAPP monomers and oligomers in solution to mitigate their associated toxicity. Due to the steric constraints imposed by the chiral silica nanoribbons, left-handed IAPP amyloid fibrils rendered by surface-adsorbed monomers and oligomers elongated away from or perpendicular to the R-SiO_2 backbone. By contrast, left-handed IAPP fibrils extended nearly parallel to the L-SiO_2 surfaces, thereby shielding the nanostructures from being further accessed by the peptide. Accordingly, the R-SiO_2 possessed much more binding sites per surface area than the L-SiO2 for IAPP adsorption and aggregation, as also evidenced by TEM and DMD simulations, and hence were far more effective in preventing IAPP induced toxicity.

(Vibra-cell 75 186, Sonics & Materials) to be colloidal suspensions.[44] Lyophilized white powder of human islet amyloid polypeptide (IAPP; KCNTATCATQRLANFLVHSSNNFGAILSSTNVGSNTY; 2–7 disulfide bridge, 3904.5 Da, purity >95%; AnaSpec; high-performance liquid chromatography (HPLC) and mass spectroscopy characterizations of IAPP refer to Figures S1 and S2, Supporting Information) was freshly dissolved in Milli-Q water at room temperature. ThT dye (319 Da) was acquired from Sigma-Aldrich. Propidium iodide (PI, excitation/emission: 535 nm/617 nm) was purchased from ThermoFisher. Poly L-lysin (0.01%) was acquired from Sigma-Aldrich and applied for cell staining.

Zeta Potential Measurement: The zeta potentials of the L/R-SiO_2 in Milli-Q water were determined using a Zetasizer Nano-ZS (Malvern Instruments, UK). The measurement was conducted using disposable folder capillary cells and analyzed by Zetasizer Software 7.02.

Scanning Electron Microscopy (SEM): For morphology imaging, 5 µL of L/R-SiO_2 (0.2 mg mL^{-1}) was pipetted and air dried on a carbon tape and the nanostructure surfaces were coated with a thin layer of sputtered gold (Bal-Tec SCD 005 Sputter) and visualized by a scanning electron microscope (FEI, Nova NanoSEM 450).

ThT Kinetic Assay: A kinetic assay was performed with 50×10^{-6} M ThT dye and 50×10^{-6} M IAPP in the presence and absence of the L/R-SiO_2 (0.2 mg mL^{-1}, for 1:1 IAPP/nanostructure mass ratio) in a 96-well plate (Costar black/clear bottom). Changes in ThT fluorescence, indicating the β-sheet content in the IAPP sample, were recorded at room temperature from the plate bottom side every 10 min over 14 h to reach the full saturation phase, using a PerkinElmer EnSight HH33400 plate reader (excitation/emission: 440 nm/485 nm). The data were stored by software Kaleido 1.2. The assay was performed in triplicate and average spectra of the measurements were presented.

TEM: For this measurement, 5 µL of the L/R-SiO_2 (0.2 mg mL^{-1}) was allowed to interact with IAPP monomers (5 µL of 50×10^{-6} M; freshly dissolved in water, termed as "0 h IAPP" from here onward), oligomers/protofibrils (1 h into fibrillization, termed as "1 h IAPP"), and fibrils (48 h into fibrillization, termed as "48 h IAPP") for 24 h of incubation. The samples were then pipetted onto 15 s glow-discharged 400 mesh copper grids (Formvar film, ProSciTech) for 60 s of adsorption. Excess samples were drawn off by filter paper and the grids were washed using 10 µL of Milli-Q water, with excess drawn off. The grids were then negatively stained with 5 µL of 1% uranyl acetate for 30 s with excess stain drawn off and air-dried. Samples were characterized on a Tecnai G2 F20 transmission electron microscope (FEI, Eindhoven, The Netherlands) operated at a voltage of 200 kV. Images were recorded using an UltraScan 1000 P 2k CCD camera (Gatan, California, USA) and Gatan Digital Micrograph 3.9.5 software.

Statistical Analysis of Amyloid Fibrils: To investigate the effects of the L/R-SiO_2 on the morphology of IAPP fibrils, TEM images were analyzed with open source software FiberApp.[45] The values of IAPP fibril length and thickness were estimated for 30 samples per condition.

Coarse-Grained Simulations: A coarse-grained amyloid peptide model was developed in DMD simulations to study the formation of amyloid fibrils. DMD is a particular type of molecular dynamics algorithm, where the interatom interaction potentials are modeled by step functions.[46] Briefly, in DMD simulations any atom moves with a constant velocity until an interatomic interaction potential step is encountered, i.e., a collision event. New velocities of two colliding atoms are determined by conservation laws of energy, linear and angular momenta. DMD simulations have been widely used to study protein amyloid aggregation.[47–51] Here, each coarse-grained peptide was represented by 11 beads (Figure S3A, Supporting Information). Two donors (atoms N1 & N5) and two acceptors (atoms O3 & O7) were able to form interchain peptide hydrogen bonds. The angular and distance-dependent hydrogen bond formed between C—N and C—O, where C denoted the

carbon atom (atoms C2 or C6) covalently linked to either donor or acceptor with a bond length of 1.5 Å, was modeled by a reaction-like algorithm.[52] A hydrogen bond with the lowest potential energy had a linear alignment between C—N and C—O and a donor–acceptor distance of ≈2 Å. Two hydrophobic beads—atoms C4 and C8 attached to C2 and C6 with a bond length of 3 Å, respectively—were introduced to model side-chain interactions between different peptides. Each peptide also included three hydrophilic beads, atoms O8, O9, and O9, which were collinear with C2 and C6 with an average separation of 5 Å forming the coarse-grained peptide "backbone." Both N1–C2–O3 and N5–C6–O7 in a peptide were collinear and perpendicular to the backbone. C2–C4 (or C6–C8) was perpendicular to both the backbone and N1–C2–O3 (or N5–C6–O7). The conformation of a peptide was, thus, determined by the dihedral angle between C4–C2–C6–C8, modeled by a multiple-well step function.[53] Motivated by a previous coarse-gained peptide model,[54–56] we allowed the peptide to adopt two conformations: amyloid-competent (β) and amyloid-protected (π) states (Figure S3B–D, Supporting Information). In the β-state, the dihedral angle with minimum free energy was ≈15°, and thus, both donors and acceptors (N1–C2–O3 and N5–C6–O7) in the peptide were approximately parallel to each other, compatible with a long fibrillar state. On the other hand, the π-state had the dihedral angle ≈90° and was incompatible with the linear fibril. In this study, the π-state of an isolated peptide was more favorable than the β-state with a lower free energy of ≈1.0 k_BT, where k_B denotes the Boltzmann constant and T corresponds to the simulation temperature. We adopted an HP-like interaction potential model[57] for nonbonded interactions—an attractive potential, ≈2 k_BT, was assigned among hydrophobic C4 and C6 atoms, and a hard-core only interaction potential was assigned among hydrophilic atoms (O9, O10, O11) and between hydrophobic and hydrophilic atoms. The net energy gain for a hydrogen bond was ≈5.5 k_BT.

To model the chiral silica, a ≈2.1 × 4.3 × 13 nm^3 crystal structure was first built along the x, y, and z dimensions using a unit cell structure of SiO_2 from the Materials Studio Software. We then followed the central axis in the x–y dimensions along the z-axis and rotated all atoms' coordinates with angles proportional to their z-values, ≈$\pm 2\pi z/L$, for the L/R-SiO_2, respectively (Figure S3E,F, Supporting Information). Here, L is the pitch length of ≈90 nm. In the simulations, the chiral silica structures were kept static while the coarse-grained peptides were allowed to freely move. Since silica was polar and the oxide on the surface was able to form hydrogen bonds with the peptides, this effect was modeled by assigning a weak attraction between all heavy atoms in silica (Si and O atoms) and the polar beads in the coarse-grained peptides (excluding hydrophobic C4 and C8), ≈0.075 k_BT.

We studied three sets of molecular systems, including the control of peptide self-assembly, and in the presence of either the L-SiO_2 or R-SiO_2. 100 peptides w/o silica nanoribbons were randomly positioned in a 20 × 20 × 20 nm^3 cubic box with intermolecular distance being kept at least 1 nm. The peptide concentration was ≈20.8 × 10^{-3} M in all cases, with the excluded volume of nanoparticles negligible. A periodic boundary condition was used. Each DMD simulation of peptide aggregation lasted 3 µs. To avoid potential bias of the initial states, the starting conformation of each peptide was randomly assigned. During the early aggregation stage, the distribution of peptides in either the π- or β-state (≈80% in π-state and ≈20% in β-state) was consistent with the corresponding free energy difference of isolated peptides (Figure S4, Supporting Information); the initially nonaggregated peptides predominantly adopted the π-state, also consistent with the experimental starting condition. Indeed, the coarse-grained peptides spontaneously formed left-handed fibrils (Figure S5, Supporting Information).

For the analysis of the coarse-grained aggregation simulations, the number of hydrogen bonds, the number of peptides in β-sheet conformations, and the size of β-sheet aggregates were monitored. A peptide belonged to a β-sheet only if it was in the β-conformation and was stabilized by at least two interpeptide hydrogen bonds. The aggregates of multiple β-sheets were defined by interpeptide contacts with an interatomic distance cutoff of 0.75 nm.

Cell Culture and Viability Assay: Pancreatic βTC-6 beta cells were cultured in complete Dulbecco's modified Eagle's medium (DMEM) with 15% fetal bovine serum (FBS). For the viability assay, a 96 well plate (Costar black/clear bottom) was coated with 70 µL Poly-L-lysine (Sigma, 0.01%), incubated at 37 °C for 30 min and cells at a density of ≈50000 cells per well in 200 µL DMEM with 15% FBS were added to the wells. Cells were incubated for 48 h at 37 °C and 5% CO_2 to reach 70–80% confluency. The cell culture medium was then refreshed, and 1 × 10^{-6} M PI dye in DMEM was added to the wells and incubated for 30 min. After optimization of concentrations, samples of 20 × 10^{-6} M IAPP and 0.08 mg mL^{-1} L/R-SiO_2 (at a 1:1 mass ratio) were added into the wells. All samples were examined in triplicate and measured by Operetta (PerkinElmer, 20 × PlanApo microscope objective, numerical aperture NA = 0.7) in a live cell chamber (37 °C, 5% CO_2) after 14 h of treatment. The percentage of dead cells (PI-positive) relative to total cell count was determined by a built-in bright-field mapping function of Harmony High-Content Imaging and Analysis software (PerkinElmer). The measurement was conducted at 5 reads per well and performed in triplicate. Untreated cells were recorded as controls.

Helium Ion Microscopy (HIM): βTC-6 cells were incubated with 20 × 10^{-6} M IAPP monomers, oligomers, and amyloid fibrils in the presence and absence of the L/R-SiO_2 for 30 min, and were then stabilized by 2.5% paraformaldehyde. The samples were incubated at 4 °C overnight. In the next step, samples were gently centrifuged and paraformaldehyde/medium was replaced with gradient concentrations of ethanol in 5 steps: 20%, 40%, 60%, 80%, and 95%, with 2 h incubation at each gradient. 30 µL of treated βTC-6 cells was air-dried on a carbon tape and the morphologies of treated cells and untreated cells, as controls, were visualized by HIM (Orion NanoFab, Zeiss, USA).

Zebrafish Embryo Toxicity Assay: IAPP of 1 nL dissolved in Milli-Q water for 0, 1, and 48 h as controls and mixed with the L/R-SiO_2 (10 × 10^{-6} M IAPP and 40 µg mL^{-1} L/R-SiO_2 in final concentration) were microinjected to the yolk of zebrafish embryos at the age of 2 h postfertilization (hpf). Injection was conducted using a pneumatic picopump (PV830 Pneumatic Picopump, WPI) and capillary needles. After injection each embryo was placed in 96-well plate, one embryo per well containing 200 µL Holtfreter's medium (H buffer).[58] To investigate the toxic effect of IAPP fibrillization w/o L/R-SiO_2, the development, hatching, and abnormality of the embryos were recorded (Olympus SZ61) every 24 h up to 80 hpf. The experiments were performed in triplicate, for 12 samples of each treatment condition.

Fluorescence Imaging of Embryonic IAPP Fibrillization: Similarly to the toxicity assay, the L/R-SiO_2 were brought to interact with IAPP dissolved in 20 × 10^{-6} M ThT solution for 10 min and were then microinjected to the yolk of zebrafish embryos. The intensity related to IAPP fibrillization in the green fluorescence channel, due to the binding of the ThT dye to β-sheet rich protofibrils and fibrils, was tracked in treated embryos up to 4 days postfertilization (dpf) (Olympus MVX10, OCULAR software version 2.0). The experiments were performed in triplicate for 12 samples of each treatment condition.

Behavioral Experiment: Monomeric and fibrillar IAPP of 10 × 10^{-6} M mixed for 10 min with 40 µg mL^{-1} of L/R-SiO_2 (1 nL in total volume) were microinjected to the yolk of 2 hpf zebrafish embryos and behavioral parameters were recorded on the surviving larvae 4 days after treatment. Each larva was put in one well of a 96 well plate and their real-time behavior was recorded using an automated behavior analysis system, ZebraBox (Viewpoint, France). The initial head-to-tail positions were set as the reference angles of 0° for each larva. Linear swimming distance (cm) and number of rotations per hour (<180° clock-wise or anti-clockwise; rotations beyond one full circle or >180° were rare events and were excluded in data collection to avoid miscounting by the automated system) were measured and analyzed with software VideoTrack version 3.5.

Supporting Information

Supporting Information is available from the Wiley Online Library or from the author.

Acknowledgements

This work was supported by ARC Project No. CE140100036 (T.P.D.), the Recruitment Program of "1000plan Youth" and Startup Funds from Tongji University (S.L.), NSF CBET-1553945 (F.D.), and NIH R35GM119691 (F.D.). A.W.P. is supported by a Principal Research Fellowship from the Australian NHMRC. TEM imaging was performed at Bio21 Advanced Microscopy Facility, University of Melbourne and SEM imaging at Ramaciotti Centre for Cryo-Electron Microscopy, Monash University. HIM imaging was performed at the MCFP platform, University of Melbourne by Dr. Babak Nasr. The authors thank Dr. Kevin M. McPeak for discussions. P.C.K. and T.P.D. designed the project. Y.O., J.G., and R.O. performed syntheses and characterizations of silica nanoribbons. A.F. performed ThT, zeta potential, SEM, viability assays, as well as FiberApp statistical analysis. A.K. and A.F. conducted TEM. A.F., G.P., I.J., M.Z., and S.L. designed and conducted in vivo assays. P.F. and A.W.P. performed HPLC and mass spectroscopy. Y.S. and F.D. performed coarse-grained simulations. A.F., P.C.K., and Y.S. wrote the manuscript. All authors agreed on the presentation of the manuscript.

Conflict of Interest

The authors declare no conflict of interest.

Keywords

amyloidogenesis, chirality, human IAPP, silica nanoribbons, toxicity

Received: July 19, 2018
Revised: August 26, 2018
Published online:

[1] L. Haataja, T. Gurlo, C. J. Huang, P. C. Butler, *Endocr. Rev.* **2008**, *29*, 303.
[2] P. Cao, A. Abedini, H. Wang, L. H. Tu, X. Zhang, A. M. Schmidt, D. P. Raleigh, *Proc. Natl. Acad. Sci. USA* **2013**, *110*, 19279.
[3] J. R. Brender, K. Hartman, R. P. R. Nanga, N. Popovych, R. de la Salud Bea, S. Vivekanandan, E. N. G. Marsh, A. Ramamoorthy, *J. Am. Chem. Soc.* **2010**, *132*, 8973.
[4] M. F. Sciacca, D. Milardi, G. M. Messina, G. Marletta, J. R. Brender, A. Ramamoorthy, C. La Rosa, *Biophys. J.* **2013**, *104*, 173.
[5] J. L. Larson, A. D. Miranker, *J. Mol. Biol.* **2004**, *335*, 221.
[6] X. Ge, A. Kakinen, E. N. Gurzov, W. Yang, L. Pang, E. H. Pilkington, P. Govindan-Nedumpully, P. Chen, F. Separovic, T. P. Davis, P. C. Ke, F. Ding, *Chem. Commun.* **2017**, *53*, 9394.
[7] R. P. Nanga, J. R. Brender, S. Vivekanandan, A. Ramamoorthy, *Biochim. Biophys. Acta* **2011**, *1808*, 2337.
[8] P. C. Ke, M. A. Sani, F. Ding, A. Kakinen, I. Javed, F. Separovic, T. P. Davis, R. Mezzenga, *Chem. Soc. Rev.* **2017**, *46*, 6492.
[9] E. H. Pilkington, M. Lai, X. Ge, W. J. Stanley, B. Wang, M. Wang, A. Kakinen, M.-A. Sani, M. R. Whittaker, E. N. Gurzov, F. Ding, J. F. Quinn, T. P. Davis, P. C. Ke, *Biomacromolecules* **2017**, *18*, 4249.
[10] I. Javed, T. Yu, G. Peng, A. Sánchez-Ferrer, A. Faridi, A. Kakinen, M. Zhao, R. Mezzenga, T. P. Davis, S. Lin, P. C. Ke, *Nano Lett.* **2018**, *18*, 5797.
[11] W. Wei, C. Xu, N. Gao, J. Ren, X. Qu, *Chem. Sci.* **2014**, *5*, 4367.
[12] G. Gao, M. Zhang, P. Lu, G. Guo, D. Wang, T. Sun, *Angew. Chem., Int. Ed.* **2015**, *54*, 2245.
[13] G. Qing, S. Zhao, Y. Xiong, Z. Lv, F. Jiang, Y. Liu, H. Chen, M. Zhang, T. Sun, *J. Am. Chem. Soc.* **2014**, *136*, 10736.
[14] Z. Du, Y. Guan, C. Ding, N. Gao, J. Ren, X. Qu, *Nano Res.* **2018**, *11*, 4102.
[15] M. Li, S. E. Howson, K. Dong, N. Gao, J. Ren, P. Scott, X. Qu, *J. Am. Chem. Soc.* **2014**, *136*, 11655.
[16] R. Malishev, E. Arad, S. K. Bhunia, S. Shaham-Niv, S. Kolusheva, E. Gazit, R. Jelinek, *Chem. Commun.* **2018**, *54*, 7762.
[17] X. Wang, X. Wang, M. Wang, D. Zhang, Q. Yang, T. Liu, R. Lei, S. Zhu, Y. Zhao, C. Chen, *Small* **2018**, *14*, 1703982.
[18] A. Kakinen, J. Adamcik, B. Wang, X. Ge, R. Mezzenga, T. P. Davis, F. Ding, P. C. Ke, *Nano Res.* **2018**, *11*, 3636.
[19] D. Shin, D. Banerjee, *Int. J. Heat Mass Transfer* **2011**, *54*, 1064.
[20] I. I. Slowing, B. G. Trewyn, S. Giri, V. S. Y. Lin, *Adv. Funct. Mater.* **2007**, *17*, 1225.
[21] W. Ichinose, M. Miyagawa, Z. An, M. Yamaguchi, *Org. Lett.* **2012**, *14*, 3123.
[22] L. Song, S. Wang, N. A. Kotov, Y. Xia, *Anal. Chem.* **2012**, *84*, 7330.
[23] R. K. Das, O. F. Zouani, C. Labrugère, R. Oda, M.-C. Durrieu, *ACS Nano* **2013**, *7*, 3351.
[24] J. K. Gansel, M. Thiel, M. S. Rill, M. Decker, K. Bade, V. Saile, G. von Freymann, S. Linden, M. Wegener, *Science* **2009**, *325*, 1513.
[25] J. Cheng, G. Le Saux, J. Gao, T. Buffeteau, Y. Battie, P. Barois, V. Ponsinet, M.-H. Delville, O. Ersen, E. Pouget, R. Oda, *ACS Nano* **2017**, *11*, 3806.
[26] T. Delgado-Perez, L. M. Bouchet, M. de la Guardia, R. E. Galian, J. Perez-Prieto, *Chem. - Eur. J.* **2013**, *19*, 11068.
[27] E. Shah, H. P. Soni, *RSC Adv.* **2013**, *3*, 17453.
[28] S. Sudhakar, P. Kalipillai, P. B. Santhosh, E. Mani, *J. Phys. Chem. C* **2017**, *121*, 6339.
[29] T. P. Knowles, M. Vendruscolo, C. M. Dobson, *Nat. Rev. Mol. Cell Biol.* **2014**, *15*, 384.
[30] J. J. Wiltzius, S. A. Sievers, M. R. Sawaya, D. Eisenberg, *Protein Sci.* **2009**, *18*, 1521.
[31] X. Zhang, J. R. St. Clair, E. London, D. P. Raleigh, *Biochemistry* **2017**, *56*, 376.
[32] S. Lin, Y. Zhao, A. E. Nel, S. Lin, *Small* **2013**, *9*, 1608.
[33] A. V. Kalueff, A. M. Stewart, R. Gerlai, *Trends Pharmacol. Sci.* **2014**, *35*, 63.
[34] J. D. Best, W. K. Alderton, *Neuropsychiatr. Dis. Treat.* **2008**, *4*, 567.
[35] E. Brustein, L. Saint-Amant, R. R. Buss, M. Chong, J. R. McDearmid, P. Drapeau, *J. Physiol.* **2003**, *97*, 77.
[36] M. Granato, F. J. van Eeden, U. Schach, T. Trowe, M. Brand, M. Furutani-Seiki, P. Haffter, M. Hammerschmidt, C. P. Heisenberg, Y. J. Jiang, D. A. Kane, R. Kelsh, M. C. Mullins, J. Odenthal, C. Nüsslein-Volhard, *Development* **1996**, *123*, 399.
[37] E. D. Levin, H. A. Swain, S. Donerly, E. Linney, *Neurotoxicol. Teratol.* **2004**, *26*, 719.
[38] J. Geng, M. Li, L. Wu, C. Chen, X. Qu, *Adv. Healthcare Mater.* **2012**, *1*, 332.
[39] W. Ma, L. Xu, A. F. de Moura, X. Wu, H. Kuang, C. Xu, N. A. Kotov, *Chem. Rev.* **2017**, *117*, 8041.
[40] K. M. McPeak, C. D. van Engers, M. Blome, J. H. Park, S. Burger, M. A. Gosálvez, A. Faridi, Y. R. Ries, A. Sahu, D. J. Norris, *Nano Lett.* **2014**, *14*, 2934.
[41] H. E. Lee, H. Y. Ahn, J. Mun, Y. Y. Lee, M. Kim, N. H. Cho, K. Chang, W. S. Kim, J. Rho, K. T. Nam, *Nature* **2018**, *556*, 360.
[42] K. Sugiyasu, S.-I. Tamaru, M. Takeuchi, D. Berthier, I. Huc, R. Oda, S. Shinkai, *Chem. Commun.* **2002**, 1212.
[43] T. Delclos, C. Aimé, E. Pouget, A. Brizard, I. Huc, M.-H. Delville, R. Oda, *Nano Lett.* **2008**, *8*, 1929.
[44] Y. Okazaki, J. Cheng, D. Dedovets, G. Kemper, M.-H. Delville, M.-C. Durrieu, H. Ihara, M. Takafuji, E. Pouget, R. Oda, *ACS Nano* **2014**, *8*, 6863.
[45] I. Usov, R. Mezzenga, *Macromolecules* **2015**, *48*, 1269.
[46] D. C. Rapaport, *The Art of Molecular Dynamics Simulation*, 2nd ed., Cambridge University Press, Cambridge **2004**.
[47] S. Auer, A. Trovato, M. Vendruscolo, *PLoS Comput. Biol.* **2009**, *5*, e1000458.

[48] S. Radic, T. P. Davis, P. C. Ke, F. Ding, *RSC Adv.* **2015**, *5*, 105489.
[49] H. D. Nguyen, C. K. Hall, *Proc. Natl. Acad. Sci. USA* **2004**, *101*, 16180.
[50] B. Urbanc, L. Cruz, S. Yun, S. V. Buldyrev, G. Bitan, D. B. Teplow, H. E. Stanley, *Proc. Natl. Acad. Sci. USA* **2004**, *101*, 17345.
[51] F. Ding, Y. Furukawa, N. Nukina, N. V. Dokholyan, *J. Mol. Biol.* **2012**, *421*, 548.
[52] F. Ding, J. M. Borreguero, S. V. Buldyrey, H. E. Stanley, N. V. Dokholyan, *Proteins: Struct., Funct., Genet.* **2003**, *53*, 220.
[53] F. Ding, D. Tsao, H. Nie, N. V. Dokholyan, *Structure* **2008**, *16*, 1010.
[54] R. Pellarin, P. Schuetz, E. Guarnera, A. Caflisch, *J. Am. Chem. Soc.* **2010**, *132*, 14960.
[55] R. Pellarin, A. Caflisch, *J. Mol. Biol.* **2006**, *360*, 882.
[56] R. Pellarin, E. Guarnera, A. Caflisch, *J. Mol. Biol.* **2007**, *374*, 917.
[57] K. A. Dill, *Biochemistry* **1985**, *24*, 1501.
[58] S. Lin, Y. Zhao, T. Xia, H. Meng, Z. Ji, R. Liu, S. George, S. Xiong, X. Wang, H. Zhang, S. Pokhrel, L. Mädler, R. Damoiseaux, S. Lin, A. E. Nel, *ACS Nano* **2011**, *5*, 7284.

NANO MICRO small

Supporting Information

for *Small,* DOI: 10.1002/smll.201802825

Mitigating Human IAPP Amyloidogenesis In Vivo with Chiral Silica Nanoribbons

Ava Faridi, Yunxiang Sun, Yutaka Okazaki, Guotao Peng, Jie Gao, Aleksandr Kakinen, Pouya Faridi, Mei Zhao, Ibrahim Javed, Anthony W. Purcell, Thomas P. Davis, Sijie Lin,* Reiko Oda,* Feng Ding, and Pu Chun Ke**

Supplementary Information

Mitigating Human IAPP Amyloidogenesis *in Vivo* with Chiral Silica Nanoribbons

Ava Faridi,[†¶] Yunxiang Sun,[£] Yutaka Okazaki,[‡] Guotao Peng,[¶] Jie Gao,[‡] Aleksandr Kakinen,[†] Pouya Faridi,[§] Mei Zhao,[¶] Ibrahim Javed,[†] Anthony W. Purcell,[§] Thomas P. Davis,[†] Sijie Lin,[¶*] Reiko Oda,[‡*] Feng Ding,[£] Pu Chun Ke[†*]*

[†]ARC Centre of Excellence in Convergent Bio-Nano Science and Technology, Monash Institute of Pharmaceutical Sciences, Monash University, 381 Royal Parade, Parkville, VIC 3052, Australia

[¶]College of Environmental Science and Engineering, Shanghai Institute of Pollution Control and Ecological Security, Biomedical Multidisciplinary Innovation Research Institute, Shanghai East Hospital, Tongji University, 1239 Siping Road, Shanghai 200092, China

[£]Department of Physics and Astronomy, Clemson University, Clemson, SC 29634, USA

[‡]Institut Européen de Chimie et Biologie, 2 rue Robert Escarpit, 33607 Pessac, France

[§]Infection and Immunity Program & Department of Biochemistry and Molecular Biology, Biomedicine Discovery Institute, Monash University, Clayton, Victoria 3800, Australia

Email: thomas.p.davis@monash.edu; lin.sijie@tongji.edu.cn; r.oda@cbmn.u-bordeaux.fr; pu-chun.ke@monash.edu

\

Methods

HPLC assay

IAPP was dissolved in 1% formic acid and ran on a 4-6 mm (internal diameter) ×50 mm (length) monolithic reversed-phase C18 high-performance liquid chromatography (HPLC) column (Chromolith SpeedROD; Merck Millipore, Darmstadt, Germany) using an ÄKTAmicro HPLC system (GE Healthcare, Little Chalfont, UK). The mobile phase consisted of buffer A (0.1% trifluoroacetic acid; Thermo Fisher Scientific) and buffer B (80% acetonitrile, 0.1% trifluoroacetic acid; Thermo Fisher Scientific). HLA-peptide mixtures were loaded onto the column and separated using the following chromatographic conditions: 2-15% buffer B over 0.25 min (2 mL/min), 15-30% buffer B over 4 min (2 mL/min), 30-40% buffer B over 8 min (2 mL/min), 40-45% buffer B over 10 min (2 mL/min), 45-99% buffer B over 2 min (1 mL/min), 99-100% buffer B over 2 min (1 mL/min), and was re-equilibrated for 6 min in 2% Buffer B at 2 mL/min.

The IAPP purity was calculated as >95% (**Fig. S1**), by comparing the area of the sample in comparison with the blank.

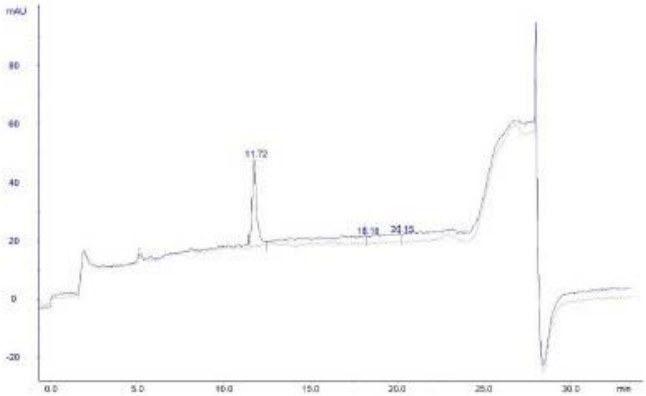

No.	Retention time	Width	Area	Height	Relative area
	min	min	mAU*min	mAU	%
1	11.72	1.01	8.8918	29.926	95.42
2	18.18	0.08	0.2237	2.923	2.4
3	20.15	0.08	0.2032	2.711	2.18

Figure S1. Purity evaluation of the as-purchased IAPP performed by HPLC, showing a purity of >95% for the peptide. mAU: milli-absorption units.

Mass spectroscopy

To confirm the sequence of IAPP, LC-MS/MS was used to identify the intact peptide. For this 160 µg IAPP was dissolved in 100 µL of 1 M Tris buffer (pH=8). For reduction disulphide bind, the IAPP was incubated with 10 mM Tris (2-carboxyethyl) phosphine hydrochloride (Sigma, CAS Number 51805-45-9) for 30 min at 50 °C. Then for cysteine alkylation, it was incubated with 40 mM 2-chloroacetamide (Sigma, CAS Number 79-07-2) in dark at room temperature for 20 min and 1% formic acid was added to change the pH from 8 to 3. The sample was desalted, dried and dissolved in 1% formic acid.

For LC-MS/MS acquisition, peptide-containing fractions were loaded onto a microfluidic trap column packed with ChromXP C18-CL 3-µm particles (300-Å nominal pore size; equilibrated in 0.1% formic acid, 2% acetonitrile) at 5 µL/min with a NanoUltra cHiPLC system (Eksigent). An analytical (75 µm × 15 cm ChromXP C18-CL, 3 µm, 120 Å, Eksigent) microfluidic column was switched in line, and peptides were separated by linear gradient elution with 0–30% buffer B (80% acetonitrile, 0.1% formic acid) over 50 min and 30–80% over 5 min flowing at 300 nL/min. Separated peptides were analyzed with a SCIEX TripleTOF® 6600 mass spectrometer equipped with a Nanospray III ion source and accumulating up to 20 MS/MS spectra per second. The following instrument parameters were used: ion spray voltage, 2,400 V; curtain gas, 25 L/min; ion source gas, 10 L/min; and interface heater temperature, 150 °C. MS/MS switch criteria included the following: ions of m/z >200 amu; charge state, +2 to +5; and intensity, >40 counts per second. The top 20 ions meeting these criteria were selected for MS/MS per cycle. The instrument was calibrated every four LC runs using [Glu1]-Fibrinopeptide B standard.

LC-MS/MS data were searched against the human proteome (UniProt v_05102017) by PEAKS Studio 8.5 (Bioinformatics Solutions) (**Fig. S2A**). MS data files were imported into PEAKS Studio 8.5 (PEAKS de novo, PEAKS DB) and subjected to default data refinement. The parent mass error tolerance was set to 15 ppm and the fragment mass error tolerance 0.1 Da. Carbamidomethylation of cysteine was set as a fix modification. A 1% false discovery rate (FDR) cut-off was applied. In MS1, IAPP was found at 3 multiple charges (**Fig. S2A**). Using MS2, the commercial IAPP was sequenced and confirmed (**Fig. S2B**).

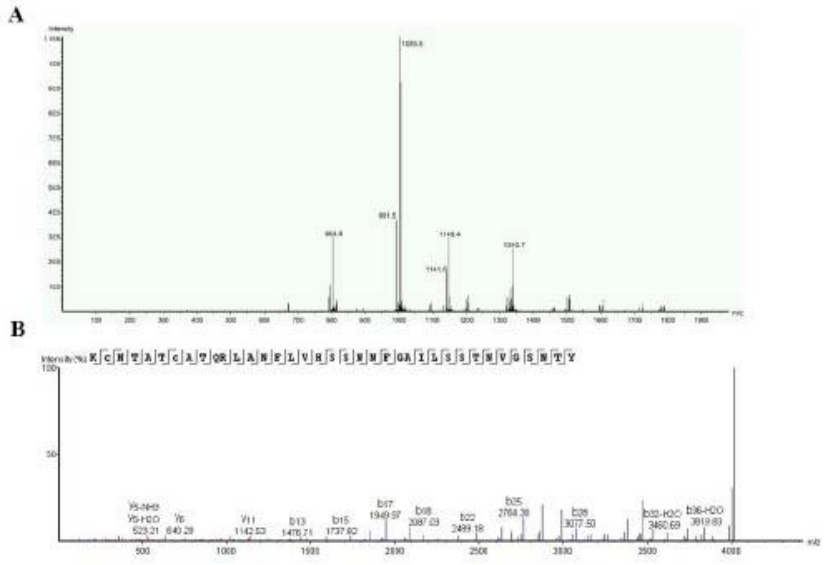

Figure S2. (A) MS1 data for IAPP intact peptide. IAPP was recorded at 3 different charge states. 804.8 corresponds to charge state +5, 1005.5 to charge state +4 and 1340.7 to charge state +3. (B) Sequencing intact IAPP peptide using LC-MS/MS.

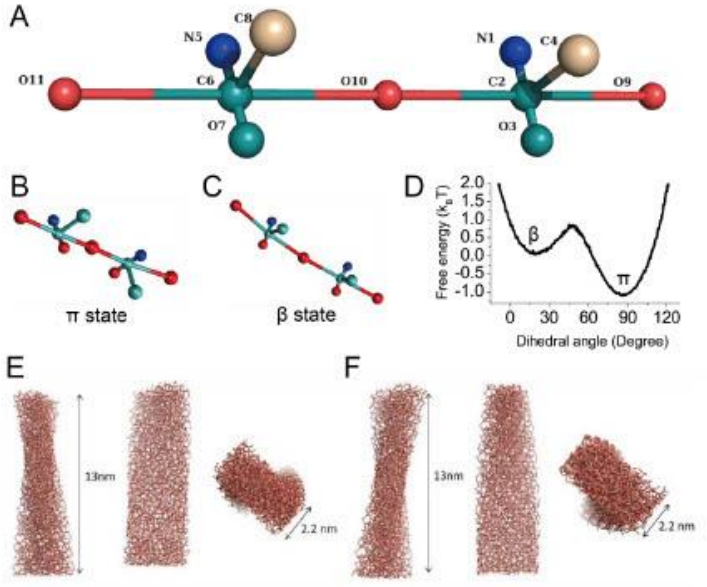

Figure S3. The models of amyloid peptides and chiral silica nanohelices. (A) The coarse-grained model for peptide used in the simulations. (B, C) The two lowest states of amyloid monomer state β and the amyloid-protected state π, respectively. (D) The β and π states of the monomer plotted as a function of the dihedral angle of the two dipoles. (E, F) L/R-SiO_2 with a pitch length of 60 nm and a rotation angle of 70°.

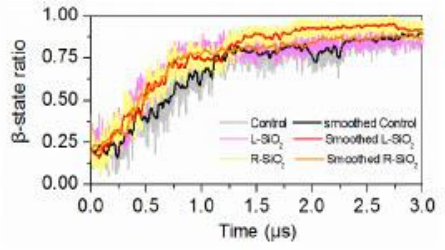

Figure S4. Time evolution of the fraction of peptides in the β -state during the CG peptide aggregation simulations in the absence (control) or presence of the L/R-SiO_2.

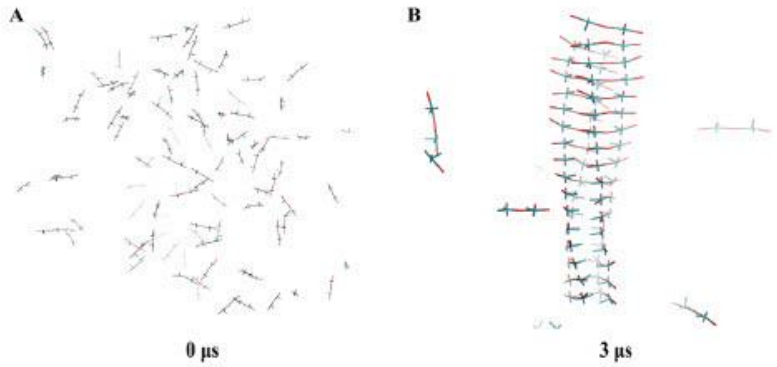

Figure S5. Self-assembly of the coarse-grained peptide in DMD simulations. Starting from randomly positions (A), the peptides spontaneously aggregated into a left-handed fibril structure (B).

Circular dichroism spectroscopy

Circular dichroism (CD) spectra of the fibrillization process of fresh IAPP (25 μM) w/o L/R-SiO_2 were obtained for the wavelength range of 190-260 nm with a 1 nm step size at room temperature (**Fig. S6**). Chirascan Plus qCD instrument (Applied Photophysics) was used to record the spectra. The measurement was performed in triplicate and average spectra of 3 measurements were analyzed.

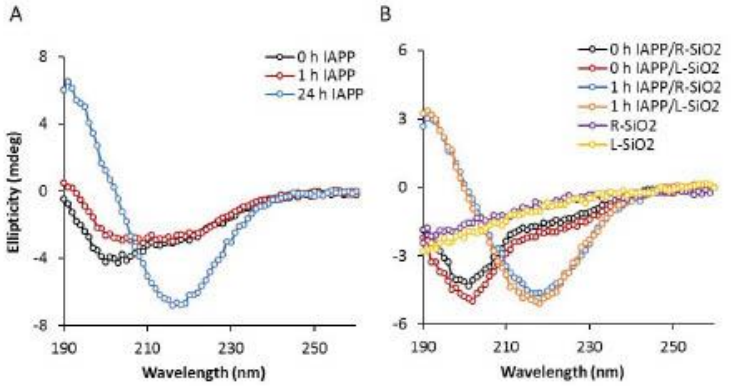

Figure S6. Evolving secondary structures of (A) 25 μM IAPP and (B) IAPP in the presence of the L/R-SiO_2 (at a 1:1 mass ratio). The changing intensities of the CD spectra of IAPP from random structure (minimum at 200 nm) at time zero to β sheets (minimum at 218 nm) after 24 h indicate the amyloid aggregation of IAPP (A). Consistent with the ThT assay, the presence of the L/R-SiO_2 accelerated IAPP fibrillization and a transition from random structure to β sheets within 1 h (B).

MTT viability assay

To further confirm the PI viability assay, a 3-(4,5-Dimethylthiazol-2-Yl)-2,5-Diphenyltetrazolium Bromide (MTT) assay was performed with the L/R-SiO_2 (**Fig. S7**). Specifically, 2×10^4 βTC-6 cells in 200 μL DMEM with 15% FBS were seeded per well in a flat-bottomed 96-well polystyrene coated plate and were incubated for 24 h at 37 °C in a 5% CO_2 incubator. After 24 h of incubation, the cell culture medium was refreshed and samples of 20 μM IAPP and 0.08 mg/mL L/R-SiO_2 (at a 1:1 mass ratio) were added into the wells. After

14 h of treatment, the samples were replaced by 10% MTT in cell culture medium with 15% FBS and incubated at 37 °C in a 5% CO_2 for 4 h. Formed crystals were dissolved in 100 µL of dimethyl sulfoxide and the plates were read immediately in a benchtop multi-mode microplate reader (FlexStation 3 Micro Devices), at 570 nm. All samples were examined in triplicate.

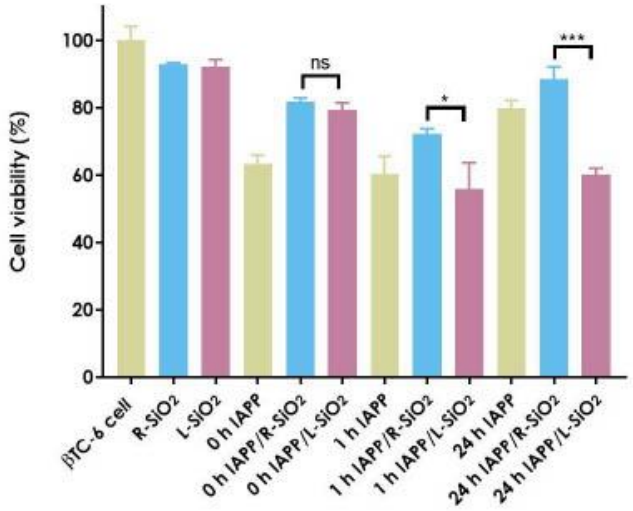

Figure S7. MTT cytotoxicity assay of βTC-6 cells exposed to 0 h, 1 h and 48 h IAPP fibrils in the presence and absence of the L/R-SiO_2 (ns: $P > 0.05$, *: $P \leq 0.05$ and ****: $P \leq 0.0001$). Here the 0 h, 1 h and 48 h aged IAPP refer to IAPP freshly dissolved in water (0 h IAPP), oligomers/protofibrils (1 h into fibrillization), and fibrils (48 h into fibrillization), respectively. The assay was performed in triplicate and the error bars show the standard deviations of the averaged data sets. IAPP concentration: 20 µM, at room temperature and pH 7.

Fibrillization-Control.mpg

7

Video S1. Aggregation of peptides into left-handed fibrils.

Video S2. Aggregation of peptides in the presence of the L-SiO_2.

Video S3. Aggregation of peptides in the presence of the R-SiO_2.

Video S4. The zebrafish larva (4 dpf) treated with 0 h IAPP/L-SiO_2 showed more rotational movement (<180° clock-wise or anti-clockwise) and in some cases circular movement compared with the control and with the R-SiO_2.

Video S5. The untreated zebrafish larva (4 dpf) as control swam in a linear path.

Video S6. The zebrafish larva (4 dpf) injected with 48 h IAPP/L-SiO_2 exhibited the lowest activities in both rotation and swimming distance, indicating the highest toxicity upon interactions between peptide fibrils and nanohelices of the same handedness.

Chapter 4

Graphene quantum dots rescue protein dysregulation of pancreatic β-cells exposed to human islet amyloid polypeptide

1. Declaration and rationale

This chapter was published as **Faridi, A.**, Sun, Y., Mortimer, M., Aranha, R.R., Nandakumar, A., Li, Y., Javed, I., Kakinen, A., Fan, Q., Purcell, A.W., Davis, T.P., Ding, F., Faridi, P., Ke, P.C., Graphene quantum dots rescue protein dysregulation of pancreatic β-cells exposed to human islet amyloid polypeptide, (2019) ***Nano Research***. Reprinted with permission from reference[210] Copyright 2019 American Chemical Society."

This chapter examined, for the first time, dysregulation of intracellular protein expression in pancreatic beta cells exposed to IAPP, as well as their rescue by GQDs. This study filled a knowledge gap on the molecular-level effects of IAPP on β cells, and on the extent of cell recovery from such assault mitigated by nanomaterials. This knowledge justifies and facilitates further studies on the application of nanomaterials against amyloidosis associated with T2D.

Nano Research
2019, 12(11): 2827–2834

ISSN 1998-0124 CN 11-5974/O4
https://doi.org/10.1007/s12274-019-2520-7

Research Article

Graphene quantum dots rescue protein dysregulation of pancreatic β-cells exposed to human islet amyloid polypeptide

Ava Faridi[1], Yunxiang Sun[2,3], Monika Mortimer[4], Ritchlynn R. Aranha[5], Aparna Nandakumar[1], Yuhuan Li[1], Ibrahim Javed[1], Aleksandr Kakinen[1], Qingqing Fan[1], Anthony W. Purcell[5], Thomas P. Davis[1,6] (✉), Feng Ding[3] (✉), Pouya Faridi[5] (✉), and Pu Chun Ke[1] (✉)

[1] *ARC Centre of Excellence in Convergent Bio-Nano Science and Technology, Monash Institute of Pharmaceutical Sciences, Monash University, 381 Royal Parade, Parkville, VIC 3052, Australia*
[2] *Department of Physics, Ningbo University, Ningbo 315211, China*
[3] *Department of Physics and Astronomy, Clemson University, Clemson, SC 29634, USA*
[4] *Institute of Environmental and Health Sciences, College of Quality and Safety Engineering, China Jiliang University, Hangzhou 310018, China*
[5] *Infection and Immunity Program & Department of Biochemistry and Molecular Biology, Biomedicine Discovery Institute, Monash University, Clayton, Victoria 3800, Australia*
[6] *Australian Institute for Bioengineering and Nanotechnology, The University of Queensland, Brisbane Qld 4072, Australia*

Received: 1 July 2019 / **Revised:** 15 September 2019 / **Accepted:** 15 September 2019

ABSTRACT

The amyloid aggregation of peptides and proteins is a hallmark of neurological disorders and type 2 diabetes. Human islet amyloid polypeptide (IAPP), co-secreted with insulin by pancreatic β-cells, plays dual roles in both glycemic control and the pathology of type 2 diabetes. While IAPP can activate the NLRP3 inflammasome and modulate cellular autophagy, apoptosis and extracellular matrix metabolism, no data is available concerning intracellular protein expression upon exposure to the polypeptide. More surprisingly, how intracellular protein expression is modulated by nanoparticle inhibitors of protein aggregation remains entirely unknown. In this study, we first examined the changing proteomes of βTC6, a pancreatic β-cell line, upon exposure to monomeric, oligomeric and fibrillar IAPP, and detailed cellular protein expression rescued by graphene quantum dots (GQDs), an IAPP inhibitor. We found that 29 proteins were significantly dysregulated by the IAPP species, while majority of these proteins were nucleotide-binding proteins. Collectively, our liquid chromatography tandem–mass spectrometry, fluorescence quenching, helium ion microscopy, cytotoxicity and discreet molecular dynamics simulations data revealed a remarkable capacity of GQDs in regulating aberrant protein expression through H-bonding and hydrophobic interactions, pointing to nanomedicine as a new frontier against human amyloid diseases.

KEYWORDS

islet amyloid polypeptide (IAPP), oligomer, amyloid, protein expression, graphene quantum dot

1 Introduction

Human islet amyloid polypeptide (IAPP) is a 37-residue hormone co-secreted and co-stored with insulin in pancreatic β-cells, and is co-released with the latter for satiety signaling [1]. Environmental factors of pH (4.5–5 within β-cells and 7.2 extracellularly), physiological metals (such as Ca^{2+} and Zn^{2+}), glucose homeostasis, insulin, chaperones and chaperone-like proteins (e.g., serum albumin) can trigger the aberrant aggregation of IAPP from monomers to oligomers, protofibrils and amyloid fibrils, thereby eliciting toxicity to β-cells. The implications of IAPP toxicity range from cell degeneration to insulin deficiency and type 2 diabetes (T2D), a disease debilitating 370 million people worldwide [2–5].

Mounting evidence has implicated the oligomers and protofibrils, among all forms of amyloid protein aggregates, as the most toxic [6, 7]. One working mechanism is that the toxicity of amyloid proteins is rendered through their transformations from random to alpha helical- and then β-sheet-rich conformations, upon their N-termini initiated association with cell membranes [1, 8]. As a result, oligomeric proteins can increase porosity and fluidity of the membranes, impact concentration gradients and transport of biometals and nutrients, and compromise integrity of cell molecular machines and organelles to trigger a host of cellular responses ranging from reactive oxygen species (ROS) production, autophagy and apoptosis, to extracellular matrix metabolism and, ultimately, cell death [1].

To date, only a handful of studies have detailed the adverse effects of amyloid proteins on cellular protein and gene expressions [9, 10]. Among the data available, it has been shown that amyloid beta (Aβ) impacted pathways are important for neuronal physiology and dysregulation in Alzheimer's disease (AD), including cell adhesion, vesicle trafficking, actin cytoskeleton dynamics and insulin signaling. Compared with Aβ, little known about the effects of IAPP aggregation species on the proteome of pancreatic β-cells, and no data is available concerning the effects of IAPP aggregation inhibitors on intracellular protein expression, two glaring knowledge deficiencies which hinder the development of new therapeutics against T2D.

Address correspondence to Thomas P. Davis, thomas.p.davis@monash.edu; Feng Ding, fding@clemson.edu; Pouya Faridi, pouya.faridi@monash.edu; Pu Chun Ke pu-chun.ke@monash.edu

Among current mitigation strategies, aggregation inhibition with small molecules (epigallocatechin-3-gallate or resveratrol) [11, 12] and nanomaterials (OH-terminated PAMAM dendrimers, chiral silica nanohelices, beta-lactoglobulin-coated gold nanoparticles, silver nanoparticles, iron oxide nanoparticles, and carbon nanotubes, etc.) has been shown effective for the prevention of IAPP toxicity *in vitro* (buffer or beta cells), *ex vivo* (beta-cell islets) or *in vivo* (zebrafish embryos) [13–16]. Graphene quantum dots (GQDs), specifically, are a miniaturized derivative of graphene sheets possessing no toxicity up to 500 μg/mL [17] and a superior translocation efficacy across the blood-brain barrier [18]. Carboxylated GQDs, for example, have been recently demonstrated as potent inhibitors against IAPP amyloidogenesis in zebrafish embryos [19] as well as synucleinopathies in the brain of a Parkinson's disease (PD) mouse model [18]. The unique amphiphilic 2D structure and large surface area of GQDs are especially suited for interfacing amphiphilic amyloid proteins than serum proteins, as amyloid proteins evolve from disordered monomers to increasingly hydrophobic and toxic oligomers and protofibrils [1]. Such increasing hydrophobicity entails high affinity of amyloid proteins for the hydrophobic GQD moieties, while the OH groups of the GQDs further mediate H-bonding with amyloid proteins to enhance their association [16]. The autofluorescence of GQDs, resulting from their quantum confinement effect, may be utilized for tracking the biodistribution of the nanomaterial *in vivo*, among other applications.

In recent years, high-throughput proteomic techniques have been used to evaluate the effect of amyloidogenesis on the initiation and progression of amyloid diseases such as AD [20, 21]. To facilitate the development of nanomedicines as a new frontier against amyloid diseases, in this study we used liquid chromatography tandem–mass spectrometry (LC-MS/MS) to characterize the protein expression profiles of the βTC6 pancreatic β-cell line exposed to three structurally representative IAPP species, namely, IAPP monomers (IAPPm), oligomers (IAPPo) and amyloid fibrils (IAPPf). Driven by the findings we further studied protein expression regulated by hydroxylated GQDs (20 μg/mL) subsequent to β-cell exposure to the IAPP species to explore the potential of the nanomaterial against cell degeneration in T2D. We found proteins which regulate gene expression, especially nucleotide-binding proteins, were most prone to the toxic forms of IAPP, while the hydroxylated GQDs partially reversed the dysregulation effects of IAPPm and IAPPo through H-bonding and hydrophobic interactions for the majority of these proteins, implicating the potential of the nanomaterial against cell degeneration in T2D.

2 Results and discussion

2.1 Characterization of GQDs and three IAPP aggregation states

Transmission electron microscopy (TEM) imaging indicated that GQDs were relatively uniform and monodisperse disks of ~ 3.8 ± 0.5 nm in lateral dimensions (Fig. S1(a) in the Electronic Supplementary Material (ESM)). The zeta potential of the hydroxylated GQDs was charge neutral at 0.78 ± 0.1 mV in aqueous solutions, which differed from the negative charge of carboxylated GQDs used in the study by Wang et al. against IAPP amyloidogenesis *in vivo* [19]. The use of hydroxylated GQDs in the present study intended to utilize their capacity in forming H-bonding with IAPP for aggregation and toxicity inhibition. The hydrophobic moieties of GQDs also favored binding with the hydrophobic and toxic IAPP species to drive their aggregation off pathway. The Fourier transform infrared (FTIR) spectrum of the GQDs indicated the presence of oxygen-functional groups, confirming the enrichment of hydroxyl groups (–OH) with a peak at wavenumber of ~ 3,400 cm^{-1}, and the main components of C=C, C–O and CH bonds at wavenumbers of ~ 1,560, 1,040, and 2,900 cm^{-1}, respectively (Fig. S2(a) in the ESM). Furthermore, thermogravimetric analysis (TGA) of GQDs (Fig. S2(b) in the ESM) indicated decreases in mass as a function of rising temperature. The TGA curve exhibited two steps of weight losses between 50 and 150 °C under N_2, with a ~ 50% weight loss occurring at 100 °C. These weight losses corresponded to the detachment of abundant oxygen-containing groups such as hydroxyls and C–O within the GQDs, in addition to evaporation of solvent at the early stage of the weight loss. The maximum fluorescence excitation and emission of GQDs occurred at 350 and 440 nm, respectively (Fig. S3(a) in the ESM).

Freshly dissolved hexafluoro-2-propanol (HFIP)-treated IAPP in Milli-Q water assumed the monomeric form (IAPPm). Oligomeric IAPP (IAPPo) was prepared by incubating the HFIP-treated IAPP in Milli-Q water at room temperature for 1 h, while full-length IAPP mature fibrils (IAPPf) were obtained by incubating the peptide at room temperature for more than 24 h. All three fibrillization states were confirmed by TEM imaging (Figs. S1(c)–S1(e) in the ESM) and by atomic force microscopy in our previous experimental studies [11, 22].

IAPPf remodelling by the GQDs was imaged by TEM (Fig. S1(f) in the ESM). FiberApp [23] was used to quantify the key mesoscopic parameters, including the contour length and persistence length of the fibrils w/o the GQDs. Specifically, IAPPf were micrometers in length and ~ 10–15 nm in diameter (Fig. S1(e) inset in the ESM), consistent with the literature [1]. Upon interaction with the GQDs, the preformed fibrils assumed heterogeneous length distribution with major fraction (40%) being 400 nm in length (Fig. S1(f) inset in the ESM) as determined by FiberApp. Such analysis was not feasible for IAPPm and IAPPo, due to the ineffectiveness of FiberApp for analyzing non-tubular morphologies.

2.2 Fluorescence quenching revealed IAPP-GQD association

To probe the interactions between GQDs and IAPP, the quenching of GQD autofluorescence by the three IAPP aggregation states of different concentrations (10–30 μM) was recorded. At fixed excitation wavelength of 350 nm and GQD concentration of 300 μg/mL, the peak emission fluorescence intensity of GQDs at 440 nm decreased linearly for IAPPm, IAPPo and IAPPf (R^2 = 0.985, R^2 = 0.932, R^2 = 0.999) with increasing IAPP concentrations (Figs. S3(b)–S3(g) in the ESM). These reductions in GQD fluorescence intensity, at 7% for IAPPm, 11% for IAPPo and 9% for IAPPf each of 20 μM (the concentration used for viability, ROS and proteomics assays), suggest associations of the monomeric, protofibrils and fibrils of IAPP during aggregation. The binding of the GQDs and the IAPP species was further studied by computer simulations (Fig. 1 and Fig. S4 in the ESM).

2.3 Discrete molecular dynamics (DMD) simulations of IAPP-GQD association

To complement the quenching assay, molecular details of the interactions between IAPP and GQDs were further studied by discrete molecular dynamics (DMD) simulations (Fig. 1 and Fig. S4 in the ESM). The IAPPm mainly adopted unstructured conformation (i.e., random coils and bends) with some partial helical and transient β-sheet structures (Fig. S4(a) in the ESM). In the presence of a GQD nanosheet, the structured conformation (helix and β-sheet) of IAPPm was completely destructed. The distribution of hydrogen bonds formed by main-chain atoms of IAPPm in both systems revealed the hydrogen bonds in IAPPm were significantly cleaved off by the GQD (Fig. S4(b) in the ESM). Moreover, IAPPm had a strong propensity of forming hydrogen bonds with the GQD. The minimum distance probability distribution of each IAPPm residue relative to the GQD revealed that all of the residues in IAPPm adsorbed onto the GQD surface with a most populated distance

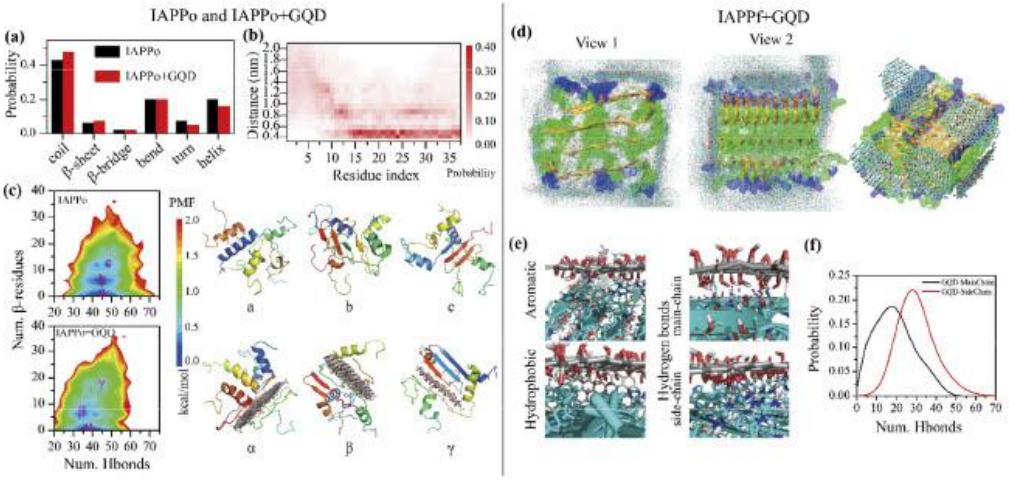

Figure 1 DMD simulations of GQD interacting with IAPPo and IAPPf. (a) Secondary structure of IAPPo in the absence and presence of the GQD. (b) Distance probability distribution of each IAPPo residue to the GQD. (c) Two-dimensional potential mean force (2D-PMF) of the IAPPo w/o the GQD. Three different types of IAPPo structures – including helical (a/α), partial β-sheet (b/β) and β-sheet rich (c/γ)-of the IAPPo (top right) and the IAPPo with the GQD (bottom right) were also presented with the coordinates labelled in the PMF on the left. DMD simulation of GQDs interacting with IAPPf. (d) Structures of GQD sheets bound on the surface of an IAPPf, obtained from different independent DMD trajectories. A representative GQD-IAPPf complex structure is shown to the right. (e) The GQD-IAPPf binding interfaces highlight the dominant inter-molecular interactions. (f) Probability distribution of the number of hydrogen bonds formed by GQD with the main-chains or side-chains of the IAPPf.

occurring at 0.4–0.5 nm (Fig. S4(c) in the ESM). The binding site distribution of IAPPm on the GQD surface indicated that IAPPm mainly bound to the nanosheet surface rather than the edges (Fig. S4(d) in the ESM). Overall, the structured conformation (helix or partial β-sheet, Fig. S4(e) in the ESM) of IAPPm was nearly completely converted into unstructured conformation (Fig. S4(f) in the ESM) in the presence of the GQD.

To investigate the effects of GQD on the conformations of IAPPo, we simulated four IAPP peptides with and without a GQD nanosheet. The random coil and β-sheet structures were slightly enhanced while the helical structures were weakly reduced in the presence of the GQD (Fig. 1(a)). Different from IAPPm, only residues 14–37 of IAPPo displayed high binding probabilities with the GQD. In addition to the first residue layer at ~ 0.5 nm from the nanosheet surface, a second layer of residues at ~ 0.9 nm from the nanosheet was also observed, though with a lower population. Examination of the simulation snapshots revealed that residues in this region could form some β-sheets perpendicular to the GQD (Fig. 1(b)). The N-terminal residues 1–10 were mainly unbound. The conformational distribution of IAPPo was also analyzed by computing 2D-PMF (i.e., two-dimensional potential of mean force) as a function of the total number of hydrogen bonds formed by main-chain atoms (Num. Hbonds) and the number of residues adopting the β-sheet structure (Num. β-sheet residues). For both systems, IAPPo predominantly adopted a helical-rich structure with a large number of hydrogen bonds and a low β-sheet content (Fig. 1(c)-a, the α state). Besides, β-sheet containing conformations were also observed (Fig. 1(c)-(b and c), the β and γ states). Similarly to IAPPm, the total number hydrogen bonds in IAPPo was also suppressed with the GQD. Overall, these results indicate that GQDs displayed distinct effects on the secondary structure of IAPPm and IAPPo. In addition, the N-terminal residues in IAPPo (Fig. 1(b)) display much weaker binding strength with than those residues in IAPPm (Fig. S4(c) in the ESM).

To understand the conformation of IAPPf interacting with a GQD, we simulated five GQD nanosheets binding with a 20-peptide IAPP fibril (Figs. 1(d)–1(f)). Ten independent DMD simulations which started with different initial structures and velocities were performed. The GQD nanosheet could bind both the elongation and secondary nucleation surfaces of the IAPPf to hinder the fibril growth (Fig. 1(d)). The driving forces of the binding were mainly aromatic, hydrophobic and hydrogen bonds (Fig. 1(e)). The GQD displayed a high propensity to form hydrogen bonds with both the main-chains and side-chains of the IAPPf (Fig. 1(f)). The strong binding affinity was indicated by a high potential energy gain of ~320 kcal/mol upon binding five GQD nanosheets averaged over ten different independent simulations (Fig. S5 in the ESM). In addition, the coating of GQDs on the surface of IAPPf also reduced direct interaction of the fibril with cells.

2.4 Graphene quantum dots mitigated IAPP toxicity *in vitro*

As with Aβ and alpha synuclein, oligomeric/protofibrillar forms are also known as the most toxic IAPP species associated with β-cell degeneration [14, 24, 25]. To quantify the toxicities of IAPP structures with and without GQDs to βTC6 cells, viability (Fig. 2(a), for 15 h of incubation. In Fig. S6 in the ESM, for 24 h of incubation in complete Dulbecco's modified Eagle's medium with 15% fetal bovine serum) and ROS assays were performed. As expected, the most potent IAPP species in inducing cell death, membrane damage as well as intracellular ROS generation were IAPPo (Fig. 2 and Figs. S6 and S7 in the ESM). Neither IAPPm nor IAPPf caused significant cell death or membrane damage, however, IAPPm induced comparable levels of intracellular ROS with IAPPo (Fig. 2(j)), suggesting a higher potential for toxicity of IAPPm compared to IAPPf. Helium ion microscopy (HIM) further demonstrated, consistently with the viability and ROS assays, that IAPPo treated cells acquired a severely deformed morphology and membrane blebbing compared to untreated control cells and IAPPm and IAPPf treated cells (Figs. 2(b), 2(d), 2(f), and 2(h), and Fig. S7 in the ESM). However, the morphology of IAPPm treated cells was more similar to IAPPo-incubated cells,

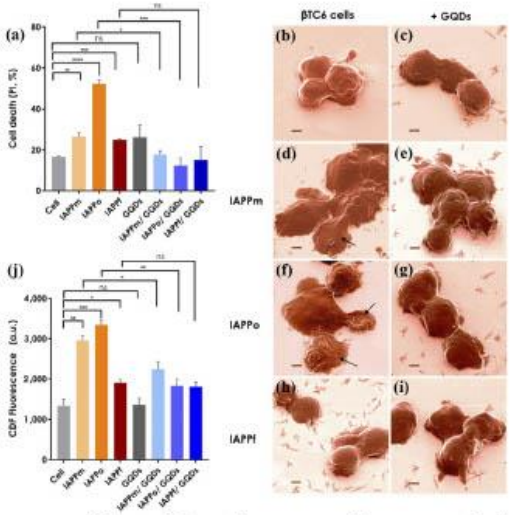

Figure 2 Viability, morphology and ROS generation of βTC6 pancreatic β-cells exposed to the IAPP species with or without GQDs. (a) βTC6 cell toxicities upon exposure to IAPPm, IAPPo and IAPPf in the presence and absence of GQDs. The GQDs were effective in reducing IAPP toxicity of all structures, especially IAPPo as the most toxic species, indicating a strong hydrogen and hydrophobic binding affinity between GQDs and IAPP. PI: propidium iodide. (b)–(i) Helium ion microscopy images as a visual evidence on toxicity of IAPP species: (b) βTC6 cells as control, treated with (c) GQDs and ((d), (f), (h)) IAPPm, IAPPo and IAPPf and ((e), (g), (i)) IAPPm, IAPPo and IAPPf withGQDs, respectively. Arrows in (d) and (f) show the deformation of cell membranes induced by IAPPm and IAPPo, respectively. In the cases of IAPPf and mixture of IAPPf with GQDs no damage was observed. Scale bars: 2 μm. Cells were incubated with IAPP species, with or without GQDs, in the viability assay for 15 h and before HIM for 1 h. (j) Intracellular ROS levels upon exposure to IAPPm, IAPPo and IAPPf in the presence and absence of GQDs. Incubation: 1 h. The experiments were carried out in triplicate, error bars show standard deviations and q-value performed by 1% FDR rate approach by using the two-stage step-up method of Benjamini, Krieger and Yekutieli (ns: $q \geq 0.01$, *: $q < 0.01$, **: $q \leq 0.001$, ***: $q \leq 0.0001$ and ****: $q \leq 0.00001$). IAPP concentration: 20 μM.

likely caused by IAPPm induced oxidative stress as indicated by relatively high intracellular ROS levels (Fig. 2(j)). Co-incubation of pancreatic β-cells with IAPPm or IAPPo and GQDs significantly mitigated IAPP-induced toxicity. In the case of IAPPm, GQDs were potent in alleviating IAPP toxicity by ~ 34%. With IAPPo, the GQDs reduced IAPP cytotoxicity by 76%, confirming a stronger binding affinity between the two species. (Fig. 2(a)). Consistent with the viability assay, significant reduction in intracellular ROS (24.5% for IAPPm and 45.4% for IAPPo) was observed for IAPP with the GQDs, indicating the mitigation power of the nanoparticles against ROS production by the IAPP species (Fig. 2(j)), especially by IAPPo. This may be attributed to the relatively high hydrophobicity of IAPPo and protofibrils [24, 25], which should bind preferably with the hydrophobic moieties of the GQDs than with other cellular proteins to sequester the peptide from aggregation and eliciting toxicity. In comparison, no cell damage was noticeable in the HIM images when the cells were exposed to IAPPm or IAPPo in the presence of the GQDs, and, as expected, no cell deformation was recorded after exposure to IAPPf with the GQDs (Figs. 2(b)–2(i)). Consistently, confocal fluorescence microscopy indicated more cell damage (red fluorescence spots) by IAPPm and IAPPo than IAPPf, and the presence and cellular distributions of the IAPP aggregates (green fluorescence spots) (Fig. S8 in the ESM).

2.5 Effects of IAPP on the proteome of pancreatic β-cells

Following the experimental design of proteomics analysis (Fig. 3(a)), we identified 1,608 proteins across all the samples (Fig. 3(b)). Label-free quantification analysis showed that IAPPm induced an over-expression of 11 proteins and under-expression of another 11 proteins. The addition of GQDs inhibited the IAPPm-induced over/under expression of 10 proteins, respectively. In comparison, IAPPo induced the over-expression of 10 proteins and under-expression of another 10 proteins, out of which the aberrant expressions of 19 proteins were mitigated by GQDs. The comparable capacities of IAPPm and IAPPo in protein dysregulation and ROS production (Figs. 2(j) and 3(c)) may be attributed to the rapid aggregation of the peptide. One of the most amyloidogenic proteins known [26, 27], IAPPm could be converted to IAPPo in hours or less at micromolar concentrations [3, 11, 15, 28]. As expected, IAPPf, the least toxic form

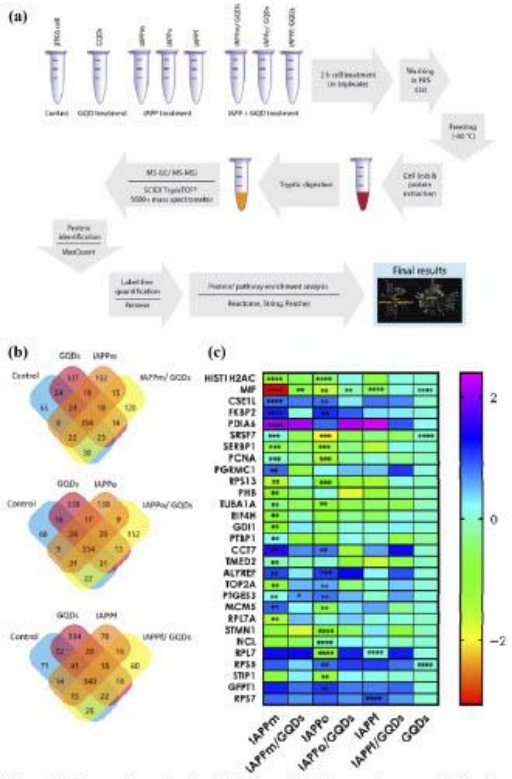

Figure 3 Proteomics analysis of IAPP- and GQD-treated pancreatic β-cells. (a) Scheme of experimental procedures for quantifying up- and down-regulation of intracellular protein expression in β-cells exposed to IAPP species in the absence and presence of GQDs. (b) More than 1,600 proteins were identified across all replicates with more than 50% overlap within each condition. (c) In total, expressions of 29 proteins were altered by the different forms of IAPP treatments. Statistical analysis was done based on the multiple t-test for the average abundance of proteins in each condition compared to the untreated control sample. **, ***, and **** indicate adjusted p-values of $p < 0.01$, $p < 0.001$, and $p < 0.0001$ respectively. The color gradient is the indicator of fold changes compared to the control sample. Based on the adjusted p-value analysis, GQDs alone induced no significant up or down protein expression. In the case of RPL7, both IAPPo and IAPPf showed significant dysregulation ($p < 0.0001$). However, IAPPo and IAPPf with GQDs recovered from significant changes.

of IAPP, caused an over-expression of only one protein and under-expression of two other proteins, with no detectable changes in protein expression when cells were co-incubated with IAPPf and GQDs (Fig. 3(c)).

2.6 Pathway classification of differentially expressed proteins

Biochemical pathway analysis was used to classify differentially expressed proteins from the β-cells treated with the three IAPP species. To achieve this, pathway classification was performed on the differentially expressed proteins identified in each comparison test by *Reactome* [29]. The canonical pathway analysis (Fig. 4 and Fig. S9 in the ESM) of three treatments revealed that DNA-repair and replication, cell cycle, gene expression and metabolism of proteins were the pathways mainly affected by IAPPm and IAPPo. Unsurprisingly, the fewest number of pathways were affected by IAPPf. IAPPo has been reported to cause highest membrane disorders and cytotoxicity [24, 30]. Consistently, and for the first time, IAPPo were the most destructive structure in dysregulating the proteins pathways. We also found proteins in the same pathway could be regulated in different ways (up/down). Based on the differential expression of proteins following exposure to IAPP aggregates we visualized changes to protein networks using STRING [31, 32], as presented in Fig. 5 and Tables S1 and S2 in the ESM.

2.7 Nucleic acid binding proteins as most affected by IAPP

We used Panther Gene Ontology software [33] to determine the proteins mostly altered by IAPP in each condition. A total of 15 out

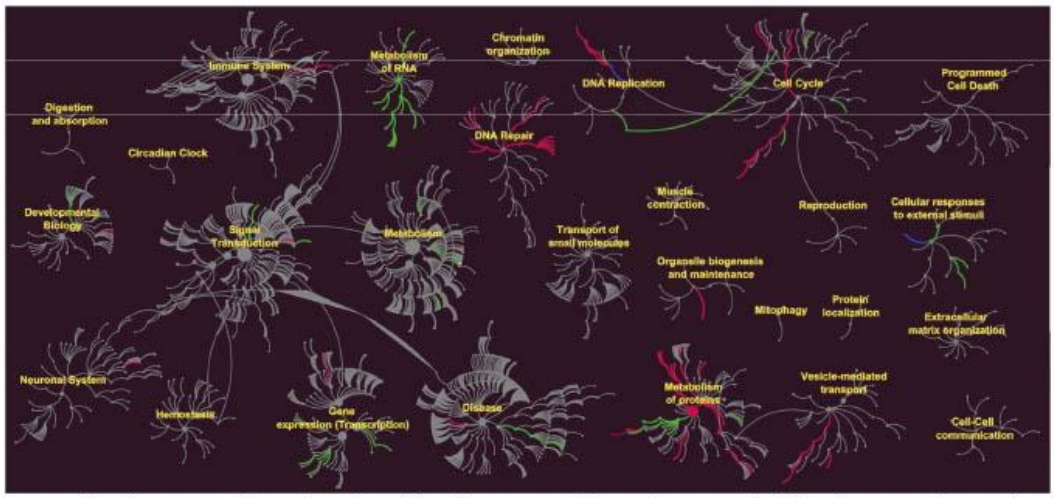

Figure 4 Effects of IAPPo on up and down regulation of intracellular pathways. *Reactome* pathways nodes are represented as filled circles. Connections between pathways and sub-pathways (edges) are represented by lines. The green edges represent up regulation and red edges down regulation. In some pathways both up and down regulations of proteins were recorded, shown as blue lines. DNA repair, metabolism of proteins, gene expression and cell cycle pathways were dysregulated by IAPPo.

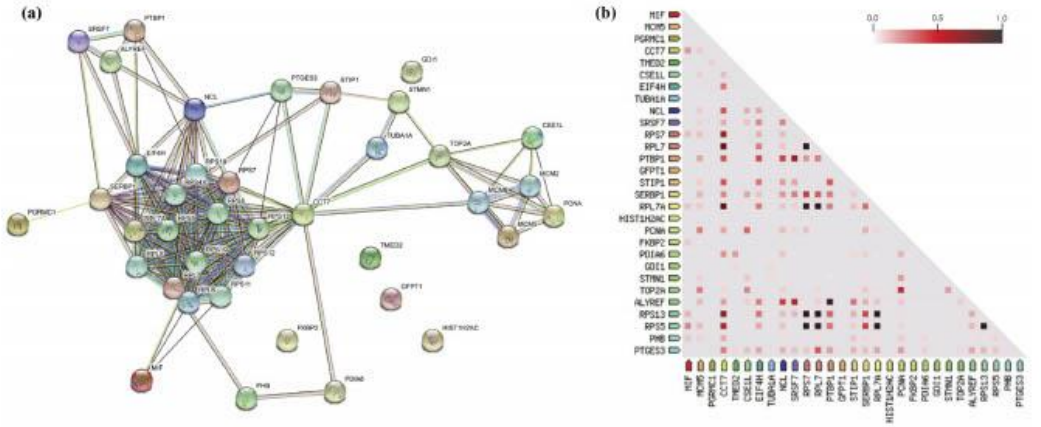

Figure 5 Protein-protein interaction analysis and co-expression of dysregulated proteins by all three IAPP species. (a) STRING database was used for protein-protein interaction analysis with a minimum interaction score of 0.400. (b) Co-expression analysis of IAPP dysregulated proteins. The color code indicates the highest correlation of proteins as 1.0 (black) and the least as 0.0 (white). Enrichment analysis, molecular action legends and co-expression scores are shown in Table S1 in the ESM.

of 29 altered proteins were "binding proteins". Interestingly, 13 proteins were "nucleic acid-binding proteins", including 3 DNA binding and 10 RNA binding (Table S1 in the ESM).

We found six ribosomal proteins, including RPL7, RPS5, RPS13, RPL7A, RPS7 and CCT7, differentially regulated by the IAPP species. A ribosomal protein is any of the proteins that, in conjunction with rRNA, makes up the ribosomal subunits involved in the cellular process of translation. Although ribosomal proteins are known for playing an essential role in ribosome assembly and protein translation, ribosome-independent functions have also been documented [34]. The roles of ribosomal proteins in amyloid diseases such as AD have been studied. For example, a new study shows that Aβ induced changes in multiple proteins involved in ribosomal machinery [35]. In addition, investigation on the chaperone activity of CCT7 for oxidative stress in neuronal apoptosis has been performed [36, 37]. In our study, specifically, the expressions of RPS13 and CCT7 increased in the β-cells treated with IAPPm and IAPPo. Although the regulation of RPS5 by IAPPm was not statistically significant, its expression was significantly decreased by IAPPo. Previously, the overexpression of RPS13 and RPS5 have been reported in AD [38]. We noted significant decreases in the expression of RPL7 by IAPPm and IAPPf and of RPL7A by IAPPm. However, to our knowledge, there are no reports on the dysregulation of these 60s ribosomal proteins in amyloidogenesis.

Alternative splicing has recently become a new mechanism for deciphering different diseases such as diabetes [39, 40] and AD, with RNA-splicing as a major genetic footprint to the diseases [41]. Here our results indicated IAPP could interfere with the regulation of mRNA splicing factor proteins, including nucleolin and SRSF7. SRSF7 was upregulated after treatment with IAPPm but downregulated by IAPPo.

There is increasing evidence that many RNA-binding proteins (RBPs) and RBP-regulated RNA networks are disrupted under diabetic conditions [39]. Here we found two altered RBPs in the β-cells exposed to the toxic forms of IAPP: both IAPPm and IAPPo increased the expression of SERBP1 but decreased the expression of Tho4.

All three IAPP species induced the expression of macrophage migration inhibitory factor (MIF) protein. MIF is a key proinflammatory cytokine involved in many inflammatory reactions and disorders. In addition to its inflammatory roles, MIF can form amyloid fibrils associated with amyloidogenic proteins such as Aβ and alpha synuclein during acid denaturing conditions [42]. Previous studies have suggested that binding of Aβ to microtubules may explain, in part, the mechanism of amyloid induced toxicity [43, 44]. In addition, the cross-interactions between Aβ with IAPP and insulin have been reported [45–47], reinforcing the importance of the findings in this study. Here we found that TUBA1A (a major constituent of microtubules) and STMN1 (involved in the regulation of microtubules) were regulated by IAPPm and IAPPo. Both IAPPm and IAPPo increased the expression of TUBA1A, while IAPPo decreased the expression of STMN1.

2.8 GQDs prevented IAPP-induced toxicity

The effects of GQDs on the inhibition of the fibrillization and toxicity of Aβ and IAPP have been shown in previous studies [19, 48]. In this study, we observed the remarkable effect of the hydroxylated GQDs on the inhibition of protein dysregulation, especially for the most toxic form of IAPPo. The GQD concentration used in this study, at 20 μg/mL, was one order of magnitude lower than its toxic concentration [17, 49, 50], but was adequate for mitigating the toxicity of IAPP at μM concentrations, a condition which triggers β-cell degeneration *in vivo* [1]. GQDs prevented or significantly decreased the level of protein dysregulation (compared with the untreated control) induced by all three forms of IAPP. As shown in Fig. 3(c), 20 out of the 22 proteins that affected by IAPPm, 19 out of the 20 proteins affected by IAPPo and all dysregulation caused by IAPPf were mitigated by GQDs. The nanostructures themselves did not cause significant changes (or with low fold changes) on the protein expression of β cells. Interestingly, GQDs could prevent the adverse effects on the MIF proteins induced by all three IAPP species. PDIA6 protein catalyzes the formation, reduction, and isomerization of disulfide bonds in proteins and also acts as a chaperone in the inhibition of protein misfolding [51]. This protein was remarkably upregulated by IAPPm, but with GQDs the level of dysregulation induced by IAPPm was decreased to with no significant difference from untreated cells (the control). The dysregulation of the IAPP structures in contrast to the constructive effects of GQDs are consistent with the *in vitro* toxicity assay of IAPP on pancreatic β-cells (Fig. 2(a)).

3 Conclusions

Protein expression and cellular pathways regulated by IAPPm and the two major IAPP aggregating species IAPPo and IAPPf were studied along with the impact of hydroxylated GQDs on amyloidosis. Using a comprehensive LC-MS/MS approach, a total of 1,608 proteins were identified in all samples, where 29 proteins showed significant over/under expression, and among them over 30% were RNA and DNA binding proteins. Such aberrant protein expression was mitigated by the GQDs to various extents, among which the most significant effect was shown for IAPPo, the most toxic species of the three aggregation states. These protein expression profiles showed a good correlation with biophysical (fluorescence quenching and HIM imaging) and toxicity (viability and ROS assays) characterizations, where IAPPo elicited the most damage to β-cells and which was ameliorated by GQDs. The binding between the IAPP species and GQDs was a result of H-bonding and hydrophobic interaction, as revealed by atomistic DMD simulations. Together, this study has demonstrated the potency of nanoparticles in restoring protein expression against the toxicity elicited by amyloid protein aggregation, thereby facilitating the development and application of novel therapeutics against a range of amyloid diseases.

Acknowledgements

This work was conceived by PCK, and was by supported by ARC Project No. CE140100036 (Davis), NSF CAREER CBET-1553945 (Ding), NIH MIRA R35GM119691 (Ding), AFTAM Research Collaboration Award (Davis and Ke), the National Natural Science Foundation of China (No. 11904189) (Sun), and the Juvenile Diabetes Research Foundation (Purcell and Faridi). A.W. P. is supported by a Principal Research Fellowship from the Australian NHMRC. TEM imaging was performed at Bio21 Advanced Microscopy Facility, University of Melbourne. HIM imaging was performed at the MCFP platform, University of Melbourne by Dr. Anders Barlow.

Electronic Supplementary Material: Supplementary material (materials and methods, Figs. S1–S9 in ESM and Tables S1 and S2 in ESM) is available in the online version of this article at https://doi.org/10.1007/s12274-019-2520-7.

References

[1] Ke, P. C.; Sani, M. A.; Ding, F.; Kakinen, A.; Javed, I.; Separovic, F.; Davis, T. P.; Mezzenga, R. Implications of peptide assemblies in amyloid diseases. *Chem. Soc. Rev.* **2017**, *46*, 6492–6531.

[2] Zhang, X. X.; St. Clair, J. R.; London, E.; Raleigh, D. P. Islet amyloid polypeptide membrane interactions: Effects of membrane composition. *Biochemistry* **2017**, *56*, 376–390.

[3] Cao, P.; Abedini, A.; Wang, H.; Tu, L. H.; Zhang, X. X.; Schmidt, A. M.; Raleigh, D. P. Islet amyloid polypeptide toxicity and membrane interactions.

Proc. Natl. Acad. Sci. USA **2013**, *110*, 19279–19284.
[4] Knowles, T. P. J.; Vendruscolo, M.; Dobson, C. M. The amyloid state and its association with protein misfolding diseases. *Nat. Rev. Mol. Cell Biol.* **2014**, *15*, 384–396.
[5] Sudhakar, S.; Kalipillai, P.; Santhosh, P. B.; Mani, E. Role of surface charge of inhibitors on amyloid beta fibrillation. *J. Phys. Chem. C* **2017**, *121*, 6339–6348.
[6] Haataja, L.; Gurlo, T.; Huang, C. J.; Butler, P. C. Islet amyloid in type 2 diabetes, and the toxic oligomer hypothesis. *Endocr. Rev.* **2008**, *29*, 303–316.
[7] Chen, X. B.; Mao, S. S. Titanium dioxide nanomaterials: Synthesis, properties, modifications, and applications. *Chem. Rev.* **2007**, *107*, 2891–2959.
[8] Fusco, G.; Chen, S. W.; Williamson, P. T. F.; Cascella, R.; Perni, M.; Jarvis, J. A.; Cecchi, C.; Vendruscolo, M.; Chiti, F.; Cremades, N. et al. Structural basis of membrane disruption and cellular toxicity by α-synuclein oligomers. *Science* **2017**, *358*, 1440–1443.
[9] Sebollela, A.; Freitas-Correa, L.; Oliveira, F. F.; Paula-Lima, A. C.; Saraiva, L. M.; Martins, S. M.; Mota, L. D.; Torres, C.; Alves-Leon, S.; de Souza, J. M. et al. Amyloid-β oligomers induce differential gene expression in adult human brain slices. *J. Biol. Chem.* **2012**, *287*, 7436–7445.
[10] Kong, L. N.; Zuo, P. P.; Mu, L.; Liu, Y. Y.; Yang, N. Gene expression profile of amyloid beta protein-injected mouse model for Alzheimer disease. *Acta Pharmacol. Sin.* **2005**, *26*, 666–672.
[11] Kakinen, A.; Adamcik, J.; Wang, B.; Ge, X. W.; Mezzenga, R.; Davis, T. P.; Ding, F.; Ke, P. C. Nanoscale inhibition of polymorphic and ambidextrous IAPP amyloid aggregation with small molecules. *Nano Res.* **2018**, *11*, 3636–3647.
[12] Nedumpully-Govindan, P.; Kakinen, A.; Pilkington, E. H.; Davis, T. P.; Ke, P. C.; Ding, F. Stabilizing off-pathway oligomers by polyphenol nanoassemblies for IAPP aggregation inhibition. *Sci. Rep.* **2016**, *6*, 19463.
[13] Gurzov, E. N.; Wang, B.; Pilkington, E. H.; Chen, P. Y.; Kakinen, A.; Stanley, W. J.; Litwak, S. A.; Hanssen, E. G.; Davis, T. P.; Ding, F. et al. Inhibition of hIAPP amyloid aggregation and pancreatic β-cell toxicity by OH-terminated PAMAM dendrimer. *Small* **2016**, *12*, 1615–1626.
[14] Pilkington, E. H.; Lai, M.; Ge, X. W.; Stanley, W. J.; Wang, B.; Wang, M. Y.; Kakinen, A.; Sani, M. A.; Whittaker, M. R.; Gurzov, E. N. et al. Star polymers reduce islet amyloid polypeptide toxicity via accelerated amyloid aggregation. *Biomacromolecules* **2017**, *18*, 4249–4260.
[15] Javed, I.; Yu, T. Y.; Peng, G. T.; Sánchez-Ferrer, A.; Faridi, A.; Kakinen, A.; Zhao, M.; Mezzenga, R.; Davis, T. P.; Lin, S. J. et al. *In vivo* mitigation of amyloidogenesis through functional–pathogenic double-protein coronae. *Nano Lett.* **2018**, *18*, 5797–5804.
[16] Wang, M. Y.; Sun, Y. X.; Cao, X. Y.; Peng, G. T.; Javed, I.; Kakinen, A.; Davis, T. P.; Lin, S. J.; Liu, J. Q.; Ding, F. et al. Graphene quantum dots against human IAPP aggregation and toxicity *in vivo*. *Nanoscale* **2018**, *10*, 19995–20006.
[17] Nurunnabi, M.; Khatun, Z.; Huh, K. M.; Park, S. Y.; Lee, D. Y.; Cho, K. J.; Lee, Y. K. *In vivo* biodistribution and toxicology of carboxylated graphene quantum dots. *ACS Nano* **2013**, *7*, 6858–6867.
[18] Kim, D.; Yoo, J. M.; Hwang, H.; Lee, J.; Lee, S. H.; Yun, S. P.; Park, M. J.; Lee, M. J.; Choi, S.; Kwon, S. H. et al. Graphene quantum dots prevent α-synucleinopathy in Parkinson's disease. *Nat. Nanotechnol.* **2018**, *13*, 812–818.
[19] Wang, M. Y.; Kakinen, A.; Pilkington, E. H.; Davis, T. P.; Ke, P. C. Differential effects of silver and iron oxide nanoparticles on IAPP amyloid aggregation. *Biomater. Sci.* **2017**, *5*, 485–493.
[20] Portelius, E.; Zetterberg, H.; Gobom, J.; Andreasson, U.; Blennow, K. Targeted proteomics in Alzheimer's disease: Focus on amyloid-β. *Expert Rev. Proteomics* **2008**, *5*, 225–237.
[21] Savas, J. N.; Wang, Y. Z.; DeNardo, L. A.; Martinez-Bartolome, S.; McClatchy, D. B.; Hark, T. J.; Shanks, N. F.; Cozzolino, K. A.; Lavallée-Adam, M.; Smukowski, S. N. et al. Amyloid accumulation drives proteome-wide alterations in mouse models of Alzheimer's disease-like pathology. *Cell Rep.* **2017**, *21*, 2614–2627.
[22] Sun, Y. X.; Kakinen, A.; Xing, Y. T.; Pilkington, E. H.; Davis, T. P.; Ke, P. C.; Ding, F. Nucleation of β-rich oligomers and β-barrels in the early aggregation of human islet amyloid polypeptide. *Biochim. Biophys. Acta Mol. Basis Dis.* **2019**, *1865*, 434–444.
[23] Usov, I.; Mezzenga, R. FiberApp: An open-source software for tracking and analyzing polymers, filaments, biomacromolecules, and fibrous objects. *Macromolecules* **2015**, *48*, 1269–1280.
[24] Lin, C. Y.; Gurlo, T.; Kayed, R.; Butler, A. E.; Haataja, L.; Glabe, C. G.; Butler, P. C. Toxic human islet amyloid polypeptide (h-IAPP) oligomers are intracellular, and vaccination to induce anti-toxic oligomer antibodies does not prevent h-IAPP-induced β-cell apoptosis in h-IAPP transgenic mice. *Diabetes* **2007**, *56*, 1324–1332.
[25] Faridi, A.; Sun, Y. X.; Okazaki, Y.; Peng, G. T.; Gao, J.; Kakinen, A.; Faridi, P.; Zhao, M.; Javed, I.; Purcell, A. W. et al. Mitigating human IAPP amyloidogenesis *in vivo* with chiral silica nanoribbons. *Small* **2018**, *14*, 1802825.
[26] Kayed, R.; Head, E.; Thompson, J. L.; McIntire, T. M.; Milton, S. C.; Cotman, C. W.; Glabe, C. G. Common structure of soluble amyloid oligomers implies common mechanism of pathogenesis. *Science* **2003**, *300*, 486–489.
[27] Lopes, D. H. J.; Colin, C.; Degaki, T. L.; de Sousa, A. C. V.; Vieira, M. N. N.; Sebollela, A.; Martinez, A. M. B.; Bloch, C. Jr.; Ferreira, S. T.; Sogayar, M. C. Amyloidogenicity and cytotoxicity of recombinant mature human islet amyloid polypeptide (rhIAPP). *J. Biol. Chem.* **2004**, *279*, 42803–42810.
[28] Krotee, P.; Rodriguez, J. A.; Sawaya, M. R.; Cascio, D.; Reyes, F. E.; Shi, D.; Hattne, J.; Nannenga, B. L.; Oskarsson, M. E.; Philipp, S. et al. Atomic structures of fibrillar segments of hIAPP suggest tightly mated β-sheets are important for cytotoxicity. *eLife* **2017**, *6*, e19273.
[29] Joshi-Tope, G.; Gillespie, M.; Vastrik, I.; D'Eustachio, P.; Schmidt, E.; de Bono, B.; Jassal, B.; Gopinath, G. R.; Wu, G. R.; Matthews, L. et al. Reactome: A knowledgebase of biological pathways. *Nucleic Acids Res.* **2005**, *33*, D428–D432.
[30] Cremades, N.; Cohen, S. I. A.; Deas, E.; Abramov, A. Y.; Chen, A. Y.; Orte, A.; Sandal, M.; Clarke, R. W.; Dunne, P.; Aprile, F. A. et al. Direct observation of the interconversion of normal and toxic forms of α-synuclein. *Cell* **2012**, *149*, 1048–1059.
[31] Szklarczyk, D.; Franceschini, A.; Wyder, S.; Forslund, K.; Heller, D.; Huerta-Cepas, J.; Simonovic, M.; Roth, A.; Santos, A.; Tsafou, K. P. et al. STRING v10: Protein-protein interaction networks, integrated over the tree of life. *Nucleic Acids Res.* **2015**, *43*, D447–D452.
[32] Szklarczyk, D.; Morris, J. H.; Cook, H.; Kuhn, M.; Wyder, S.; Simonovic, M.; Santos, A.; Doncheva, N. T.; Roth, A.; Bork, P. et al. The STRING database in 2017: Quality-controlled protein-protein association networks, made broadly accessible. *Nucleic Acids Res.* **2017**, *45*, D362–D368.
[33] Mi, H. Y.; Huang, X. S.; Muruganujan, A.; Tang, H. M.; Mills, C.; Kang, D.; Thomas, P. D. PANTHER version 11: Expanded annotation data from Gene Ontology and Reactome pathways, and data analysis tool enhancements. *Nucleic Acids Res.* **2017**, *45*, D183–D189.
[34] Zhou, X.; Liao, W. J.; Liao, J. M.; Liao, P.; Lu, H. Ribosomal proteins: Functions beyond the ribosome. *J. Mol. Cell Biol.* **2015**, *7*, 92–104.
[35] Deng, L. T.; Pushpitha, K.; Joseph, C.; Gupta, V.; Rajput, R.; Chitranshi, N.; Dheer, Y.; Amirkhani, A.; Kamath, K.; Pascovici, D. et al. Amyloid β induces early changes in the ribosomal machinery, cytoskeletal organization and oxidative phosphorylation in retinal photoreceptor cells. *Front. Mol. Neurosci.* **2019**, *12*, 24.
[36] Anantharam, V.; Lehrmann, E.; Kanthasamy, A.; Yang, Y. J.; Banerjee, P.; Becker, K. G.; Freed, W. J.; Kanthasamy, A. G. Microarray analysis of oxidative stress regulated genes in mesencephalic dopaminergic neuronal cells: Relevance to oxidative damage in Parkinson's disease. *Neurochem. Int.* **2007**, *50*, 834–847.
[37] Pavel, M.; Imarisio, S.; Menzies, F. M.; Jimenez-Sanchez, M.; Siddiqi, F. H.; Wu, X. T.; Renna, M.; O'Kane, C. J.; Crowther, D. C.; Rubinsztein, D. C. CCT complex restricts neuropathogenic protein aggregation via autophagy. *Nat. Commun.* **2016**, *7*, 13821.
[38] Garcia-Esparcia, P.; Sideris-Lampretsas, G.; Hernandez-Ortega, K.; Grau-Rivera, O.; Sklaviadis, T.; Gelpi, E.; Ferrer, I. Altered mechanisms of protein synthesis in frontal cortex in Alzheimer disease and a mouse model. *Am. J. Neurodegener. Dis.* **2017**, *6*, 15–25.
[39] Nutter, C. A.; Kuyumcu-Martinez, M. N. Emerging roles of RNA-binding proteins in diabetes and their therapeutic potential in diabetic complications. *Wiley Interdiscip. Rev. RNA* **2018**, *9*, e1459.
[40] Juan-Mateu, J.; Villate, O.; Eizirik, D. L. MECHANISMS IN ENDOCRINOLOGY: Alternative splicing: The new frontier in diabetes research. *Eur. J. Endocrinol.* **2016**, *174*, R225–R238.
[41] Love, J. E.; Hayden, E. J.; Rohn, T. T. Alternative splicing in Alzheimer's disease. *J. Parkinsons Dis. Alzheimers Dis.* **2015**, *2*, 6.
[42] Lashuel, H. A.; Aljabari, B.; Sigurdsson, E. M.; Metz, C. N.; Leng, L.; Callaway, D. J. E.; Bucala, R. Amyloid fibril formation by macrophage migration inhibitory factor. *Biochem. Biophys. Res. Commun.* **2005**, *338*,

973–980.

[43] Gevorkian, G.; Gonzalez-Noriega, A.; Acero, G.; Ordoñez, J.; Michalak, C.; Munguia, M. E.; Govezensky, T.; Cribbs, D. H.; Manoutcharian, K. Amyloid-β peptide binds to microtubule-associated protein 1B (MAP1B). *Neurochem. Int.* **2008**, *52*, 1030–1036.

[44] Pianu, B.; Lefort, R.; Thuiliere, L.; Tabourier, E.; Bartolini, F. The $A\beta_{1-42}$ peptide regulates microtubule stability independently of tau. *J. Cell Sci.* **2014**, *127*, 1117–1127.

[45] Luo, J. H.; Wärmländer, S. K. T. S.; Gräslund, A.; Abrahams, J. P. Cross-interactions between the Alzheimer disease amyloid-β peptide and other amyloid proteins: A further aspect of the Amyloid cascade hypothesis. *J. Biol. Chem.* **2016**, *291*, 16485–16493.

[46] Lim, Y. A.; Rhein, V.; Baysang, G.; Meier, F.; Poljak, A.; Raftery, M. J.; Guilhaus, M.; Ittner, L. M.; Eckert, A.; Götz, J. Aβ and human amylin share a common toxicity pathway via mitochondrial dysfunction. *Proteomics* **2010**, *10*, 1621–1633.

[47] Götz, J.; Lim, Y. A.; Eckert, A. Lessons from two prevalent amyloidoses-what amylin and Aβ have in common. *Front. Aging Neurosci.* **2013**, *5*, 38.

[48] Liu, Y. B.; Xu, L. P.; Dai, W. H.; Dong, H. F.; Wen, Y. Q.; Zhang, X. J. Graphene quantum dots for the inhibition of β amyloid aggregation. *Nanoscale* **2015**, *7*, 19060–19065.

[49] Wu, C. Y.; Wang, C.; Han, T.; Zhou, X. J.; Guo, S. W.; Zhang, J. Y. Insight into the cellular internalization and cytotoxicity of graphene quantum dots. *Adv. Healthc. Mater.* **2013**, *2*, 1613–1619.

[50] Chong, Y.; Ma, Y. F.; Shen, H.; Tu, X. L.; Zhou, X.; Xu, J. Y.; Dai, J. W.; Fan, S. J.; Zhang, Z. J. The *in vitro* and *in vivo* toxicity of graphene quantum dots. *Biomaterials* **2014**, *35*, 5041–5048.

[51] Matsusaki, M.; Kanemura, S.; Kinoshita, M.; Lee, Y. H.; Inaba, K.; Okumura, M. The protein disulfide isomerase family: From proteostasis to pathogenesis. *Biochim. Biophys. Acta Gen. Subj.* in press, DOI: 10.1016/j.bbagen.2019.04.003.

Chapter 5

Summary and Future directions

Summary

My PhD project has accomplished the objectives as described in Chapters 2, 3&4. The results of my studies have provided crucial new knowledge on the mechanisms of amyloid protein fibrillation, their toxicities *in vitro* and *in vivo*, as well as their interaction with cell membranes and nanomaterials. This knowledge is essential for facilitating the design of potent and biocompatible NP inhibitors for the mitigation of amyloidosis and amyloid diseases.

The major goal of chapter 2 was to identify human plasma corona and understand its role on immune cell responses to amyloid protein fibrillation. Here, oligomeric and fibrillar Aβ (Aβo and Aβf) were prepared and labelled with fluorescent dye. The fibrillation and toxicity of the aggregates were examined by a ThT kinetics assay, TEM and an *in vitro* viability assay with neuronal cells. To probe amyloid protein-immune cell interaction, T cells, Dendritic cells (D cells), Natural Killer Cells (NK cells), B cells, monocytes and granulocytes were phenotyped by antibodies and their associations with the peptide aggregates were recorded with a blood assay using flow cytometry. LSPR chips consisting of antibody-functionalized gold nanorods were used to detect TNF and IL-6 secretion by immune cells. This study revealed a convoluted relationship between the amyloidosis and immunogenicity of Aβ. Specifically, Aβo displayed little difference in cell membrane association in whole blood or washed blood, while Aβf showed a clear preference for binding with all cell types in the absence of plasma proteins. Immune cells exposed to Aβo, but not to Aβf, resulted in significant expression of cytokines IL-6 and TNF. These observations suggested greater immune cell association and cytokine stimulation of Aβo than Aβf, and revealed the contrasting toxicities of Aβo and Aβf resulting from their differential capacities in acquiring a plasma protein corona.

Amyloid fibrils are usually chiral in morphology, an aspect which has rarely been exploited in the literature of amyloidosis inhibition. Accordingly, chapter 3 investigated the first application

of chiral NPs against IAPP amyloidogenesis *in vivo*. Silica nanoribbons eliminated the IAPP nucleation phase and shortened its elongation phase. This accelerated IAPP fibrillization translated to reduced toxicity, especially for the right-handed silica nanoribbons, as revealed by cell viability on βTC6 pancreatic cells and observed by helium ion microscopy. I*n vivo,* chiral silica nanohelices mitigated IAPP toxicity in zebrafish embryos, as reflected by significantly improved survival, development and swimming behaviour of the organism. The results demonstrated a great potency of inhibiting IAPP aggregation and toxicity with their oppositely handed silica nanoribbons.

There was no data available concerning intracellular protein expression upon exposure to IAPP or IAPP plus their NP inhibitors. Here, the proteome of βTC6 pancreatic cells exposed to the monomeric, oligomeric and fibrillar IAPP, in the absence and presence of GQDs, a known protein fibrillation inhibitor, was detailed using mass spectroscopy. A total of 29 proteins were significantly regulated by different forms of IAPP, and majority of these proteins were nucleotide-binding proteins. GQDs regulated aberrant protein expression through H-bonding and hydrophobic interactions, pointing to nanomedicine as a new frontier against human amyloid diseases.

Future direction

Application of nanomaterial against amyloidosis has a great potential in the development of therapeutics against debilitating human diseases such as T2D and dementia. Based on the outcomes of this project, NPs can elicit electrostatic and hydrophobic interactions, hydrogen bonding and π-π stacking with pathogenic amyloid proteins to inhibit or reduce their self-assemblies. Towards novel nanomedicines for curing amyloid diseases, however, further studies on the mechanisms of NP-protein binding in the presence and absence of chaperone proteins, ligands and psychological metals, the biocompatibility, biodistribution and clearance of NPs, and the cross seeding of amyloid proteins are essential. Our findings on the selective

inhibition of IAPP amyloidogensis with chiral silica nanohelices may be applicable to other classes of chiral nanostructures and other types of amyloidosis associated with AD and PD. Such aspect needs to be fully explored.

NPs are not only effective in mitigating protein amyloid fibrillation, but also in restoring intracellular protein expression against the toxicity elicited by amyloid protein aggregation. GQDs are novel candidate to rescue the dysregulation of proteins, especially the nucleotide-binding proteins. Expanding this finding to *in vivo*, similar nanostructures with may have the capacity in regulating protein expression through hydrogen bonding and hydrophobic interaction, may offer new opportunities against human amyloid diseases.

Zebrafish share 80% of disease-related genes with human, carry multiple pathogenic pathways, and entail a high throughput capacity and short lifecycles, compared to mouse and rat models. In the early stage of development, zebrafish embryos can act as a compromise between *in vitro* cell cultures and *in vivo* mouse models, with the possibility of analysing multiple endpoints from survival rate and development to gene assays. More physiological and behaviour tests may involve zebrafish larvae and adults as alternative systems to AD and PD mice for greater economic and time efficiencies as well as greater flexibility in experimental design.